MEASUREMENT OF PARITY-VIOLATING ELECTROWEAK ASYMMETRIES IN $\overrightarrow{e}p$ SCATTERING AT $0.1 < Q^2 < 0.4\,(\mathrm{GeV/c})^2$

A Dissertation

Presented to

The Faculty of the Department of Physics

The College of William and Mary in Virginia

In Partial Fulfillment

Of the Requirements for the Degree of

Doctor of Philosophy

---

by

Jeffery A. Secrest

2005

APPROVAL SHEET

This dissertation is submitted in partial fulfillment of

the requirements for the degree of

Doctor of Philosophy

Jeffery A. Secrest

Approved, November 2005

Dr. Allison Lung, Chair

Dr. David S. Armstrong

Dr. John M. Finn

Dr. Jeffrey K. Nelson

Dr. Marc Sher

Dr. Philip G. Roos, University of Maryland

CONTENTS

LIST OF TABLES

LIST OF FIGURES

ABSTRACT

This work is based on the first engineering run of the G^0 experiment from October 2002 though January 2003 in Hall C at Jefferson Lab. The G^0 experiment will be the first to measure the weak neutral form factors: $G_E^Z(Q^2)$, $G_M^Z(Q^2)$ and $G_A^e(Q^2)$ and to extract the proton's strange form factors: $G_E^s(Q^2)$ and $G_M^s(Q^2)$ via a Rosenbluth separation over a range of Q^2 $(0.1 - 1.0$ $(\mathrm{GeV/c})^2)$. This will require four sets of measurements: forward angle measurements with a proton target, and three sets of backward angle measurements with a hydrogen and deuterium target. The measurements are made of the parity-violating asymmetries in elastic electron scattering.

The G^0 experiment is a major installation at Jefferson Lab's Hall C with a new dedicated spectrometer. The superconducting magnet is made up of 8 coils with a maximum field of 1.6 T·m. The scintillator detector array (detector solid angle between 0.4 - 0.9 sr) detects recoiled protons in the forward angle measurement (where $\theta_p = 70^\circ \pm 10^\circ$ corresponding to scattered electron angles of a few degrees) and to detect scattered electrons in the backward angle measurements. This detector array is made up of a set of 16 pairs of scintillators arranged in 8 sectors around the beam line. Custom electronics handle the high data rate (approximately 1 MHz per detector). The target is a 20 cm long liquid hydrogen cryotarget. Besides the check-out of the new hardware, G^0 has stringent requirements on the performance of the polarized electron beam in order to minimize false asymmetries. Further complicating this fact, in the forward mode, was the requirement that the time structure of the JLab beam had to be changed from 499 MHz to 31 MHz in order to count the recoiled protons in the spectrometer. Data was collected over a 12 day period at the end of the engineering run. These data were analyzed for a Q^2 range of $0.1 - 0.4$ $(\mathrm{GeV/c})^2$ corresponding to measured electroweak asymmetries that ranged from (-4.4 $\pm$ 1.6 $\pm$ 1.6 ppm) to (-8.5 $\pm$ 2.8 $\pm$ 2.5 ppm).

CHAPTER 1

Introduction

The existence of the proton has been known since the early 20th century, yet its structure is still not entirely understood. The current theory of the strong interaction, Quantum Chromdynamics (QCD), describes the proton as being made up of three valence quarks (two up and one down quarks) within a complicated "sea" of quarks, antiquarks and gluons. A troubling difficulty of QCD is that while it successfully describes the strong interaction at high momentum transfers where the theory is perturbative, the theory is more difficult to handle at low momentum transfers where the theory is non-perturbative.

Strange and anti-strange quarks, which are the next lightest quarks after the up and down, are found in the quark "sea" around the proton. Since strange quarks have a comparable mass with the proton, the question can be asked, what role do they play in contributing to the static properties of the proton?

1.1 Strange Quarks in the Proton

Strange quarks are the lightest quarks not to contribute to the proton's valence distribution. The strange quarks exist as only strange quark-antiquark pairs in the

quark sea surrounding the proton. The net strangeness of the proton is zero. This might lead one to believe that strange quarks cannot contribute to the properties of the proton. Experiments have indicated that strange quarks do, in fact, play a fundamental role in the understanding of the proton [1–5, 12].

One set of strange quark observables is related to the so-called strange quark matrix elements of the nucleon. These matrix elements have the form

$$\langle P|\bar{s}\Gamma s|P\rangle \tag{1.1}$$

where $|P\rangle$ is the proton state, $\bar{s}\Gamma s$ is an operator containing strange quark, s, fields bilinearly, Γ is a matrix in spinor space which takes the form $\Gamma = 1_4$, γ^μ, or $\gamma^\mu\gamma_5$ depending on whether one is interested in the scalar, vector, or axial strangeness of the proton.

One of the original indicators that strange quarks play a fundamental role in the proton came from looking at the pion-nucleon sigma term. Strange quarks contribute to the mass of the proton via the matrix element $\langle P|\bar{s}s|P\rangle$. This matrix element can be inferred from the so-called "sigma term" in π-N scattering. The pion-nucleon sigma term is defined to be

$$\sigma_{\pi N} = \hat{m}\langle P|\bar{u}u + \bar{d}d|P\rangle \tag{1.2}$$

where $\hat{m} = \frac{1}{2}(m_u + m_d)$, the average of the up and down quark masses. The proton mass, under the SU(3) flavor assumption that one can neglect $c\bar{c}$, $b\bar{b}$ and $t\bar{t}$, can then be written as

$$M_p = M_0 + \sigma_s + \sigma \tag{1.3}$$

where M_p is the physical mass of the proton, M_0 is the mass of the proton as the quark masses go to zero (in the so-called chiral limit), σ_s is the mass contribution due to strangeness (if any) and σ is the mass contribution from non-strange quarks.

The pion-nucleon term $\sigma_{\pi N}$ can be used to find the non-strangeness quark contribution σ by extracting $\sigma_{\pi N}$ at the unphysical Cheng-Daschen point (that is, where the Mandelstam variables $s = M_p^2$ and $t = m_\pi^2$) by use of dispersion relations. The standard value [1] for this result, after taking into account higher-order contributions, is $\sigma = 45 \pm 8$ MeV.

If the nucleon is free of strange quarks, σ should equal the SU(3)-octet scaler quark density which can be calculated from the baryon masses

$$\hat{\sigma} = m_0 \langle P|\bar{u}u + \bar{d}d - 2\bar{s}s|P\rangle. \tag{1.4}$$

This has been calculated [2,3],to be $\hat{\sigma} = 35 \pm 5$ MeV.

Comparing $\hat{\sigma}$ and σ, deviations from the equality, are assumed to be coming from strange quarks. This can be written as

$$\hat{\sigma} = \sigma(1 - y). \tag{1.5}$$

where y is the strangeness content of the proton, which can then be written as

$$y = \frac{2\langle P|\bar{s}s|P\rangle}{\langle P|\bar{u}u + \bar{d}d|P\rangle}. \tag{1.6}$$

This leads to a value of $y = 0.2 \pm 0.2$, indicating that strange quarks might contribute to the mass of the proton. This implies that as much as 200 MeV of the proton's mass might be due to the strange quarks. This result also indicates a violation of the OZI rule [7] which assumes that the nucleon is free of strange quarks. This result must be accepted with some degree of skepticism since there is a significant uncertainty due to the data and the extensive theory needed to interpret this result.

Another piece of evidence for strange quark contributions to the nucleon come from some $\bar{p}p$ annihilation channels [8,9]. In these channels, an observed enhancement of ϕ relative to ω production is in disagreement with the OZI prediction by a

factor of 30-50. A possible interpretation of these results is that the nucleon wave function contains some significant fraction of polarized $\bar{s}s$ pairs.

Another indicator that strange quarks play a role in the proton comes from polarized deep inelastic scattering (DIS) experiments. This method allows for access to the $\langle P|\bar{s}\gamma^5 s|P\rangle$ matrix element. The focus of these experiments is the spin structure of the nucleon. These spin structure experiments indicate that the fraction of the proton spin carried by the valence quarks is $\Sigma \sim 0.3$. This naturally leads to the question: is some of the missing spin due to strange quarks?

Each of the quark (antiquark) flavors can be described by a single quark (antiquark) distribution function $q(x)$ ($\bar{q}(x)$) over a range in Bjorken x, where Bjorken x is the fraction of four-momentum carried by a parton in the proton. The distribution $q(x)$ is the probability that a parton carries a fraction x of the momentum of the proton. A quantity of interest is the net spin polarization, Δq, of the quark flavor q

$$\Delta q \equiv \int_0^1 [q^{\uparrow}(x) - q^{\downarrow}(x) + \bar{q}^{\uparrow}(x) - \bar{q}^{\downarrow}(x)]dx. \tag{1.7}$$

The $g_1(x)$ structure function is the charge-weighted vector sum of the quark polarizations in the nucleon

$$g_1 = \frac{1}{2}\sum_q Q_q \Delta q \tag{1.8}$$

The first moment of the $g_1(x)$ structure function, Γ_1, describes the total spin carried by the quarks

$$\Gamma_1 \equiv \int_0^1 g_1(x)dx. \tag{1.9}$$

The Ellis-Jaffe sum rule [10] connects the structure functions to the quark spin distributions using Equations 1.8 and 1.9. The Ellis-Jaffe sum rule for the proton

can be written as

$$\Gamma_1^p = \frac{1}{12}\left[1 + \left(\frac{5}{3}\right)\frac{3F/D - 1}{F/D + 1}\right] \tag{1.10}$$

where F and D are the universal weak decay constants. Ellis and Jaffe assumed that the strange quarks do not contribute to the nucleon's spin and SU(3) flavor symmetry. This results in $\Delta s = 0$. Ellis and Jaffe's calculation results in the relation,

$$\Gamma_1^p = \frac{1}{2}\left(\frac{4}{9}\Delta u + \frac{1}{9}\Delta d\right) = 0.17 \tag{1.11}$$

The EMC collaboration [11] measured Γ_1^p and found

$$\Gamma_1^p = 0.126 \pm 0.010(stat) \pm 0.015(syst) \tag{1.12}$$

which is in disagreement with the calculated results in Equation 1.11 where Δs was frozen out. This was a hint that strange quarks might play a role in the properties of the proton.

Now with these results one can isolate the individual flavor components. The total fraction of the nucleon spin carried by the quarks is [4, 5]

$$\Delta u + \Delta d + \Delta s = 0.20 \pm 0.10. \tag{1.13}$$

The portion of the spin due to strange quarks is [4, 5]

$$\Delta s = -0.1 \pm 0.1. \tag{1.14}$$

The minus sign implies that the strange quarks and antiquarks are polarized negatively with respect to the direction of the nucleon spin. This extracted value is to be taken with care since the strange quark extraction is sensitive to SU(3) flavor breaking, and information from neutron beta decay and hyperon semi-leptonic decays had to be incorporated into the analysis assuming exact SU(3) flavor symmetry.

Another DIS technique that is employed is the scattering of neutrinos and anti-neutrinos with nucleons to probe the $s\bar{s}$ sea. The NuTeV experiment [12] at Fermilab looked at the production of charmed particles in charged-current interactions of neutrinos and anti-neutrinos with nucleons in the deep inelastic region. These charmed particles are produced in $d-c$ and $s-c$ transitions. The neutrinos interact with the d and s quarks by raising their charge and producing a negative lepton. The $d-c$ transition is a Cabibbo suppressed one. This enhances the possibility of studying the strange sea. By observing two muon-neutrino events, the NuTeV collaboration extracted the total momentum fraction κ of the strange sea as [12]

$$\kappa = \frac{2\int_0^1 (s+\bar{s})dx}{\int_0^1 (u+\bar{u}+d+\bar{d})dx} = 0.42 \pm 0.07 \pm 0.06 \tag{1.15}$$

at $Q^2 = 16$ (GeV/c)^2.

From experiment, there has thus been evidence that the strange quark-antiquark sea may play a significant role in the proton. Much work has gone into extracting the $\pi - N$ sigma term to find the strange quark mass contribution, but theoretical uncertainties still exist. The strange quark-antiquark contribution to the spin of the proton has been another subject of intense research, but once again the result suffers from uncertainties in the theoretical interpretation. Low energy neutrino scattering will offer the best hope in measuring Δs. This can be technically challenging since there can be uncertainties in knowing the neutrino flux, the detector efficiencies, and nuclear target effects. With all these tantalizing hints, parity-violating electron-proton scattering is attractive, as it is a technique that has the potential to provide a direct and clean measurement of the strange vector and axial currents in the nucleon.

1.2 Parity-Violating Electron Scattering

In order to access the strange magnetic and electric form factors, parity-violating electron scattering has been employed. The strange magnetic and electric form factors, represented by G_E^s and G_M^s, are physical observables related to the strange quark charge and magnetic distributions in the nucleon. In electron-proton scattering, two different kinds of interactions are involved: the electromagnetic interaction via the exchange of a photon and the weak interaction via Z^0 exchange. This can be seen from the cross-section in Figure 1.1.

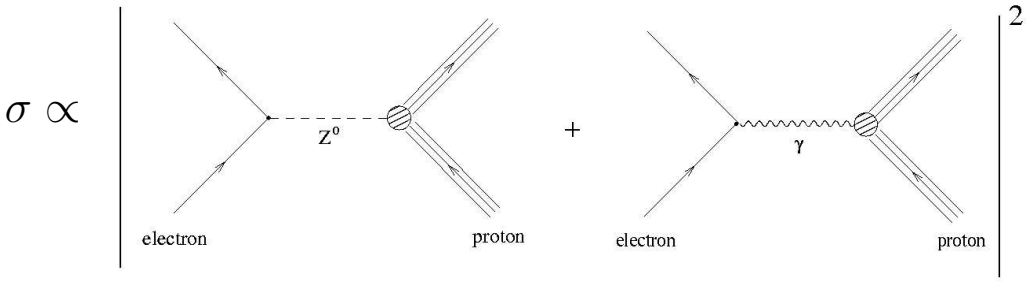

FIG. 1.1: *Electromagnetic and weak contributions to the scattering cross section in electron proton scattering.*

Typically, at low momentum transfers, the weak interaction is ignored since it is small in comparison to the electromagnetic contribution. However, the weak interaction violates parity, thus by using polarized electrons and forming the ratio of the difference of polarized cross sections over the sum of the polarized cross sections, an asymmetry can be formed, which is non-zero only due to the weak interaction. This asymmetry can be written for longitudinally polarized electrons scattering from an unpolarized proton target, as

$$A = \frac{\sigma_+ - \sigma_-}{\sigma_+ + \sigma_-} \approx \frac{G_F Q^2}{4\sqrt{2}\pi\alpha} \approx 10^{-4} Q^2 \tag{1.16}$$

where G_F is the Fermi constant, Q^2 is the momentum transfer ($0.1 < Q^2 < 1.0$ (GeV/c)^2 for the G^0 experiment), $\sigma_{+(-)}$ (sometimes this is denoted as $\sigma_{r(l)}$) is the

cross section for right (left) handed incident electrons scattering from a proton and α is the fine structure constant. A right (left) handed particle is a particle whose spin vector is parallel (anti-parallel) to its momentum vector. This is known as the particle's helicity. This asymmetry can then be related to the electromagnetic and weak form factors. The form factors can then be written in terms of quark flavors. Then by utilizing charge symmetry between the neutron and proton, the asymmetry can be written in terms of known electromagnetic form factors for the proton and neutron and the strange quark form factors.

Measuring asymmetries on the order of 10^{-6} with errors on the order of 10^{-7} is a challenging feat. In order to make a measurement with this precision, a large number of scattering events with specified helicity is required. The number of scattered events, n_s is given by

$$n_s = \frac{d\sigma}{d\Omega} \times \mathcal{L} = \frac{d\sigma}{d\Omega} \times I \times \rho \times L \times \Delta\Omega \tag{1.17}$$

where $\frac{d\sigma}{d\Omega}$ is the differential scattering cross section, I is the beam current, ρ is the density of the target, L is the target length, $\Delta\Omega$ is the solid angle of the detector and $\mathcal{L}$ is the luminosity. It is most important to maximize the luminosity in order to get as many events as possible. This in turn drives the characteristics common to most electron-nucleon parity-violation experiments:

- high beam polarization

- high beam currents

- long targets

- large detector solid angles.

Another concern with parity experiments is the control of helicity-correlated systematic errors. The measured asymmetry is fairly insensitive to common systematic

errors. Let N_{sys} be the number of counts associated with a common systematic error such as small drifts in some experimental parameter. Forming the measured asymmetry, A_{meas}, with this common systematic error

$$\begin{aligned} A_{meas} &= \frac{(N_+ + N_{sys}) - (N_- + N_{sys})}{(N_+ + N_{sys}) + (N_- + N_{sys})} && (1.18) \\ &= \frac{N_+ - N_-}{N_+ + N_- + 2N_{sys}} && (1.19) \\ &\approx \frac{N_+ - N_-}{2N}\left(1 + \frac{N_{sys}}{N}\right)^{-1} && (1.20) \\ &\approx A_{PV}\left(1 - \frac{N_{sys}}{N}\right) && (1.21) \end{aligned}$$

where N_+ is the number of right-handed scattered particles, N_- is the number of left-handed scattered particles, $N \approx \frac{N_+ + N_-}{2}$, and A_{PV} is the parity-violating asymmetry without the systematic contribution.

On the other hand, parity experiments must guard against helicity-correlated systematic errors. Using the variables defined above, but now with a helicity-correlated systematic error, N_{HC_sys} the measured asymmetry, A_{meas}, can be written as

$$\begin{aligned} A_{meas} &= \frac{(N_+ - N_{HC\_sys}) - (N_- - N_{HC\_sys})}{(N_+ - N_{HC\_sys}) + (N_- - N_{HC\_sys})} && (1.22) \\ &\approx \frac{N_+ - N_- + 2N_{HC\_sys}}{N_+ - N_-} && (1.23) \\ &\approx A_{PV} + \frac{N_{HC\_sys}}{N}. && (1.24) \end{aligned}$$

These helicity-correlated systematic errors which come in as an additive factor to the 'true' A_{PV} must be controlled since they form a false asymmetry which adds directly to the true asymmetry.

In order to control systematic errors and increase the number of scattered events measured by the detector(s), a variety of techniques have been established. Some of these techniques are:

- GaAs and strained GaAs crystals used as photo-cathodes
- rapid pseudo-random reversal of the beam helicity
- precision beam monitors
- passive helicity reversal (typically by an insertable halfwave plate)
- beam intensity and position feedback.

In general, most electron-nucleon scattering parity experiments have similar set-ups. Linearly-polarized light from a laser is transformed into circularly-polarized light by a Pockels cell. By applying different voltages to the Pockels cell, left and right-handed polarized light is produced. This circularly-polarized light shines on a GaAs crystal liberating polarized electrons by the photo-electric effect. An insertable half-wave plate can be inserted and retracted from the laser beam allowing for passive helicity reversal to check for (and cancel) some systematic errors.

The polarized electrons are accelerated to some energy before impinging on a target. During the transport through the accelerator and experimental end station, beam position and current monitors detect helicity-correlated differences in the beam. Position monitors in an accelerator arc can be used to measure the helicity-correlated energy differences. These beam monitors feed data to feedback systems which in turn attempt to minimize the helicity-correlated differences. Detector packages can then be arranged in the experimental end station to detect the scattered particles.

1.3 Overview of the G^0 Experiment

The full measurement of the G^0 experiment will access the strange quark contributions to the magnetic and charge distributions of the proton, $G_M^s(Q^2)$, $G_E^s(Q^2)$,

and the electron-proton axial form factor, $G_A^e(Q^2)$. This will be done by measuring parity-violating asymmetries in forward elastic electron-proton scattering and backward scattering for elastic electron-proton and quasi-elastic electron-deuteron scattering. The parity-violating asymmetries are expected to range from -3 to -35 parts-per-million (ppm)[1] for the forward angle measurements and the asymmetries measured in the backward angle configuration on hydrogen are expected to be larger, ranging from -18 to -72 ppm. This will allow for a clean extraction of $G_M^s(Q^2)$, $G_E^s(Q^2)$ and $G_A^e(Q^2)$ with few assumptions (such as charge symmetry). The complete G^0 experiment will be the first experiment to completely separate $G_M^s(Q^2)$, $G_E^s(Q^2)$ and $G_A^e(Q^2)$ and to measure the evolution of these observables at three different momentum transfers (Q^2). G^0 is a counting experiment in contrast to previous parity-violating experiments like SAMPLE [13] at MIT-Bates and HAPPEX [14] in Hall A at Jefferson Lab that used an integrating technique.

The G^0 experiment is located in Hall C at Jefferson Lab. A dedicated large acceptance spectrometer (see Figure 1.2) was built in order to perform the experimental program. The spectrometer is a toroidal magnet consisting of 8 superconducting coils in a common cryostat that generate up to a 1.6 T field. The diameter of this spectrometer is about 4 m, and it has an operating current of 5000 A. The total energy stored in the magnet is 6.6 MJ. The solid angle is defined by collimators at the inner diameter of the coils. This geometry allows a line-of-sight shield from the detectors to the target. Elastically scattered particles of the same Q^2 are focused onto individual focal plane detectors. Each detector is made of a pair of plastic scintillators. There are 8 sets of 16 detector pairs called octants that are placed symmetrically around the symmetry axis of the spectrometer.

For the measured asymmetries, which are on the order of parts-per-million, the

[1]Due to the large number of abbreviations and acronyms, Appendix A is glossary of many terms used in this experiment.

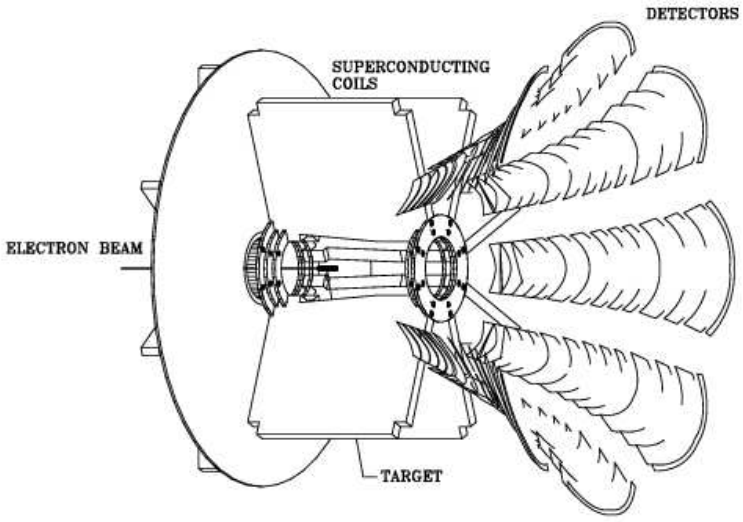

FIG. 1.2: *Schematic of the G^0 apparatus at JLab. This is a dedicated spectrometer in Hall C. In the forward configuration, polarized electrons hit an unpolarized hydrogen target and the recoil protons are detected while the electrons scatter at a forward angle. The apparatus can then be turned around so that polarized electrons hit an unpolarized hydrogen (deuterium) target and the back-scattered electrons are detected.*

level of statistical uncertainty will be about 5% and the systematic uncertainties related to helicity-correlated effects should be on the order of 10^{-7}. The G^0 collaboration will extract G_E^s, G_M^s, and G_A^e at the values $Q^2 = 0.30$, 0.50, and 0.80 $(\mathrm{GeV/c})^2$ from the measured asymmetries. The projected errors from this extraction are shown in Table 1.1 and in Figures 1.3, 1.4, and 1.5. The calculation assumes 700 hours of data taking for the forward angle measurement on the hydrogen target and for each of the backward angle measurements on the hydrogen and deuterium targets. It is the statistical uncertainties on these measured asymmetries that dominate the overall errors on G_E^s, G_M^s, and G_A^e. The polarization of the electron beam is assumed to be $70 \pm 2\%$ in the calculation of these proposed errors. It is the polarization measurement that is expected to dominate the systematic errors on G_E^s, G_M^s, and G_A^e. Errors coming from the uncertainties in the electromagnetic form factors are: 20% for G_E^n, 3% for G_M^n, 2% for G_E^p, and 2% for G_M^p. A theoretical uncertainty

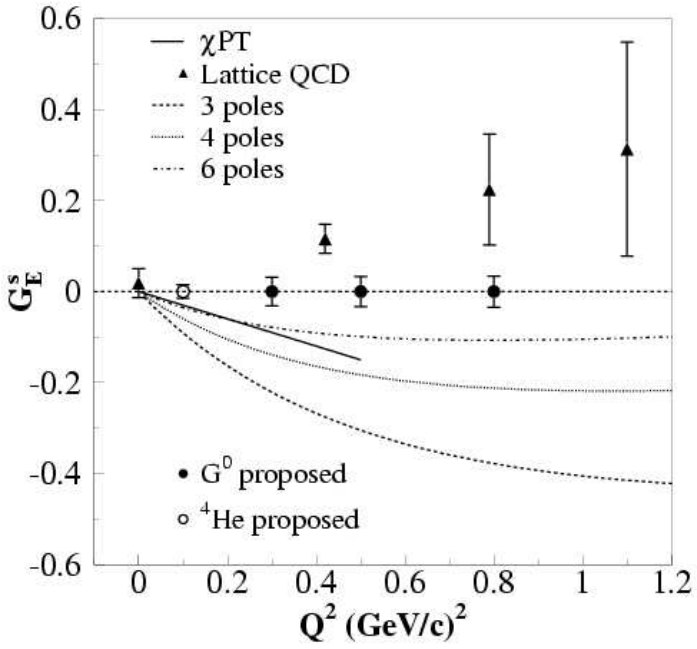

FIG. 1.3: *Projected errors on G_E^s. Result from the SAMPLE experiment is shown along with the expected errors from the HAPPEX II experiments. Also shown are theoretical predictions from chiral perturbation theory, lattice QCD, and various pole (dispersion analysis) models.*

had to be included on the isoscaler part of the electron-proton axial form factor, $G_A^e(T=0)$ since this contribution is not accessible in the asymmetry measurements. The momentum transfer Q^2 is expected to be measured to within 1%.

In the first phase of the G^0 experiment, forward angle asymmetries are measured. This is done by detecting elastically scattered protons between $62^\circ < \theta_p < 78^\circ$ The 20 cm liquid hydrogen target is based on the SAMPLE [15] design. The target's main requirement is that the density remain constant as the beam deposits up to 500 W of power. The target provides a high longitudinal flow of about 5-10 m/s in order to provide enough mixing by turbulent flow. The spectrometer has an acceptance of ~ 0.9 sr defined by collimators at the inner radius of the coils of the magnet. The measured Q^2 range is from $0.1 < Q^2 < 1.0$ (GeV/c)^2 with an incident beam energy of 3.0 GeV. The scattered particles are detected by pairs of plastic

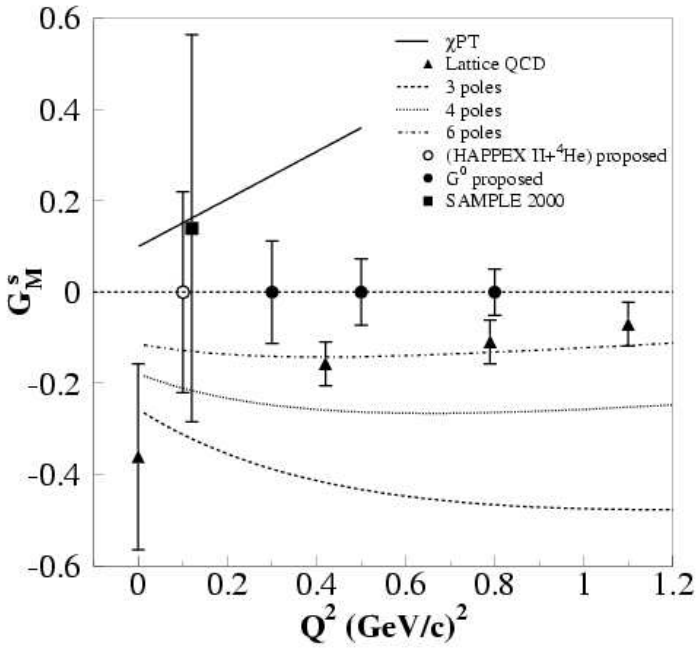

FIG. 1.4: *Projected errors on G_M^s. Result from the SAMPLE experiment is shown along with the expected errors from the HAPPEX II experiments. Also shown are theoretical predictions from chiral perturbation theory, lattice QCD, and various pole (dispersion analysis) models.*

scintillators known as the Focal Plane Detectors (FPDs). For each of the eight sectors, there are 16 detector pairs corresponding to increasing Q^2 with increasing detector number. The detectors are shaped into arcs of a circle in order to collect events of approximately the same Q^2. In the forward mode, time-of-flight is used to reject some of the backgrounds. Since it takes about 20 ns for a proton to reach a detector from the target, the CEBAF machine producing polarized electrons must reduce the micro-structure of the beam bursts from 499 MHz to 31 MHz in order to to provide electrons every 32 ns for this experiment. Custom electronics were built to accumulate the time-of-flight spectra in this configuration. These time-of-flight data are recorded by shift registers that feed scalers. This time-of-flight measurement, made over a 32 ns window, is used to supplement the momentum selection by the spectrometer and separate elastic from inelastic contributions, allowing for

	G_E^s			G_M^s			$G_A^e(T=1)$		
Q^2(GeV/c)^2	0.30	0.50	0.80	0.30	0.50	0.80	0.30	0.50	0.80
Error (ppm)	0.032	0.037	0.052	0.090	0.059	0.041	0.188	0.159	0.137
A_f (%)	20.3	11.4	12.5	0.20	0.1	0.1	1.5	0.7	0.7
A_b (%)	31.0	34.3	37.8	50.3	47.4	47.9	0.9	0.8	0.9
A_{deut} (%)	14.3	17.1	22.0	23.3	23.7	27.9	61.8	62.6	72.6
G_E^p (%)	2.1	1.9	1.0	0.0	0.0	0.0	1.1	0.4	0.1
G_M^p (%)	1.5	1.3	0.6	0.9	1.2	1.0	0.4	0.8	0.8
G_E^n (%)	12.2	10.9	5.7	0.3	0.2	0.1	0.9	0.6	0.3
G_M^n (%)	0.9	0.9	0.6	1.4	2.0	1.9	3.8	3.1	1.9
Q^2 (%)	4.4	4.9	3.7	5.0	4.8	3.3	7.2	6.9	4.8
P_e (%)	11.4	14.3	11.8	15.6	16.5	12.5	22.3	23.8	17.8
$G_A^e(T=0)$ (%)	1.8	3.1	4.2	3.0	4.2	5.3	0.1	0.2	0.2

TABLE 1.1: *Expected relative contributions of statistical and systematic errors on the proposed full G^0 experiment for G_E^s, G_M^s, and G_A^e. The total absolute error is noted in the second line of the table. The statistical errors on the forward, backward, and deuterium asymmetry measurements are denoted by A_f, A_b, and A_{deut} respectively.*

background corrections to the elastic asymmetries. The maximum rate of elastically scattered protons for a given detector pair is about 1 MHz.

The longitudinally-polarized electrons are provided by the Continuous Electron Beam Facility (CEBAF). Linearly-polarized light is provided by a laser in the injector and is turned into circularly-polarized light by a $\frac{\lambda}{4}$ waveplate (a Pockels cell). This circularly-polarized light interacts with a "strained" GaAs photocathode and liberates longitudinally-polarized electrons. The helicity of the electrons can be reversed by changing polarity of the voltage applied to the Pockels cell. As mentioned above, G^0 requires a beam energy of 3.0 GeV, with high intensity (40 μA) and a pulsed structure (31 MHz instead of the typical 499 MHz) in the forward angle phase of the experiment. This mode produces a charge per bunch that is 16 times larger than normal. This requires changes to be made to the beam optics. It is important for G^0 to control any helicity-correlated beam differences. This is because these beam differences may manifest themselves as false asymmetries.

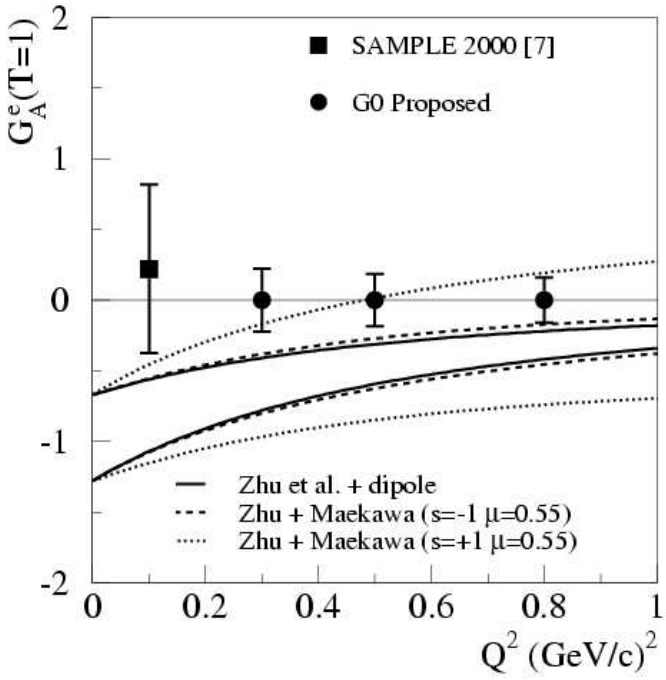

FIG. 1.5: *Projected errors on G_A^e. Result from the SAMPLE experiment is shown. Also shown are theoretical predictions.*

In the second phase of the G^0 experiment, backward angle asymmetries will be measured. This will be done by reversing the apparatus relative to the beam line. Elastically scattered electrons will be detected at 110° from the same 20 cm liquid hydrogen target. In this phase of the experiment, the background is expected to be composed of electrons and pions from inelastic processes. In this case, the time-of-flight cannot discriminate between the different reactions and thus the selection between particles will be obtained from their different trajectories. To aid in discrimination of elastic and inelastic electrons, another set of 9 detectors, the cryostat exit detectors (CEDs) will be added near the exit window of the cryostat. The Focal Plane Detector arrays will be reduced to a single layer of 16 scintillators. This reduction of the FPDs is due to the fact that the CEDs act as the second scintillator. The decision to keep the front FPD scintillator and not the back FPD scintillator is

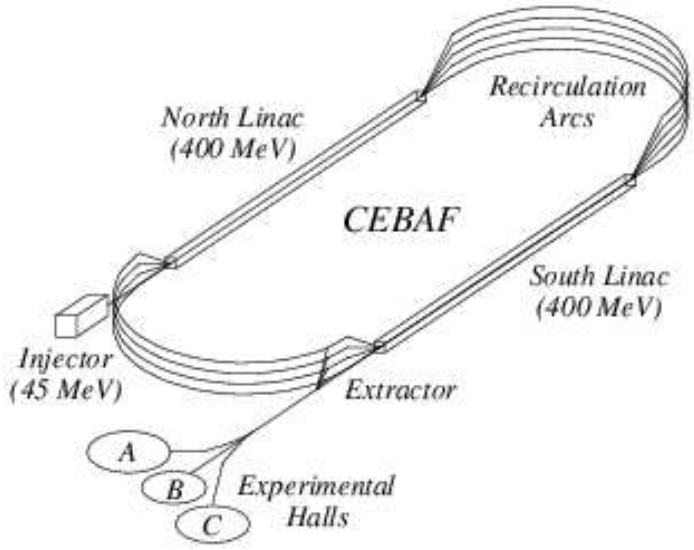

FIG. 1.6: *The CEBAF accelerator at JLab.*

because the front detector could become a source of background/multiple scattering for the back scintillator. The coincidence between the CED-FPD combination allows for a rough measurement of the electron momentum and scattering angle. To reject pion background from the entrance and exit foils of the targets, a Cerenkov detector will be placed between the CEDs and the FPDs. In the backward mode, programmable logic chips in the electronics will be employed to identify elastic events from CED/FPD coincidences. The target will also be filled with liquid deuterium in order to perform a third set of measurements for the extraction of the axial form factor.

This thesis is based on the work of the First G^0 Engineering Run that occurred in October 2002 through the January 2003. The First G^0 Engineering Run was a "proof of principle" run. The layout of this thesis is as follows: Chapter 2 describes the formalism of parity-violating electron-nucleon scattering and previous experiments, Chapter 3 describes the G^0 experimental apparatus with an emphasis on the polarized electron beam (discussed in further detail in Appendix B) and on

the North American detector system (further discussed in Appendix C), Chapter 4 describes the analysis of the data from the raw asymmetries to the extracted physics asymmetries with a particularly detailed discussion on the extraction of the inelastic dilution factors, and in Chapter 5, the physics asymmetries are compared to the standard model predictions and the performance of the individual components of the G^0 experiment are discussed.

CHAPTER 2

Physics Formalism

Parity-violating electron scattering is a practical and clean method for measuring the strange quark vector matrix elements. This is done by measuring the parity-violating amplitudes arising from the electroweak interference in elastic scattering of polarized electrons from an unpolarized proton. In this chapter, the formalism required to interpret the G^0 experiment is presented.

2.1 Structure of the Proton

The proton is a composite particle made up of quarks and gluons (collectively known as partons). This cluster of quarks and gluons that form the proton can be approximately written as

$$p = \underbrace{uud}_{\text{valence quarks}} + \underbrace{u\bar{u} + d\bar{d} + s\bar{s} + \ldots}_{\text{sea quarks}} + \underbrace{g + g + \ldots}_{\text{gluons}}; . \tag{2.1}$$

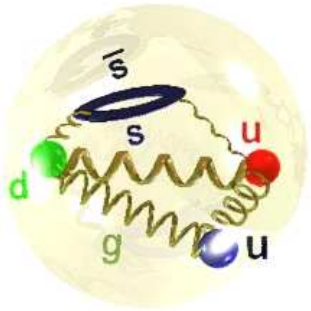

FIG. 2.1: *The proton is made up of three valence quarks, two up and one down quark. Gluons, the mediator of the strong interaction, are exchanged between quarks to hold the proton together. These gluons, by virtue of the Heisenberg uncertainty principle, bubble into quark-antiquark pairs as illustrated by the strange quarks in this figure.*

The first term in Equation 2.1 refers to the so-called "valence quarks", where the current quark masses are

$$m_u \approx 5\,\text{MeV} \tag{2.2}$$

$$m_d \approx 9\,\text{MeV} \tag{2.3}$$

$$m_s \approx 175\,\text{MeV}. \tag{2.4}$$

The second term is related to the large number of relatively low-momentum quark-antiquark pairs, known collectively as "sea quarks". The probability of these $q\bar{q}$ pairs fall off inversely with the mass of the quark species being produced (this is why the heavy $c\bar{c}$, $b\bar{b}$, and $t\bar{t}$ are expected to play a relatively small role). The quarks are all held together by the mediator of the strong interaction, gluons. In fact, it is from these gluons that the $q\bar{q}$ sea quarks are generated via the Heisenberg uncertainty relation much like in e^+e^- vacuum polarization in QED. As has been demonstrated in Section 1.1, strange quarks may play a major role in the structure of the proton and accessing the strange quarks says something about the pure sea quarks. Sadly, perturbative QCD cannot light the way, since the mass of the strange quark, m_s is comparable to the QCD scale, λ_{QCD}, where $\frac{\lambda_{QCD}}{m_s} \sim 1$.

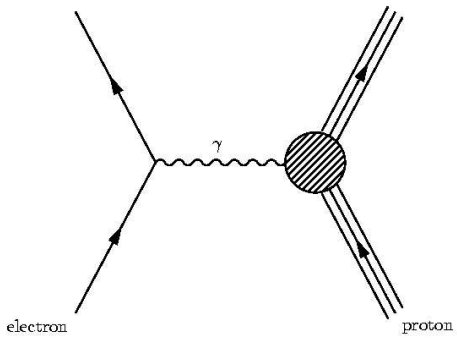

FIG. 2.2: *Tree level Feynman diagram for electron-proton electromagnetic scattering.*

2.2 Electromagnetic Form Factors

Electromagnetic form factors describe the complicated interactions of photons with the complex structure of the nucleon in elastic scattering (see the tree-level Feynman diagram in Figure 2.2). This tree-level scattering diagram is described by the following scattering amplitude for the single photon exchange

$$\mathcal{M}_\gamma = -\frac{4\pi\alpha}{q^2} J_e^\mu J_\mu^p. \tag{2.5}$$

The electron is a point-like spin-$\frac{1}{2}$ particle; the associated current for the electron is

$$J_e^\mu = \bar{u}\gamma^\mu u \tag{2.6}$$

where u is the Dirac 4-component spinor that describes the initial electron, u is the Dirac 4-component adjoint spinor of the final electron, and γ^μ is the Dirac gamma matrix. In contrast, the proton, being an extended spin-$\frac{1}{2}$ particle, yields a more complicated transition current due to its complex structure. Since the electromagnetic interaction respects parity conservation, Lorentz invariance and current conservation, the transition current can be written in the general form as

$$J_\mu^p = \bar{u}\left[\gamma_\mu F_1 + i\left(\frac{\kappa}{2M_p}F_2\right)\sigma_{\mu\nu}q^\nu\right]u \tag{2.7}$$

where $F_1(Q^2)$ and $F_2(Q^2)$ are known as the Dirac and Pauli form factors respectively, $\kappa = 1.79$ nuclear magnetons is the anomalous part of the magnetic moment of the proton (if the proton were structureless then $\kappa = 0$). The momentum transfer, Q^2, is the only variable needed to describe the electromagnetic interaction vertex and hence the form factors are only functions of momentum transfer.

The Sachs form factors are more physically insightful combinations of the Dirac and Pauli form factors, and allow for a more convenient formalism to be written without form factor cross terms in the cross section for electron-nucleon scattering. In the Breit frame, where the exchanged boson (in this case a virtual photon or Z^0) is purely space-like ($Q^2 = 0$), this implies that the initial and final momentum of the scattered particle is equal in magnitude but opposite in sign ($\vec{p}' = \vec{p}$). These form factors are closely related to the proton charge and magnetic moment distributions. The Sachs form factors are related to the Pauli and Dirac form factors by

$$G_E^p(Q^2) \equiv F_1 - \tau F_2 \qquad\qquad G_M^p(Q^2) \equiv F_1 + F_2 \tag{2.8}$$

where $\tau = \frac{Q^2}{4M_N^2}$ is a measure of the relativistic recoil effects. At $Q^2 = 0$ these form factors are normalized to

$$G_E^p(Q^2 = 0) = \frac{q_0}{e} \qquad\qquad G_M^p(Q^2 = 0) = \frac{\mu_p}{e/2M_p} \tag{2.9}$$

where q_0 is the proton's electric charge and μ_p is the proton's magnetic moment. G_E^p and G_M^p can be determined from elastic electron-proton scattering experiments. In these experiments, the differential cross sections, $\dfrac{d\sigma}{d\Omega}$, are measured at different values of Q^2 and lab angle, θ. The Rosenbluth formula [16] which describes the elastic electron-proton scattering can then be applied

$$\frac{d\sigma}{d\Omega} = \left(\frac{d\sigma}{d\Omega}\right)_{Mott} \left[\frac{(G_E^p)^2 + \tau(G_M^p)^2}{1+\tau} + 2\tau(G_M^p)^2 \tan^2\left(\frac{\theta}{2}\right)\right] \tag{2.10}$$

where $\left(\frac{d\sigma}{d\Omega}\right)_{Mott}$ is the Mott differential cross section [17] which describes the scattering of spin $\frac{1}{2}$ Dirac particles and takes into account the recoil of the proton. A

Rosenbluth plot (as shown in Figure 2.3) can be made showing the cross section as a function of $\tan^2(\frac{\theta}{2})$ for constant Q^2. The data should lie along a straight line with a slope of $2\tau(G_M^p)^2$ and the extrapolation to $\tau = 0$ will determine the electric form factor G_E^p for that value of Q^2.

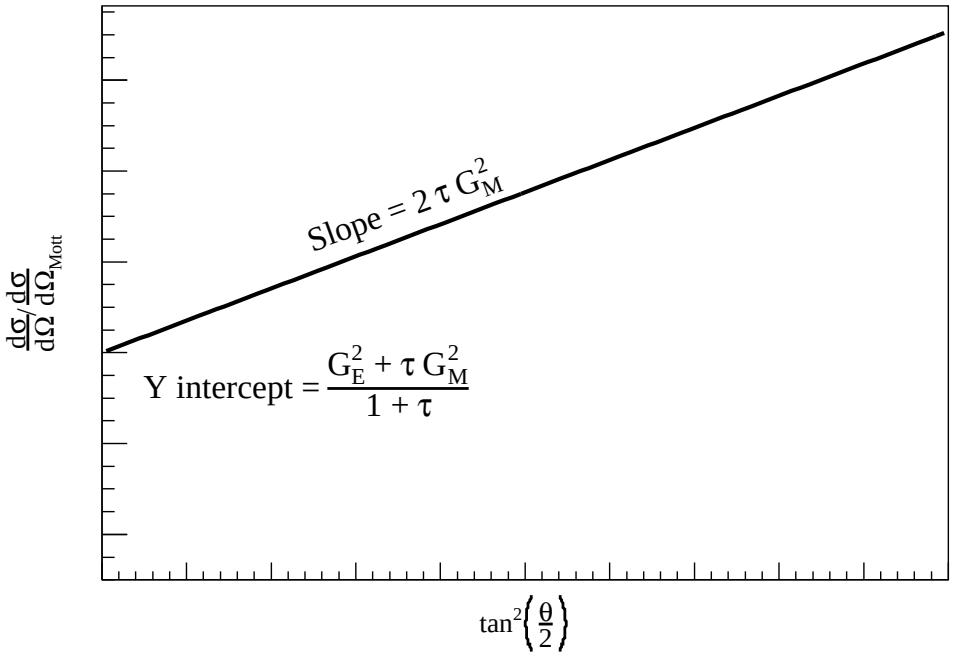

FIG. 2.3: *Rosenbluth plot showing the linear relationship between* $(d\sigma/d\Omega)/(d\sigma/d\Omega)_{Mott}$ *and* $tan^2(\theta/2)$ *at a fixed value of* Q^2.

The proton form factors G_E^p and G_M^p have been determined by the Rosenbluth separation up to $Q^2 \sim 9$ (GeV/c)^2 [18–21]. Empirically both G_E^p and G_M^p approximately follow the so-called empirical dipole form (see Figure 2.4)

$$G_E^p \simeq G_D = \left(1 + \frac{Q^2}{0.71\,(\mathrm{GeV/c})^2}\right)^{-2} \tag{2.11}$$

$$G_M^p \simeq \mu_p G_D \tag{2.12}$$

Besides the Rosenbluth separation, another experimental technique used to

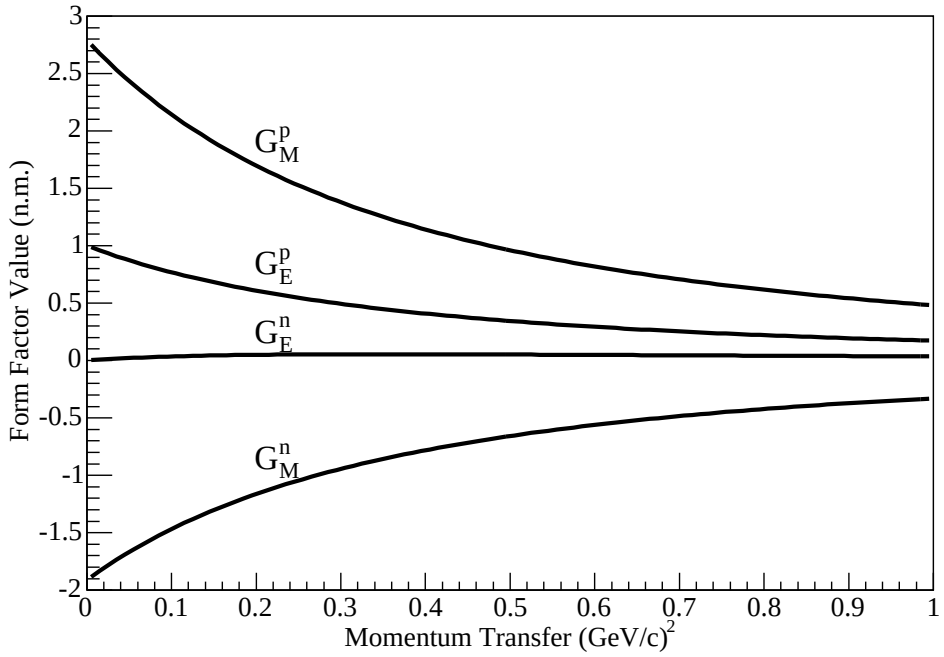

FIG. 2.4: *Plot of the dipole parameterizations of G_M^p, G_E^p, and G_M^n and the Galster parameterization of G_E^n.*

extract G_E^p is to measure the recoil polarization transfer in polarized electron-unpolarized proton scattering. This technique was originally suggested in the 1970's [22]. This polarization transfer method is less prone to some systematic uncertainties compared to the Rosenbluth separation. Considering only one-photon exchange, a polarized electron beam transfers its polarization to the recoil proton with two non-zero components, P_t, perpendicular to, and P_l, parallel to, the proton momentum in the scattering plane. These components are related to the electric and magnetic form factors

$$P_t \propto G_E^p G_M^p \quad \text{and} \quad P_l \propto G_M^{p2}. \tag{2.13}$$

Putting in the kinematical variables, the ratio G_E^p/G_M^p can be expressed as

$$\frac{G_E^p}{G_M^p} = -\frac{P_t}{P_l}\frac{(E_e + E_{e'})}{2M_p}\tan\left(\frac{\theta_e}{2}\right) \tag{2.14}$$

where E_e is the beam energy, $E_{e'}$ is the scattered electron energy, M_p is the proton mass and θ_e is the angle of the scattered electron.

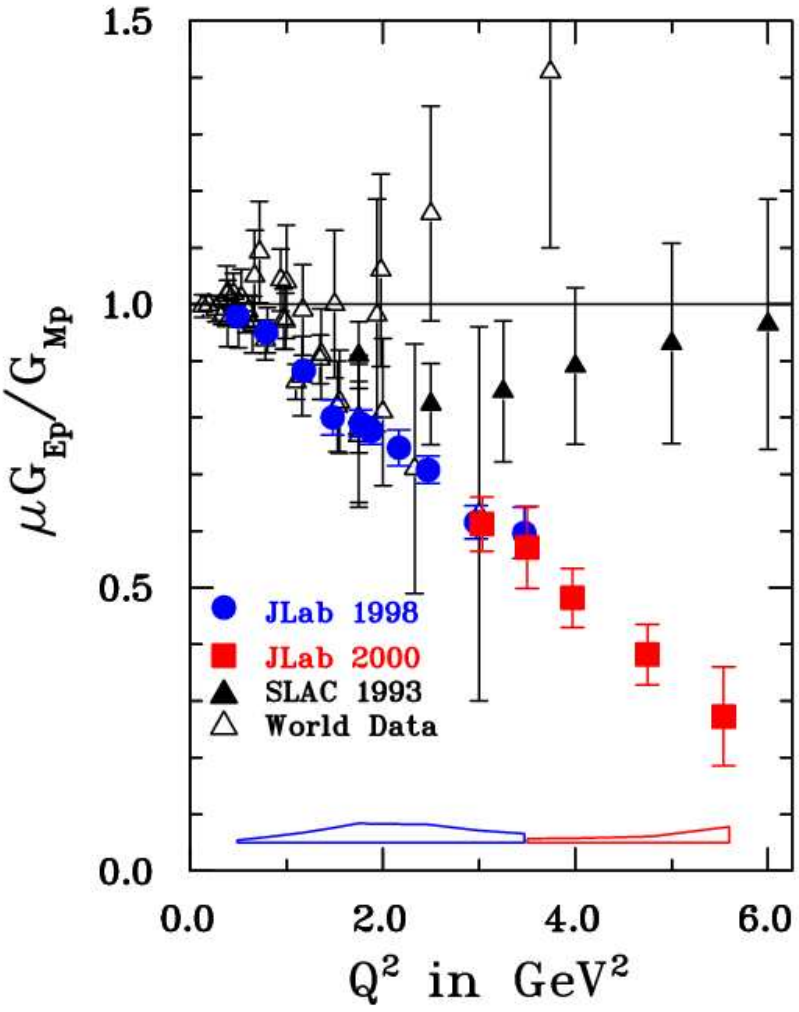

FIG. 2.5: *Plot of $\mu_p G_E^p/G_M^p$ vs. Q^2 for Rosenbluth separation technique (triangle symbols) [23–28], and polarization transfer measurements (blue circles and red squares) [30, 31] results. The systematic uncertainties of the JLab data are shown at the bottom of the plot.*

Surprisingly, the results from these polarization transfer experiments [29–31] disagree with the Rosenbluth separation [23–28] as shown in Figure 2.5, especially for Q^2 larger than 1.0 (GeV/c)^2. At low Q^2, $\frac{G_E^p}{G_M^p} \sim 1$ as measured with both

techniques, but the ratio falls with increasing Q^2 using the polarization transfer data. Theoretical work is ongoing to understand the source of this discrepancy [32, 33]. Since G^0 operates at momentum transfers less than 1.0 $(\mathrm{GeV/c})^2$ this discrepancy should have little effect.

The neutron form factors are defined in an analogous way. They are more difficult to measure since there are no free neutron targets. Typically deuterium and helium targets in quasi-elastic scattering are used and the theoretical and/or measured proton contribution is subtracted off. G_M^n can be parameterized as (see Figure 2.4)

$$G_M^n \simeq \mu_n G_D \tag{2.15}$$

where μ_n is the neutron's magnetic moment. G_E^n is a more difficult situation since the neutron's net electric charge is zero. Therefore, in the static limit, $G_E^n(Q^2 \to 0) = 0$. The small value of G_E^n at $Q^2 = 0$ compared to G_M^n makes the Rosenbluth separation [34] challenging for the neutron. It has been found that G_E^n is approximated by the so-called Galster parameterization [35] (see Figure 2.4)

$$G_E^n = \frac{-\mu_n \tau G_D}{1 + 5.6\tau}. \tag{2.16}$$

Recent experiments using recoil polarimetry [36–38] and polarization transfer [39–41] with light nuclei in quasi-elastic scattering have been employed to measure G_E^n without using the Rosenbluth separation. Interference between the magnetic and electric scattering amplitudes produces an asymmetry that can be measured and related to a ratio of G_E^n and G_M^n. These techniques have several advantages, one of the most important being that many of the systematic errors cancel in these ratios. Comparing the Rosenbluth results and these recent experiments, they seem to be in agreement.

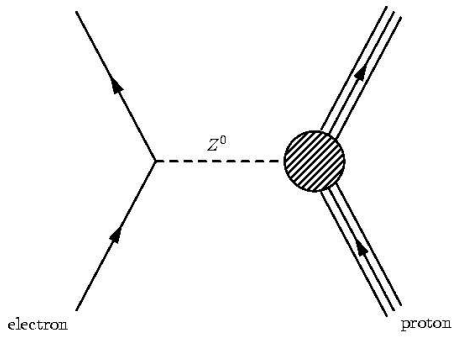

FIG. 2.6: *Tree level Feynman diagram for electron-proton weak neutral current scattering.*

2.3 Weak Neutral Form Factors

Besides electromagnetic scattering via the photon exchange, electron-nucleon scattering has a mixture component that can occur via the weak neutral current interaction (see Figure 2.6). The scattering amplitude is

$$\mathcal{M}_Z = \frac{G_F}{\sqrt{2}} j^{Z\mu} J^Z_\mu. \tag{2.17}$$

Since the weak interaction is a V-A theory [42], the proton current is more complicated than the electromagnetic case. It is given by:

$$J^Z_\mu = \bar{u}\left[\gamma_\mu F_1^Z + i\frac{\sigma_{\mu\nu}q^\nu}{2M_p}F_2^Z + \gamma_\mu\gamma_5 G_A^e\right]u. \tag{2.18}$$

The weak neutral form factors F_1^Z and F_2^Z are analogous to the electromagnetic form factors F_1^γ and F_2^γ. Besides the vector form factors, in weak scattering there is also an axial contribution, represented by the electron-nucleon axial vector form factor, (G_A^Z). This form factor can be written in general as (see Figure 2.7)

$$G_A^e = G_A^Z + \eta F_A + R_A^e \tag{2.19}$$

where

$$G_A^Z = -\tau_3 G_A + G_A^s \tag{2.20}$$

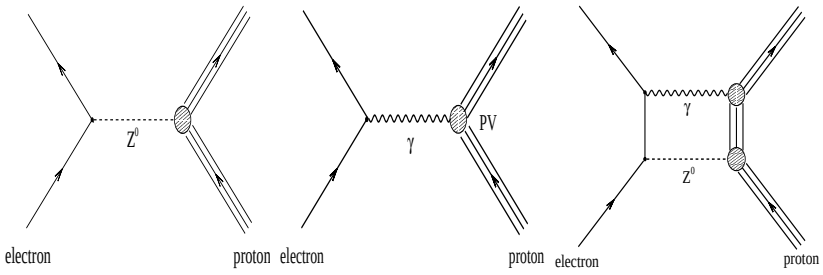

FIG. 2.7: *Feynman diagrams for contributions to the electron-nucleon axial coupling. The first diagram describes a single Z^0 exchange. The second diagram describes the parity-violating photon exchange which contributes to the nucleon anapole moment. The third diagram is an example of radiative corrections that must be taken into account.*

corresponding to the weak axial form factor associated with Z^0 exchange. It is measured at $Q^2 = 0$ in neutron beta decay with a value of $G_A(0) = 1.2601 \pm 0.0028$ [43], and its Q^2 dependence is measured in neutrino-proton scattering [44]. The strangeness portion, $G_A^s(Q^2)$ is measured at $Q^2 = 0$ in deep inelastic scattering [45]. F_A is the nucleon anapole moment which describes the parity-violating coupling of the photon to the nucleon. This term is enhanced by a factor

$$\eta = \frac{8\pi\sqrt{2}\alpha}{1 - 4\sin^2\theta_W} \tag{2.21}$$

where θ_W [43] is the weak mixing angle. This coupling can occur when two quarks in the proton interact weakly while interacting with the scattered photon. This term is unique to parity-violating interactions with charged particles such as electrons. R_A^e represents the radiative corrections that have been folded into G_A^e.

2.4 G_M^S, G_E^S and G^0: Quark Decomposition of Form Factors

It is possible to decompose the electromagnetic and neutral weak form factors in terms of individual quark flavors. In this way the strange quark content of the nucleon can be isolated.

The SU(3) flavor decomposition (that is working with the u, d, and s quark basis) of the proton electromagnetic form factors can be written for each form factor. This is the sum of the individual quark flavor form factors weighted by the electromagnetic charge of that flavor quark

$$G_E^{\gamma,p} = \frac{2}{3}G_E^u - \frac{1}{3}G_E^d - \frac{1}{3}G_E^s \tag{2.22}$$

$$G_M^{\gamma,p} = \frac{2}{3}G_M^u - \frac{1}{3}G_M^d - \frac{1}{3}G_M^s. \tag{2.23}$$

By analogy the same can be done for the weak form factors, but this time the quark flavor form factors are weighted by the weak charge of that flavor quark:

$$G_E^Z = \left(1 - \frac{8}{3}\sin^2\theta_W\right) G_E^u + \left(-1 + \frac{4}{3}\sin^2\theta_W\right) G_E^d + \left(-1 + \frac{4}{3}\sin^2\theta_W\right) G_E^s \tag{2.24}$$

$$G_M^Z = \left(1 - \frac{8}{3}\sin^2\theta_W\right) G_M^u + \left(-1 + \frac{4}{3}\sin^2\theta_W\right) G_M^d + \left(-1 + \frac{4}{3}\sin^2\theta_W\right) G_M^s \tag{2.25}$$

where the parameter $\sin^2(\theta_W)$ is known with a high degree of accuracy. Its on-shell value is given by [43]:

$$\sin^2(\theta_W) = 0.23117 \pm 0.00016. \tag{2.26}$$

Assuming charge symmetry between the up and down quarks in the neutron and proton:

$$G_E^{u,p} = G_E^{d,n} \qquad G_M^{u,p} = G_M^{d,n} \tag{2.27}$$

$$G_E^{d,p} = G_E^{u,n} \qquad G_M^{d,p} = G_M^{u,n} \tag{2.28}$$

allows for the u and d quark contributions to be eliminated. The weak form factors can then be written as

$$G_{E,M}^{Z,p} = (1 - 4\sin^2\theta_W)G_{E,M}^{\gamma,p} - G_{E,M}^{\gamma,n} - G_{E,M}^s \tag{2.29}$$

solving for $G_{E,M}^s$ yields

$$G_{E,M}^s = (1 - 4\sin^2\theta_W)G_{E,M}^{\gamma,p} - G_{E,M}^{\gamma,n} - G_{E,M}^{Z,p}. \tag{2.30}$$

In the $Q^2 = 0$ limit, one may assume that

$$G_M^s = \mu_s \tag{2.31}$$

$$G_E^s = 0 \tag{2.32}$$

where μ_s is the strange magnetic moment of the nucleon in terms of the nuclear magneton. Relation 2.32 follows from the fact that the nucleon has no net strangeness.

Strange quarks could contribute to G_E^p and/or G_M^p. In order to contribute to the charge form factor, there must be a spatial polarization between strange and anti-strange quarks. In order to contribute to the magnetic form factor, the strange and anti-strange quarks must have spatial distribution of angular momenta.

An alternative formulation is found, again, by considering only SU(3) flavors, which allows one to write an expression for the SU(3) flavor singlet form factor $G_{E,M}^0$ (and hence the name of this experiment). This form factor characterizes the difference between the corresponding electromagnetic and weak form factors for the nucleon. In terms of the proton form factors

$$G_{E,M}^{0,p} = 4\left[\left(\frac{1}{2} - \sin^2\theta_W\right) G_{E,M}^{p,\gamma} - G_{E,M}^{p,Z}\right]. \tag{2.33}$$

This can be written in terms of the quark flavors

$$G_{E,M}^{0,p} = \frac{1}{3}\left[G_{E,M}^{u,p} + G_{E,M}^{d,p} + G_{E,M}^{s,p}\right]. \tag{2.34}$$

It should be noted that the charge symmetry assumption (see Equations 2.27 and 2.28) between the up and down quarks in the neutron and the proton demands a closer look. Under this charge symmetry, the up and down quark wave functions in the proton describe the down and up quark wavefunctions in the neutron. This charge symmetry is broken by the mass differences between the up and down quarks and from electromagnetic effects. This charge symmetry breaking manifests itself as an additive term to Equation 2.29

$$G_{E,M}^{Z,p} = (1 - 4\sin^2\theta_W)G_{E,M}^{\gamma,p} - G_{E,M}^{\gamma,n} - G_{E,M}^s - G_{E,M}^{u,d}. \tag{2.35}$$

The effects of $G_{E,M}^{u,d}$ along with any possible Q^2 dependence has been investigated using non-relativistic quark models [46]. In these non-relativistic quark models, the largest effect has been calculated to alter the values of the electromagnetic form factors by less than 1%.

2.5 Elastic Parity-Violating Electron-Nucleon Scattering

In order to measure the strange electric and magnetic form factors of the proton it is necessary to measure the weak neutral form factors. Since the electromagnetic interaction dominates over the weak interaction, direct measurement of the weak neutral form factors is challenging. In order to observe the weak neutral form factors parity-violating electron-nucleon scattering may be employed.

In elastic electron-nucleon scattering, polarized electrons are scattered off of the unpolarized nucleon. A polarized electron can come in two states: right handed electrons (denoted by a '+' or 'r') are electrons whose spin and momentum vectors are parallel and left handed electrons (denoted by a '-' or 'l') are electrons whose spins and momentum vectors are anti-parallel. The scattering interaction can occur via the exchange of a virtual photon or a virtual Z^0. This gives rise to two scattering amplitudes, $\mathcal{M}_Z$ and $\mathcal{M}_\gamma$. The total scattering amplitude, $\mathcal{M}$, is given by

$$\mathcal{M} = \mathcal{M}_\gamma + \mathcal{M}_Z. \tag{2.36}$$

The cross section is proportional to the square of the scattering amplitude

$$|\mathcal{M}^2| = |\mathcal{M}_\gamma^2| + 2\mathrm{Re}\{(\mathcal{M}_\gamma)^* \mathcal{M}_Z\} + |\mathcal{M}_Z^2|. \tag{2.37}$$

The weak interaction violates parity. A parity transformation involves an inversion of a physical system through the origin of coordinates. The handedness of a particle,

the relative orientation of its momentum and spin, reverses under mirror reflections. Since the weak interaction violates parity, its scattering amplitude, M_Z, will be different for scattering of left or right-handed electrons. An asymmetry, A, can be formed by taking the difference over the sum of helicity dependent scattering cross sections, σ_R and σ_L

$$A = \frac{\sigma_R - \sigma_L}{\sigma_R + \sigma_L}. \tag{2.38}$$

Writing in terms of the helicity-dependent scattering amplitudes gives:

$$A = \frac{|\mathcal{M}_\gamma + \mathcal{M}_Z|^2_R - |\mathcal{M}_\gamma + \mathcal{M}_Z|^2_L}{|\mathcal{M}_\gamma + \mathcal{M}_Z|^2_R + |\mathcal{M}_\gamma + \mathcal{M}_Z|^2_L} \tag{2.39}$$

$$= 2\frac{\mathcal{M}^*_\gamma \mathcal{M}_Z}{|\mathcal{M}_\gamma|^2}. \tag{2.40}$$

Using Equations 2.5 and 2.17 in Equation 2.40 yields

$$A = \left(\frac{-G_F Q^2}{4\sqrt{2}\pi\alpha}\right) \frac{\epsilon G_E^{\gamma,p} G_E^{Z,p} + \tau G_M^{\gamma,p} G_M^{Z,p} - \frac{1}{2}(1 - 4\sin^2\theta_W)\epsilon' G_M^{\gamma,p} G_A^e}{\epsilon (G_E^{\gamma,p})^2 + (G_M^{\gamma,p})^2} \tag{2.41}$$

where

$$\epsilon = \frac{1}{1 + 2(1+\tau)\tan^2(\frac{\theta}{2})} \tag{2.42}$$

$$\epsilon' = \sqrt{\tau(1+\tau)(1-\epsilon^2)}. \tag{2.43}$$

The electromagnetic nucleon form factors have been measured and are fairly well known (see Section 2.2) and these values can be used as inputs in the above equation. Measurements of different linear combinations of weak neutral form factors must be done. By selecting different kinematics, one is able to access different combinations of weak neutral form factors. Three independent measurements are needed for a complete determination of the three weak form factors: $G_M^{Z,p}$, $G_E^{Z,p}$, and G_A^e. This can be done by varying the kinematical variables ϵ and ϵ' at a fixed Q^2 (similar to Figure 2.3). Forward angle measurements correspond to large ϵ and small ϵ' while backward angle measurements are most sensitive to large ϵ' and small ϵ. Note

that the axial term is suppressed relative to the vector electric and magnetic terms because of the factor $(1 - 4\sin^2\theta_W) \approx 0.08$. For the third measurement to get to G_A^e, it appears most effective to measure the asymmetry in quasi-elastic scattering off of deuterium.

In this quasi-elastic scattering off of deuterium, the impulse approximation can be used. This approximation is one in which the deuteron as a whole is described as a linear superposition of the single nucleon observables. This allows one to write the asymmetry as

$$A_{QE} = \frac{\sigma_p A_p + \sigma_n A_n}{\sigma_d} \tag{2.44}$$

where $\sigma_{p(n)}$ is the cross-section for elastic e-p(n) scattering, $\sigma_d = \sigma_p + \sigma_n$, the asymmetry on the proton A_p is given by Equation 2.41 and the asymmetry on the neutron is given by

$$A_n = \left(\frac{-G_F Q^2}{4\sqrt{2}\pi\alpha}\right) \frac{\epsilon G_E^{\gamma,n} G_E^{Z,n} + \tau G_M^{\gamma,n} G_M^{Z,n} - \frac{1}{2}(1 - 4\sin^2\theta_W)\epsilon' G_M^{\gamma,n} G_A^{Z,n}}{\epsilon (G_E^{\gamma,n})^2 + (G_M^{\gamma,n})^2}. \tag{2.45}$$

Effects associated with the deuteron wave function and different potential models have been explored in [47] and were shown to be quite small. Corrections for final state interactions and exchange currents must be taken into account for a reliable separation of the axial and magnetic form factors. These issues have been addressed in [48].

2.6 Strange Form Factors and Physics Asymmetry

Using Equations 2.41 and 2.29, the parity-violating asymmetry, to leading order, can be written in terms of strange (unknown), axial (unknown), proton (known)

and neutron (known) form factors. This asymmetry equation can be written as

$$\begin{aligned} A &= \left(\frac{-G_F Q^2}{4\sqrt{2}\pi\alpha}\right)\frac{1}{\epsilon(G^{\gamma,p})^2_E + \tau(G^{\gamma,p}_M)^2} \\ &\times \epsilon G^{\gamma,p}_E[(1-4\sin^2\theta_W)G^{\gamma,p}_E - G^{\gamma,n}_E] + \tau G^{\gamma,p}_M[(1-4\sin^2\theta_W)G^{\gamma,p}_M \\ &- G^{\gamma,n}_M] - (1-4\sin^2\theta_W)\epsilon' G^{\gamma,p}_M G^{ep}_A + G^{\gamma,p}_E G^s_E + \tau G^{\gamma,p}_M G^s_M. \end{aligned} \tag{2.46}$$

It is useful to write Equation 2.46 as a combination of the three unknowns, G^s_E, G^s_M, and G^e_A:

$$A = \eta + \xi G^s_E + \chi G^s_M + \psi G^e_A \tag{2.47}$$

where

$$\begin{aligned} \eta &= \left(\frac{-G_F Q^2}{4\sqrt{2}\pi\alpha}\right)\frac{1}{\epsilon(G^{\gamma,p})^2 + \tau(G^{\gamma,p}_M)^2}\epsilon G^{\gamma,p}_E((1-4\sin^2\theta_W)G^{\gamma,p}_E - G^{\gamma,n}_E) \\ &+ \tau G^{\gamma,p}_M((1-4\sin^2\theta_W)G^{\gamma,p}_M - G^{\gamma,n}_M) \end{aligned} \tag{2.48}$$

$$\xi = \left(\frac{-G_F Q^2}{4\sqrt{2}\pi\alpha}\right)\frac{\epsilon G^{\gamma,p}_E}{\epsilon(G^{\gamma,p})^2 + \tau(G^{\gamma,p}_M)^2} \tag{2.49}$$

$$\chi = \left(\frac{-G_F Q^2}{4\sqrt{2}\pi\alpha}\right)\frac{\tau G^{\gamma,p}_M}{\epsilon(G^{\gamma,p})^2 + \tau(G^{\gamma,p}_M)^2} \tag{2.50}$$

$$\psi = \left(\frac{-G_F Q^2}{4\sqrt{2}\pi\alpha}\right)\frac{(1-4\sin^2\theta_W)\epsilon' G^{\gamma,p}}{\epsilon(G^{\gamma,p})^2 + \tau(G^{\gamma,p}_M)^2}. \tag{2.51}$$

From Equations 2.48 and 2.51, there is expected to be a non-zero asymmetry, even if the strange quarks do not contribute to the properties of the nucleon. This non-strange quark asymmetry is determined by the non-strange electric, magnetic, and axial form factors of the nucleon and by the electroweak parameter $\sin^2(\theta_W)$.

2.7 Survey of Previous Experiments

HAPPEX I [14] was an experiment that ran in 1998 and 1999 at Jefferson Lab. It measured the parity-violating electroweak asymmetry in elastic electron-proton scattering. In order to be most sensitive to the strange electric form factor G^S_E,

kinematics of $\theta = 12.3^\circ$ and Q^2=0.477 (GeV/c)^2 were used. A 3.36 GeV polarized electron beam scattered off an unpolarized 15 cm long liquid hydrogen target. In the first run, the beam current was 100 μA with an average beam polarization of 38.8 $\pm$ 2.7% from a bulk GaAs polarized source. In the second run, the beam current was 35 μA with a beam polarization of about 70% from a "strained" GaAs polarized source. A Compton polarimeter was used to continuously measure the beam polarization. Two spectrometers in Hall A with a small acceptance $\Delta\Omega = 5.5$ msr detected the scattered electrons at this extreme forward angle. The detected signals were integrated from a lead/lucite scintillator calorimeter which only accepted elastically scattered particles. The measured asymmetry was $A = -15.05 \pm 0.98(stat) \pm 0.56(syst)$ ppm. Due to limited kinematics, HAPPEX I was unable to perform the Rosenbluth separation to disentangle G_E^S and G_M^S. Thus HAPPEX I effectively measured a combination of strange electric and magnetic form factors at their kinematics of

$$G_E^S + 0.39 G_M^S = 0.014 \pm 0.020 \pm 0.010 \tag{2.52}$$

which is consistent with zero contribution of strange quarks, or a cancellation by G_E^S and G_M^S at these kinematics.

The SAMPLE experiment [13] was performed at the Bates Linear Accelerator Center in 1995-1999. It measured the parity-violating asymmetry in elastic scattering of polarized 200 MeV electrons from a 40 cm long unpolarized hydrogen (deuterium) target. The beam polarization was about 37% from a bulk GaAs polarized electron source. The scattered electrons were detected in a large solid angle of approximately $\Delta\Omega \approx 1.5$ sr using air Cerenkov detector at backward angles of 130° to 170°. Since measurements were made at backward angles, the asymmetry is most sensitive to G_M^s and G_A^e. The scattered electrons with an average $Q^2 \sim 0.1$ (GeV/c)^2 were detected by Cerenkov light produced in air absorbed by ten photomultiplier tubes via ten mirrors positioned around the beam axis. The measured

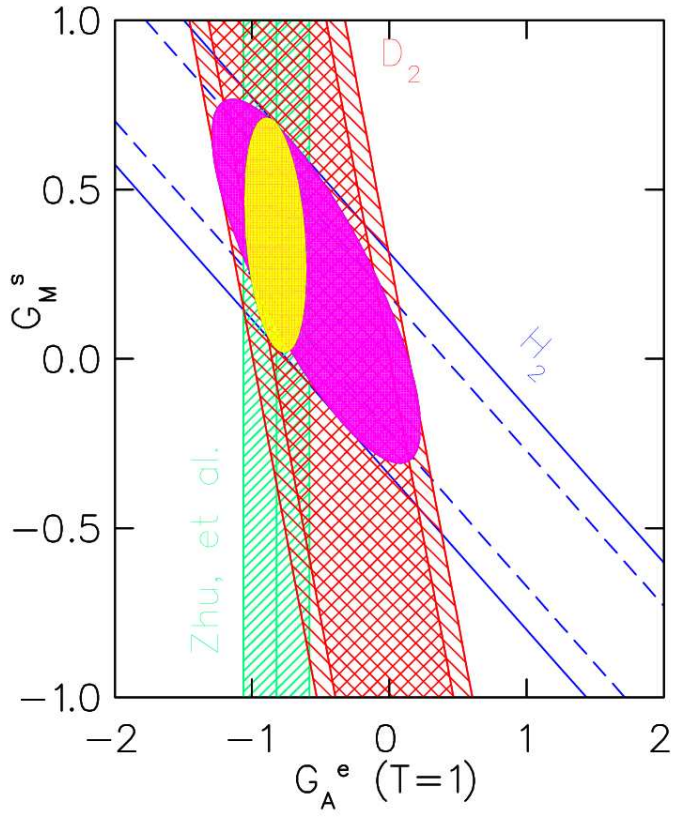

FIG. 2.8: *SAMPLE uncertainty bands of G_M^s vs. G_E^s at $Q^2 = 0.1$ (GeV/c)^2. Also shown is the uncertainty in a theoretical calculation of G_A^e by Zhu [49] at the same momentum transfer. The smaller ellipse (yellow) corresponds to a 1σ overlap between the SAMPLE results on hydrogen and the theoretical calculation. The larger ellipse (magenta) corresponds to a one sigma overlap between the SAMPLE hydrogen and deuterium results.*

asymmetry for the proton was $A = -5.61 \pm 0.67 \pm 0.88$ ppm. Making measurements on both hydrogen and deuterium allowed the SAMPLE collaboration to measure the electron-proton axial form factor, $G_A^e = -0.83 \pm 0.26$. This in turn, at the SAMPLE kinematics, allows one to isolate the strange magnetic form factor. The strange magnetic form factor was found to be

$$G_M^s(Q^2 = 0.1) = 0.37 \pm 0.20(stat) \pm 0.26(syst) \pm 0.07(theory) \qquad (2.53)$$

which is consistent with zero.

Using Chiral Perturbation Theory [50] to extrapolate to $Q^2 = 0$ yields a con-

tribution to the magnetic moment due to strange quarks:

$$\mu_s = 0.37 \pm 0.20 \pm 0.26 \pm 0.15. \tag{2.54}$$

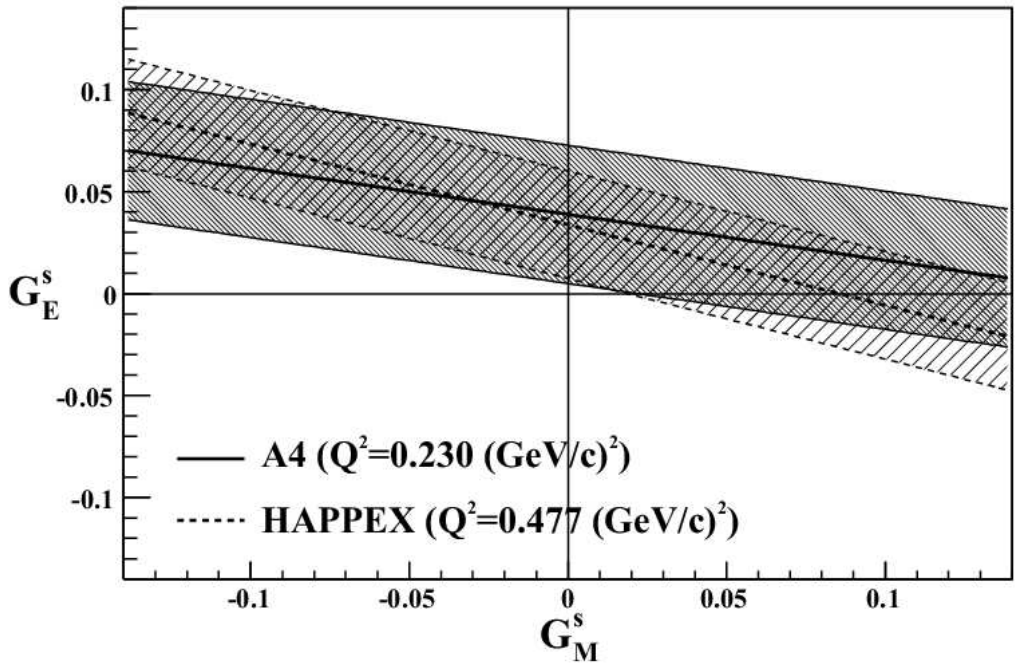

FIG. 2.9: *The PVA4 (represented as 'A4' in the plot) results are shown as a solid line representing all possible combinations of* $G_E^s + 0.225 G_M^s$ *at* $Q^2 = 0.230$ *(GeV/c)*^{2}*. The densely hatched region represents the PVA4 uncertainty. The HAPPEX result is shown as a dashed line representing all possible combinations of* $G_E^s + 0.395 G_M^s$ *at* $Q^2 = 0.477$ *(GeV/c)*^{2}*. The less densely hatched region represents the HAPPEX uncertainty.*

The PVA4 experiment [51] was performed at MAMI at Mainz. It measured the parity-violating asymmetry in elastic scattering of 854.3 MeV polarized electrons from an unpolarized hydrogen target at a Q^2 of 0.230 (GeV/c)^2. The scattered electrons between 30° and 40° were detected by a large acceptance ($\Delta\Omega$ = 0.62 sr) calorimeter. This calorimeter consists of 512 PbF_2 crystals. The beam current was 20 μA with a polarization of about 80% produced using a "strained" GaAs polarized electron source. The polarization was measured by both Compton and

Moller polarimeters. The measured asymmetry was $A = -5.44 \pm 0.54(stat) \pm 0.26(syst)$. The extracted linear combination of the strange and magnetic form factors was found to be

$$G_E^s + 0.225 G_M^s = 0.039 \pm 0.034. \tag{2.55}$$

This result is 1.2σ away from zero. It should be noted, *with caution*, that [51] averages the PVA4 result (Q^2=0.230 (GeV/c)^2) with the HAPPEX result (Q^2=0.477 (GeV/c)^2) at different kinematics. They use a value for G_M^s based on theoretical estimates and SAMPLE's result to obtain $G_M^s(0.1 < Q^2 < 0.5\ (\mathrm{GeV/c})^2) = 0.066 \pm 0.26$ which leads to a non-zero contribution of strange quarks to the strange electric form factor.

CHAPTER 3

Experimental Apparatus

The G^0 engineering run was performed in Hall C at Jefferson Lab in the Fall of 2002 through January 2003. A second engineering run is scheduled for the Fall 2003 with the forward production run occurring in early 2004. This chapter will describe the G^0 spectrometer, Jefferson Lab's electron accelerator, the G^0 beam structure, and polarimetry.

3.1 The G^0 Magnet

The superconducting magnet system (SMS) is the largest component of the G^0 apparatus. The purpose of the magnet is to bend elastically charged particles from the target of the same momentum onto the focal plane detectors, independently of the interaction point along the target length (see Figure 3.1). The magnet produces, at a maximum, a 1.6 T·m field. This toroidal magnet consists of 8 superconducting coils in a single cryostat. Each coil is made from 144 turns of integrated superconductor. The superconducting coils in series are cooled by four parallel liquid helium convection circuits. Two additional parallel cooling paths are used to cool the superconducting electrical buss through which power is supplied to the coils. The

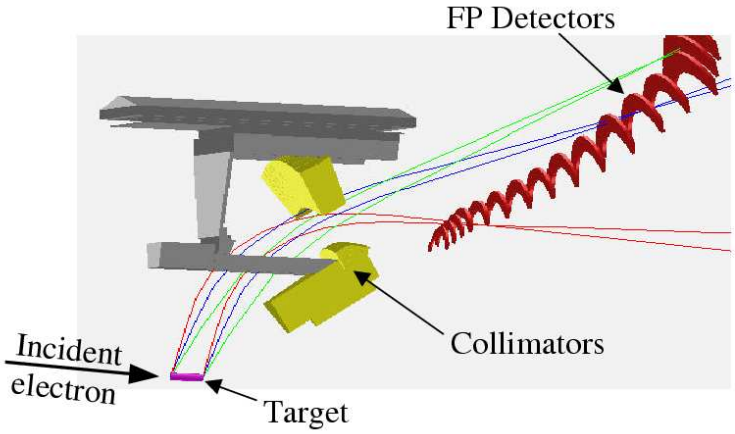

FIG. 3.1: *Elastically scattered protons, of the same momentum, are focused onto the Focal Plane Detectors (FPD). This is independent of where along the target the scattering occurs. This is shown schematically by looking at three different momentum values (denoted by red, green, and blue) at opposite ends of the target being focused on the detectors. The collimators are used to reduce the background and to set the acceptance of the detectors.*

coils, electrical buss, and collimators (which define the spectrometer acceptance and provide shielding for the target and detectors) make up what is called the cold mass. This sits inside a stainless steel shell and makes up the bulk of the magnet. A liquid nitrogen shield surrounds the cold mass. The cryogens, lN_2 and lHe are fed into the magnet via a manifold at the bottom of the magnet from reservoirs located in the control dewar at the top of the magnet. The cryogens percolate back up to the reservoirs through the cooling circuit, losing density and absorbing power along the way. Aluminum end caps cover both the front and back of the main shell that houses the cold mass. There are eight trapezoidal holes, 0.51 m^2 in area, on the downstream end cap that are covered by an 0.020 inch titanium plate. These are the exit windows that provide a path of low energy loss and multiple scattering from particles emanating from the target to the detectors. Mounted to the beam line at the upstream magnet end cap is the target service module that contains the target and its positioning mechanism. Valves are connected upstream of the target service

module and at the downstream end of the exit beam line to be isolated. When these valves are closed, the entire experimental apparatus can be disconnected and moved to the left of the beam line. This is necessary since the G^0 experimental program will take several years to complete and will not be the only experiment running in Hall C, thus the G^0 apparatus must be able to be removed from the Hall C beam line.

3.2 The G^0 Hydrogen Target

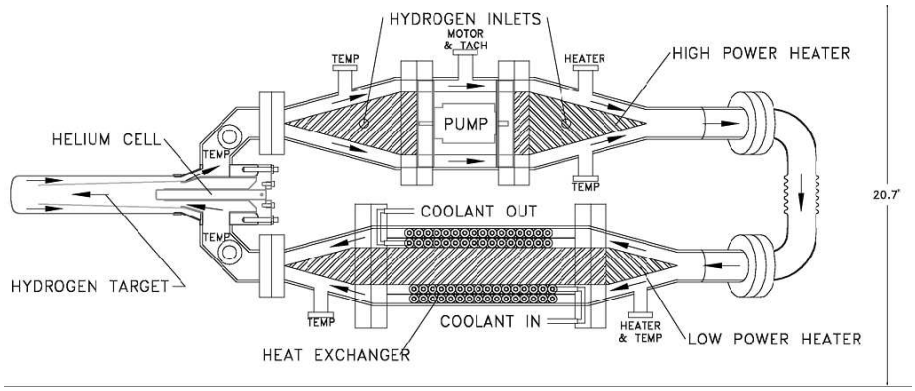

FIG. 3.2: *A schematic of the G^0 target. The G^0 target has been designed to minimize false asymmetries. The target cell is 20 cm long and filled with liquid hydrogen. The target operates at 450 watts.*

The G^0 experiment uses a liquid hydrogen target (see Figure 3.2) based on the SAMPLE experiment's design [15]. The target is optimized to reduce energy loss along the scattered particles' path and to minimize density fluctuations, caused by up to 250 W of beam power deposited on the target. The target is connected to a cryogenic loop to recirculate and cool the liquid hydrogen. The target and cryogenic loop sit inside the 77K liquid nitrogen shield of the SMS. The hydrogen cell is 20 cm long and 5 cm in diameter. The radius of curvature of the endcap of the target is 7.6 cm. The outer wall and endcap are 7.0 $\pm$ 0.5 mils of aluminum. A manifold

inside the lH_2 cell has been designed to direct the fluid flow down the center of the target cell and back near the cell walls. The target is fronted by a helium cell that has two purposes.

- To first order, it eliminates variations in target thickness with beam position by matching the radius of curvature of the entrance and exit windows of the hydrogen cell.

- It extends the hydrogen cell beyond the part of the cryoloop which is not symmetric about the beam axis allowing the target-beam interaction region to be axially symmetric.

The heat exchanger uses gaseous helium with an inlet temperature of about 15 K and pressure of 20 atm, supplied by the Jefferson Lab End Station Refrigerator. With a beam current of 40 μA impinging on it, the target requires a flow of 17 g/s of 15 K coolant. The coolant flows inside the finned tube and liquid hydrogen flows over the fins on the outside of the tubing. The heat exchanger has 2 layers of finned tubing through which the liquid hydrogen flows in parallel. The heat exchanger removes about 450 W of heat from the target with 250 W coming from 40 μA beam heating, 100 W from the pump motor and 100 W from connections to the outside world.

Two internal heaters in the G^0 cryogenic target are used to maintain a constant heat load and/or temperature in the target. The high-power heater consists of three heater coils in parallel. The high-power heater is a feedback loop that reads a signal proportional to the beam current and calculates the heat load of the beam, and then changes the heater such that there is a constant heat load on the target and thus ensures a constant temperature in the cell and coolant loop. A second 80 W low-power heater works in parallel with the high-power heater to maintain constant target temperature against small time-dependent drifts from other heat

load sources (such as the motor, coolant inefficiencies and radiant heating). The

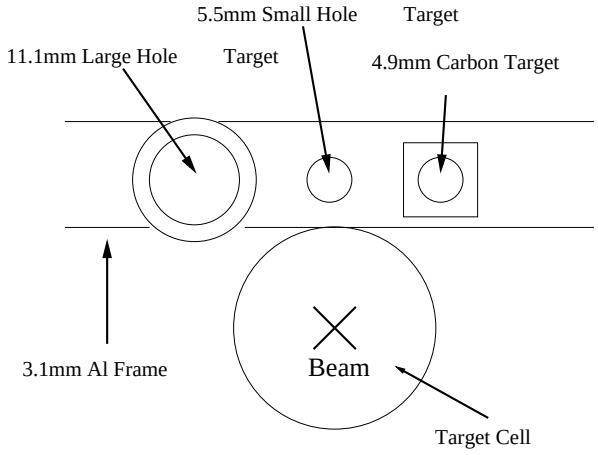

FIG. 3.3: *Schematic of the dummy target looking downstream of the beam. There are three dummy targets located above the target cell. Two of these dummy targets (large and small hole) are used in studying beam halo. The third dummy target is a ^{12}C radiator target.*

target is mounted onto an aluminum frame that is 3.05 mm thick. On this aluminum frame there are three dummy targets: two blank hole targets for studying beam halo and one ^{12}C target (see Figure 3.3). The big hole target has an inner diameter the same as the hydrogen target but with an outer diameter of 19.05 mm and a thickness of 3.912 mm to match the radiation length of 1 inch of aluminum. The small hole is 5.46 mm diameter. The ^{12}C target sits behind a hole of 9.562 mm diameter in the aluminum frame. Five slabs of $\sim$ 1 mm thick carbon make up the 4.9 mm thick ^{12}C target. The entire target can be removed from the beam trajectory for diagnostic purposes and can be warmed independently of the spectrometer.

One issue with the target that must be addressed in a parity-violation experiment is that of target boiling. If the target boils (e.g. density fluctuations due to a high amount of energy being deposited on the target by the electron beam) this will add noise to the experimental system. This noise will then increase the statistical error of the experiment. This additional noise from target boiling, (σ_b^2), is added in

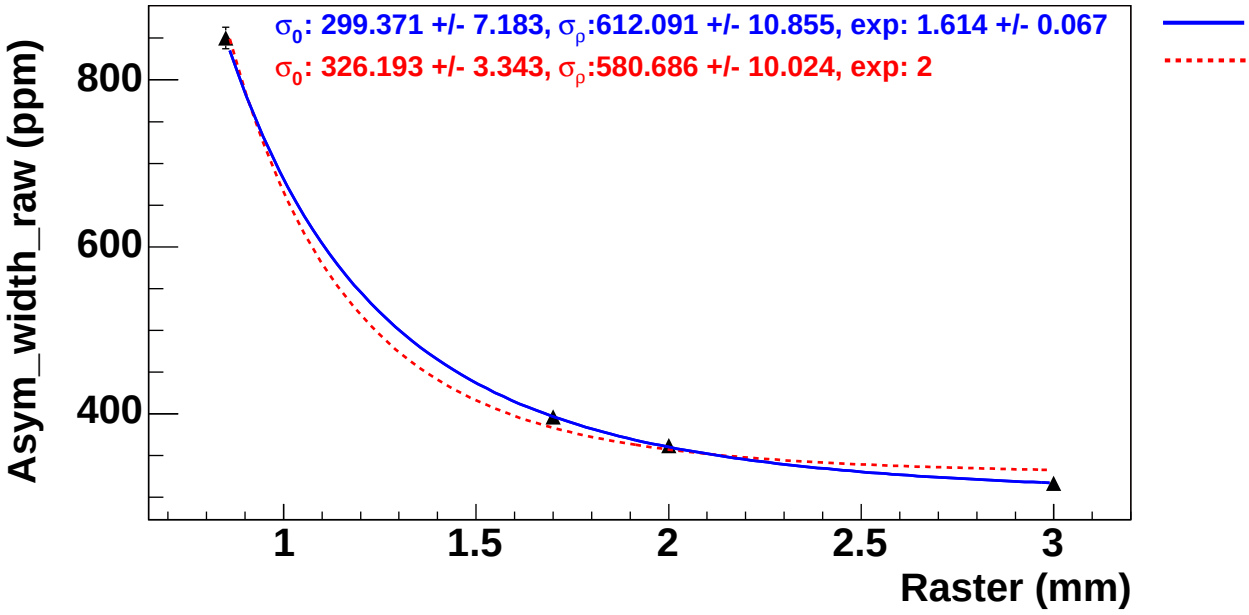

FIG. 3.4: *Fluctuations in the statistical width (ppm) as a function of raster size for target boiling studies. These data come from measurements with the LUMI detector.*

quadrature to the statistical width due to counting statistics, (σ_0^2):

$$\sigma^2 = \sigma_0^2 + \sigma_b^2 \tag{3.1}$$

where the overall statistical width is given by σ^2. The beam's noise σ_b^2 is parameterized by $\frac{\sigma_\rho^2}{r^x}$ where r is the raster size and x is the exponent which can either be fixed at 2 or allowed to be variable. The LUMI monitors (see Section 3.7) are used to measure the target boiling because they are at extreme small angles relative to the beam line. This means that the LUMIs see an electroweak asymmetry of zero and their detected rate is very high allowing one to make faster measurements than with the Focal Plane Detectors. A test that is performed is to boil the target by depositing more energy on the target by changing the raster (area) of the electron beam (see Figure 3.2). The LUMIs are then used to measure the contribution to the statistical width from the target. Two separate fits were performed to the data and the noise contribution at the G^0 raster size of 3 mm was found to be about

300 ppm. This is small compared to the statistical width due to counting statistics (found to be about 1400 ppm averaged over all the detectors). Taking the ratio of the measured statistical width (σ_{meas}) compared to the statistical width from counting statistics (σ_{stat}) and using the fact that the noise contribution from the beam monitors and target are $\approx$ 300 ppm each:

$$\frac{\sigma_{meas}}{\sigma_{stat}} = \frac{\sqrt{1400^2 + 2 \times 300^2}}{1400} = 1.05. \tag{3.2}$$

This implies that the error has been increased by 5% past counting statistics (and thus the error is dominated by counting statistics).

3.3 The G^0 Detector

The G^0 detector system consists of eight octants surrounding the beam line (see Figure 3.5). Four octants were designed and mounted by French collaborators and four by North American collaborators (see Figure 3.6). Each octant encloses an array of 16 scintillator pairs along the focal plane of the G^0 magnet. Each end of a scintillator is coupled to a lightguide, at the end of each lightguide is a PMT. These detectors are named the focal plane detectors (FPDs). The FPDs are the only detectors necessary for the forward angle measurement in the G^0 experiment. In this configuration, the scintillators detect elastically recoiled protons. The output PMT signals are used to measure the Time-of-Flight of the particles between the target and the focal plane of the magnet, providing particle identification. Each scintillator provides a selection in momentum transfer (Q^2) which is supplemented by a selection on the Time-of-Flight necessary for particle identification.

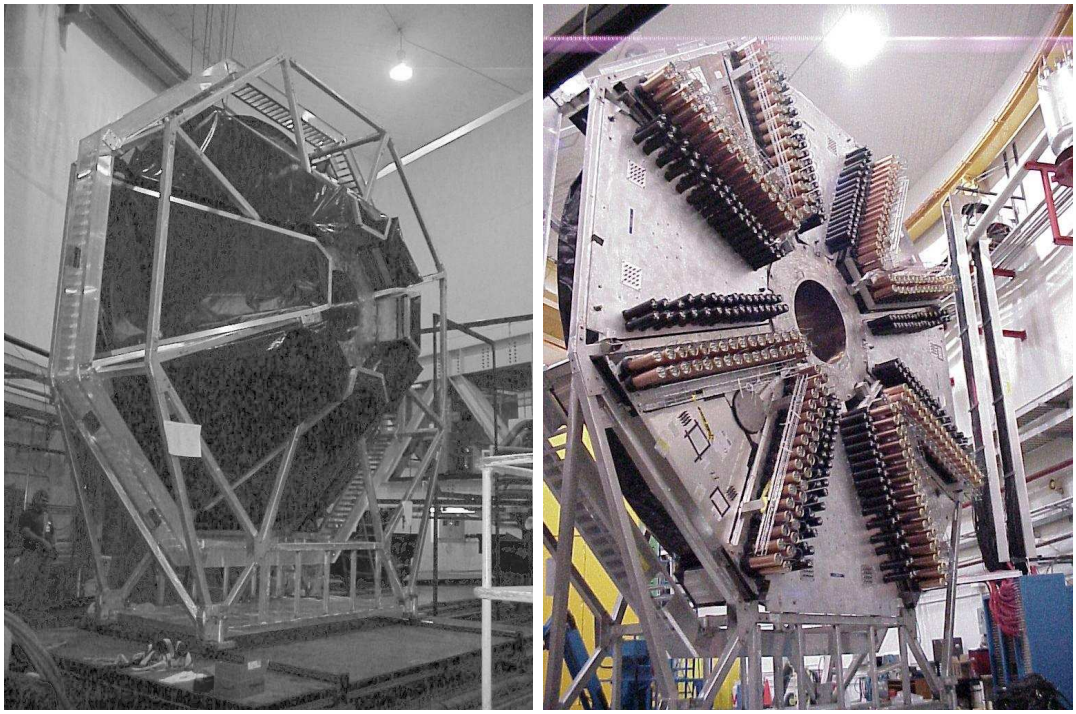

FIG. 3.5: *The G^0 detector system, supported by an aluminum support known as the 'Ferris Wheel', as seen upstream on the left picture and downstream on the right picture. The octants are numbered 1 though 8 starting from the top and moving clock-wise. Odd (even) numbered Octants are North American (French). The G^0 target and magnet are not pictured here; they were placed directly upstream of the Ferris Wheel.*

Detector System

An octant is an array of 16 BC408 Bicron scintillator pairs located at the focal plane of the G^0 magnet. They are labeled from 1 to 16 where the larger scintillator number corresponds to the scintillators located further away from the beam line and further from the target. Larger scintillator number also corresponds to the larger scintillator size and, in general, the larger measured value of Q^2 (with detectors 14 and 15 containing two Q^2 points and detector 16 containing no elastic Q^2 points so it is used to measure background). The FPDs have been divided into 16 detectors in order to keep the individual count rate for each detector around 1 MHz. The arc shape of the scintillator was defined to follow the iso-Q^2 phase space. The

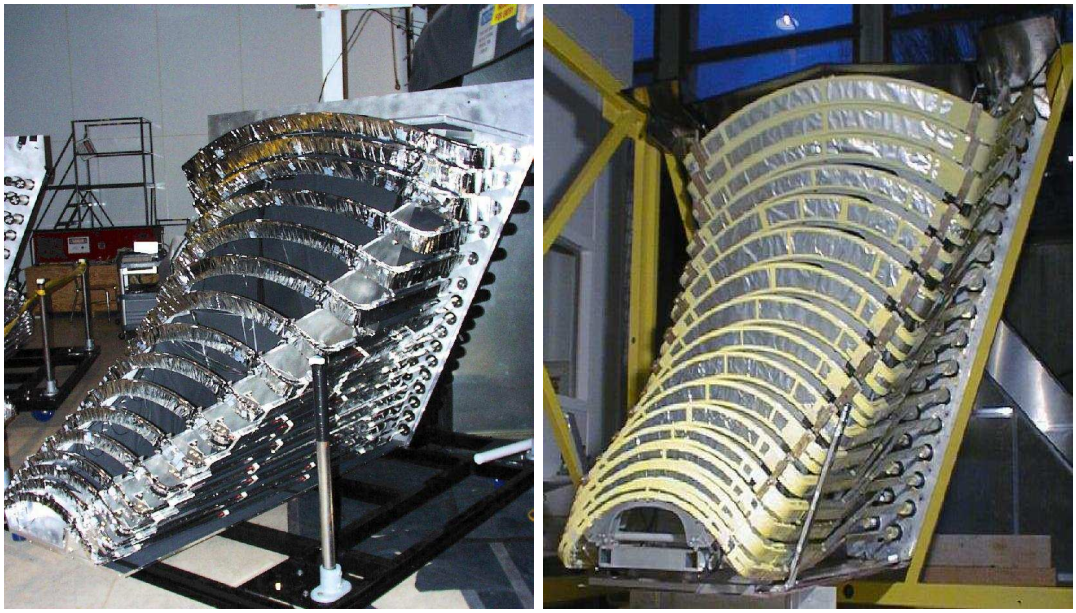

FIG. 3.6: *Pictured on the left is the North American Octant 7. On the right is pictured the French Octant 2. Both octants are shown without their light tight box.*

dimensions and areas of the scintillators are given in Table 3.1. The scintillators are paired together to increase background rejection, moreover two scintillators from the same pair are separated by a thin material (aluminum for French and polycarbonate for NA). Each FPD is a pair of two light pipes attached to the aluminum support of one octant. Each light pipe is the assembly of a scintillator and two light guides glued at each of the ends of the scintillator with photo-multiplier tubes attached to each end of the light guides. Optical fibers are air coupled to each end (right and left) of the scintillator. The fibers shine UV light to the scintillator and allow gain monitoring of the PMTs. The whole assembly is enclosed inside a light-tight box.

Further discussion of the calibration and testing of the NA detectors system can be found in Appendix C.

Scintillator	1	2	3	4	5	6
Length (cm)	60.1	61.3	62.1	62.6	64.6	69.2
Length (ns)	4.4	4.3	4.3	4.4	4.3	4.8
Area (cm^2)	177.8	237.1	254.0	238.9	293.5	353.9
Thickness (cm)	0.5	0.5	0.5	0.5(f)-1.0(b)	1.0	1.0

Scintillator	7	8	9	10	11	12
Length (cm)	74.7	80.8	88.6	95.8	104.5	112.3
Length (ns)	5.6	5.1	6.0	6.4	7.0	
Area (cm^2)	441.6	441.8	581.2	689.5	878.2	864.5
Thickness (cm)	1.0	1.0	1.0	1.0	1.0	1.0

Scintillator	13	14	15	16
Length (cm)	120.1	136.8	135.0	136.0
Length (ns)	8.0	9.5	9.3	9.3
Area (cm^2)	871.4	1146.7	1209.9	1218.8
Thickness (cm)	1.0	1.0	1.0	1.0

TABLE 3.1: *Lengths and areas of the NA G^0 scintillators. The scintillators are arc shaped. The length (in centimeters) refers to the perimeter of the inner arc. The statistical precision of the measurement (in nanoseconds) is 0.3 ns. Note that the size of the scintillator is not the same for French and North American octants. Also note that the thickness of scintillator 1 to 3 is 0.5 cm. The thickness of scintillator 4 back (b) is 0.5 cm, the thickness of scintillator 4 front (f) is 1 cm, and the thickness of scintillator 5 to 16 is 1 cm.*

Light Pipe

The North American light guides are made out of Lucite. The French light guides are made of Polymethyl Matacrylate (PMMA). The North American detectors used Philips XP2262B (12 stages) PMTs powered by custom made Zener-resistor bases [52]. The French detectors used Photonis XP2282B04 (8 stages) PMTs powered by a custom made Zener base with an amplifier with a gain of 20. The light pipes are wrapped in μ-metal to reduce any remaining fringe magnetic field influence from the G^0 magnet.

Light-Tight Box

The North American light pipes are individually wrapped in aluminized mylar. The French light pipes are wrapped in aluminum foil. These light pipes are not light-tight. For operating the PMTs, the assemblies are enclosed in a light-tight box known as an octant. Each octant is roughly 2 m by 2 m by 3 m long. The octant consists of aluminum plates on four sides with a black cover on the remaining fifth side. The inside of the octant support as well as the aluminum plates have been covered by black Tedlar to minimize reflection of light leaks. The front fifth side of a North American (French) octant is covered by a sheet of Herculite (plastic sheeting). No access is possible to the inside of the octant without destroying the integrity of the light tight-box.

Detector Superstructure Support Frame

The North American and French octants "plug in" to a detector superstructure known as the "Ferris Wheel" (see Figure 3.5). Within the Ferris Wheel, the North American octants are located at the 12 o'clock, 3 o'clock, 6 o'clock and 9 o'clock positions. The French octants are located in between the North American

octants. Each octant is attached to the Ferris Wheel by means of three bolts on the downstream face of the structure. The Ferris Wheel is about 7 m above the floor at its highest point with the symmetry axis (the beam line) 4 m from the floor. The detectors are shielded from the beam line by 9.525 cm of lead and 15.716 cm of poly-boron. A rail system permits the Ferris Wheel to be retracted from the Superconducting Magnet System. This is done so that the G^0 apparatus can easily be moved out of the beam line so other experiments in Hall C can be performed.

3.4 The G^0 Beam

G^0 requires a beam current of 40 μA pulsed at 31.2 MHz instead of the typical CEBAF 499 MHz. This produces a charge bunch that is 16 times larger than the normal operating mode bunch. These high charge bunches require special beam optics due to space charge effects. Each micropulse contains on average 1.28 pC, yielding an average current of 40 μA.

In order to measure the small asymmetry between the two helicity states the same experimental conditions must exist for the two different helicity states. Deviations in the experimental conditions between the two helicity states can induce a false asymmetry.

The number of detected particles measured in each helicity state depends on the electron-proton scattering cross section. This cross section is sensitive to energy, beam position, and beam angle. Any systematic difference between these properties for the two helicity states can manifest itself as a false asymmetry.

Helicity-correlated differences typically originate in the injector due to the way the circularly polarized laser light emerges from the Pockels cell. The beam will not be perfectly circularly polarized but will be elliptically polarized due to some residual linear component; this, coupled to the analyzing power of the cathode, produces

	A_q (ppm)	Δx (μm)	Δy (μm)	$\Delta\theta_x$ (μrad)	$\Delta\theta_x$ (μrad)	$\Delta E/E$ ($\times 10^6$)
specified	1	20	20	2	2	10
measured	1	7	5	2	2	6.0

TABLE 3.2: *The measured run averaged helicity-correlations for January 18-26, compared to the G^0 specifications for 700 hours of data taking.*

helicity-correlated differences in the beam. Helicity-correlated laser motion coupled to spatial variations in the quantum efficiency of the cathode will also produce helicity-correlated differences in the beam. Beam scraping in the injector (and possibly in the main machine) can cause helicity-correlated beam differences.

Charge asymmetries[1] must also be minimized since charge asymmetries can induce helicity-correlated differences in other beam parameters. Via beam loading, charge asymmetries become energy differences. Energy differences, in turn, manifest themselves as position differences due to achromatic transport through the accelerator.

The G^0 experiment has specified how large these helicity-correlated beam differences can be allowed to be (see Table 3.2). This is because the size of these quantities determines how accurately the helicity-correlated beam properties are measured. This in turn determines the errors on the correction procedures to correct for the helicity-correlated beam properties.

3.4.1 The G^0 Beam Structure

The Time-of-Flight technique requires that the polarized electron beam be pulsed at 31.2 MHz rather than the typical CEBAF 499 MHz. This translates into buckets of polarized electrons arriving every 32 ns at the target. The helicity of the beam is flipped at 30 Hz. One illustration of why this time scale is chosen

[1]The charge asymmetry is defined as $A_q = \frac{Q_+ - Q_-}{Q_+ + Q_-}$

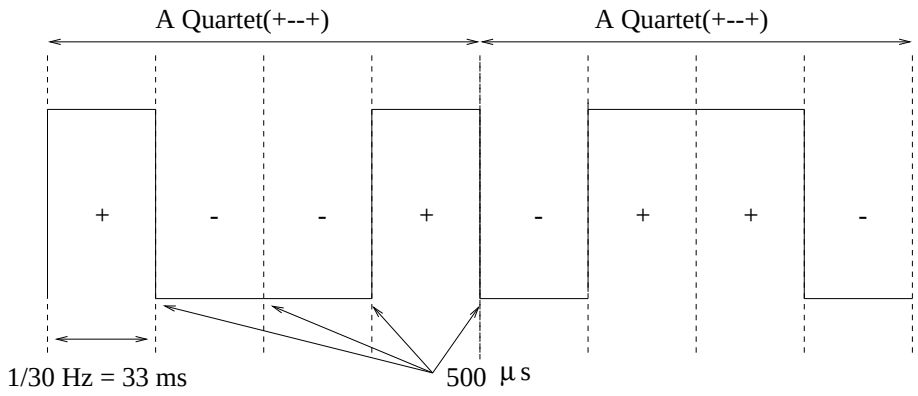

FIG. 3.7: *The G^0 beam structure. The G^0 beam is pulsed at 31.2 MHz. The G^0 beam flips helicity every 30 Hz, known as a macropulse (MPS). The G^0 beam is divided into quartets of four MPSs. The first MPS is chosen pseudo-randomly with the next two MPSs the complement of the first MPS and the fourth MPS is the same as the first MPS.*

can be seen if there is 60 Hz noise in a power supply causing a discriminator level to oscillate up and down at 60 Hz. Then during one half of the cycle more counts would be collected than in the other cycle. If the spin flipping was not a multiple of the 60 Hz period, there would be non-statistical fluctuations from one data collection period to the next. By holding each helicity state for 1/30 s, the experiment averages over any changes in the experiment caused by the 60 Hz noise and any of its harmonics. 30 Hz is also a quiet frequency in regards to noise, with higher frequencies typically populated by noise from electronics and lower frequencies sensitive to mechanical vibrations. Each 33 ms helicity state of the beam is referred to as a macropulse (MPS). The helicity is reversed during a 500 μs interval (see Figure 3.7). The macropulses are grouped into quartets with the sign of the first MPS being chosen pseudo-randomly. The next two MPSs are the helicity complement of the first MPS. The last MPS helicity in the quartet is the same as the first MPS helicity. The beam helicity is flipped quickly to insure that short-lived changes in the experimental conditions are experienced by both helicity states.

Since there is a 500 μs settle time for the Pockels cell, this scheme allows the

phase of each new helicity states to slip with respect to the 60 Hz power cycle. This phase slip is beneficial to the experiment. This will allow the helicity states to precess through all the phases and thus sample different aspects of the 60 Hz line noise.

3.5 The CEBAF Injector and the Polarized Source

This section describes the various pieces of equipment that are in the injector and associated with the polarized source. A description of the helicity devices on the polarized source laser table in the injector are covered along with a description of the performance of the feedback systems that use these helicity devices. The G^0 TIGER laser used to excite the photo-cathode along with the GaAs photo-cathode are also described in this section.

3.5.1 The G^0 TIGER Laser

The G^0 laser, known as the TIGER, is a Ti-Sapphire laser. Ti:Sa lasers can achieve both high current and high polarization, unlike the typical diode lasers used at CEBAF that can achieve either high current or high polarization but not both. The TIGER laser is a commercial laser produced by Time-Bandwidth. It has passive mode-locking to reference the 31.2 MHz RF source. The TIGER laser produced more than 300 mW of power at a wavelength of 840 nm. The TIGER laser is tunable from 770-860 nm.

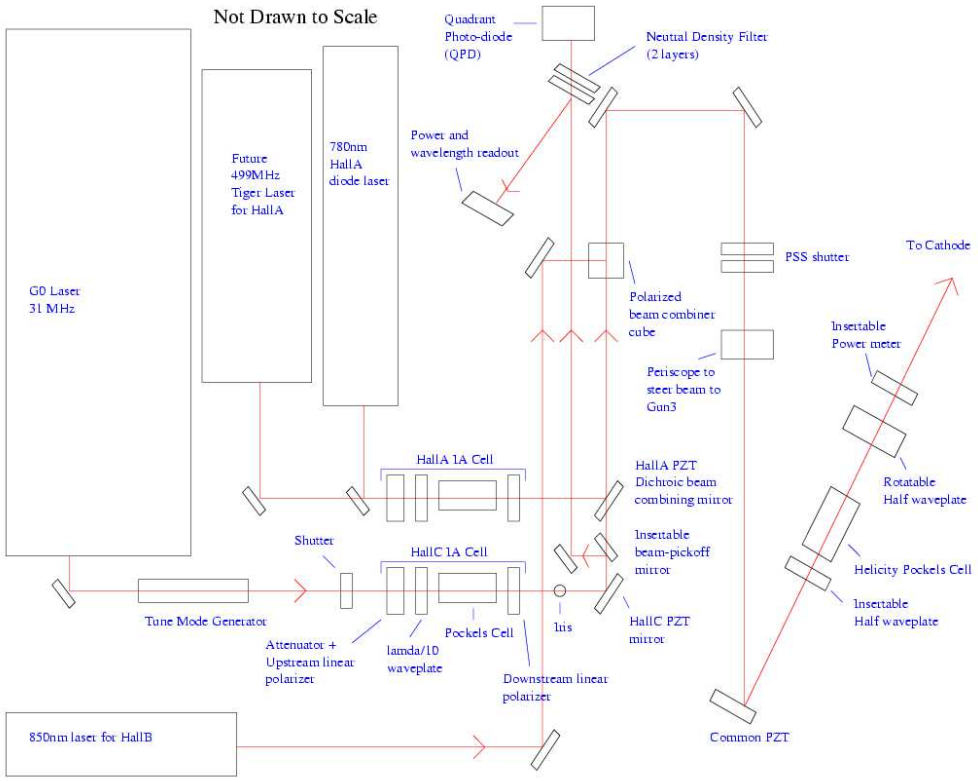

FIG. 3.8: *Schematic of the CEBAF polarized source laser table in the injector. This schematic shows the path the laser light produced by the G^0 TIGER laser follows. Important optical elements to note are the IA cell used for controlling intensity differences and the PZT used to control helicity-correlated position differences. There is a quadrant photo-diode (QPD) that is used to understand the optical elements upstream of the QPD. The insertable halfwave plate is a device to passively change the handedness of the laser light and thus used as a diagnostic for understanding helicity-correlated noise in the system. The helicity Pockels cell is used to flip and produce circularly polarized light before striking the photo-cathode.*

3.5.2 Optical Elements

Intensity Attenuator Cell

The Intensity Attenuator (IA) cell is the central device in the injector used by the charge feedback system from Hall C to null the charge asymmetry without inducing large helicity-correlated beam differences. The IA cell is an electro-optic modulator (see Appendix B for more details). This device modulates the laser light in a helicity-correlated manner before it reaches the photo-cathode. The IA is made

up of a Lasermetrics model 1059-10 Pockels cell with a 3° wedge on both faces and a broadband anti-reflective coating at 850 nm. The Pockels cell is between two parallel linear polarizers followed by bare mica model WPUM-10-850 tenth-wave plate for 850 nm from the Karl Lambecht Corporation.

Linearly-polarized light from the laser is transmitted through the first linear polarizer, then is transmitted through the tenth-wave plate. This produces slightly elliptically polarized light. This elliptically polarized light is transmitted through a low-voltage Pockels cell (operating at about 50 V in one helicity state). If the Pockels cell is at 0 V, then the elliptically-polarized light is transmitted unchanged through the cell. The light is then transmitted through the second polarizer (parallel to the first polarizer) and linear light is produced. If the IA Pockels cell is at some non-zero voltage, more elliptically polarized light emerges from the Pockels cell. When this elliptically polarized light is transmitted through the second parallel polarizer only the linear component will survive, thus modulating the intensity of the laser beam.

The IA cell responded well during the commissioning, offering a large ($\sim$ 400 ppm/V) intensity difference calibration, though it did generate large position differences for reasons that were not always clear (see Table 3.3). The IA calibration constants were fairly stable over time, but did require new measurements of this constant roughly every couple of days, or whenever the insertable halfwave plate was inserted or retracted. The main problem with the IA cell was variations in time of the calibration constant (ppm/V). This was caused by the IA cell inducing position differences that created charge asymmetries at apertures in the injector (see Figure 3.9). This occurred as the IA would steer the beam in a helicity-correlated way causing the electron beam to clip along the sides of apertures in the injector. These apertures' diameters were subsequently increased to reduce this problem.

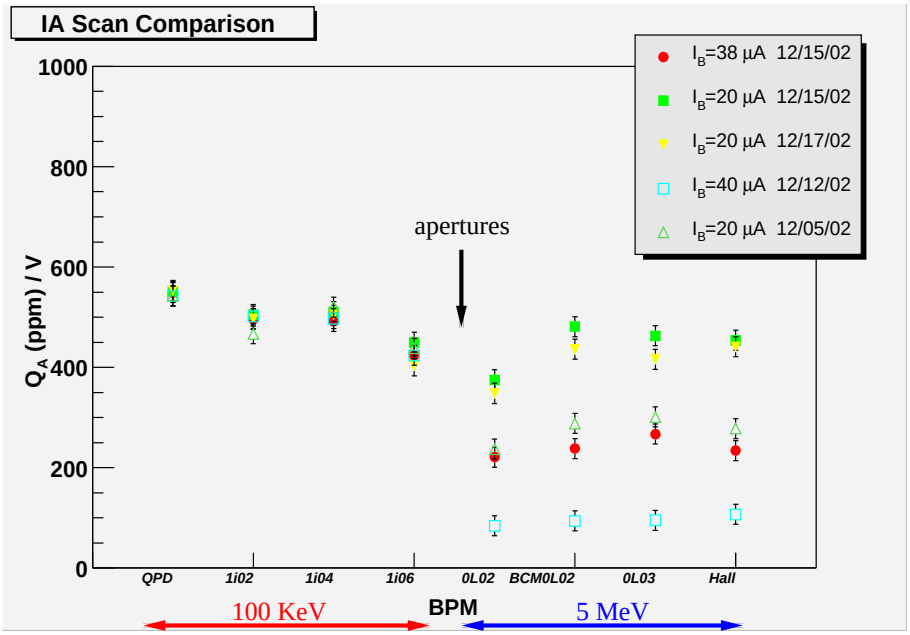

FIG. 3.9: *The IA calibration constants (ppm/V) as a function of beam position monitor in the injector to Hall C. A quadrant photo-diode (QPD) is placed on the laser table to determine what is happening on the laser table. Note that the values from 1i02 to 1i06 are consistent with one another. Between 1i06 and 0L02 are two apertures. It is hypothesized that, due to scraping on these apertures, the calibration constant did not remain the same between the 1i06 and 0L02 regions.*

Intensity Feedback

The automated intensity feedback uses the IA cell (see section 3.5.2). It was used to vary the laser intensity in a helicity-correlated way to insure that the helicity-correlated electron beam intensity measured in Hall C at BCM1 (Beam Current Monitor) is kept small. BCM1 is used to measure beam currents above 20 μA and, another BCM, BCM2, is used to measured beam currents from 5-20 μA. Typically a change to this feedback system was made every 5 minutes (see Figure 3.10). The nature of the feedback system is to cancel the contributions arising from the statistical jitter of the charge asymmetry. In the absence of feedback, the statistical reduction in the charge asymmetry goes like $\frac{1}{\sqrt{N}}$ where N is the number of 5 minute measurements. With the charge asymmetry feedback active, the charge asymmetry

date	charge (ppm/V)	x position (nm/V)	y position (nm/V)
Jan. 13 '03	-468	840 ± 100	958 ± 100
Jan. 16 '03	-452	645 ± 323	1117 ± 497
Jan. 25 '03	-237	46 ± 334	14 ± 241
Jan. 15 '03	-313	N/A	N/A
Jan. 17 '03	-344	N/A	N/A
Jan. 19 '03	-348	N/A	N/A
Jan. 23 '03	-537	231 ± 219	95 ± 267
Jan. 26 '03	-231	-58 ± 225	6 ± 183
Jan. 26 '03	-201	-21 ± 174	-75 ± 134
Jan. 27 '03	-197	83 ± 213	-4 ± 162

TABLE 3.3: *Table of the IA calibration slopes measured in Hall C. Overall, the IA feedback was moderately stable during the engineering run. Entries marked 'N/A' do not have data available.*

convergence goes like $\frac{1}{N}$.

Rotating Halfwave Plate

The rotating halfwave plate (RHWP) is also used to minimize the intensity difference. The halfwave plate operates on the principle that the light from the Pockels cell will not be perfectly circularly polarized, but will instead be elliptically polarized. Elliptically polarized light can be decomposed into two components: circular polarized and linearly polarized. The RHWP takes the residual linear component of the light and rotates it with respect to the cathode depending on the adjustable rotation angle (see Figure 3.11). Scans of the halfwave plate are done on the order of days (versus the IA, which is used to minimize the intensity difference on the order of minutes using an automated feedback system) to find the minimum intensity difference (known as the "sweet spot"). From results in Hall C, the setting for the sweet spot of the RHWP is very stable and the null setting only needed to be checked on a daily basis.

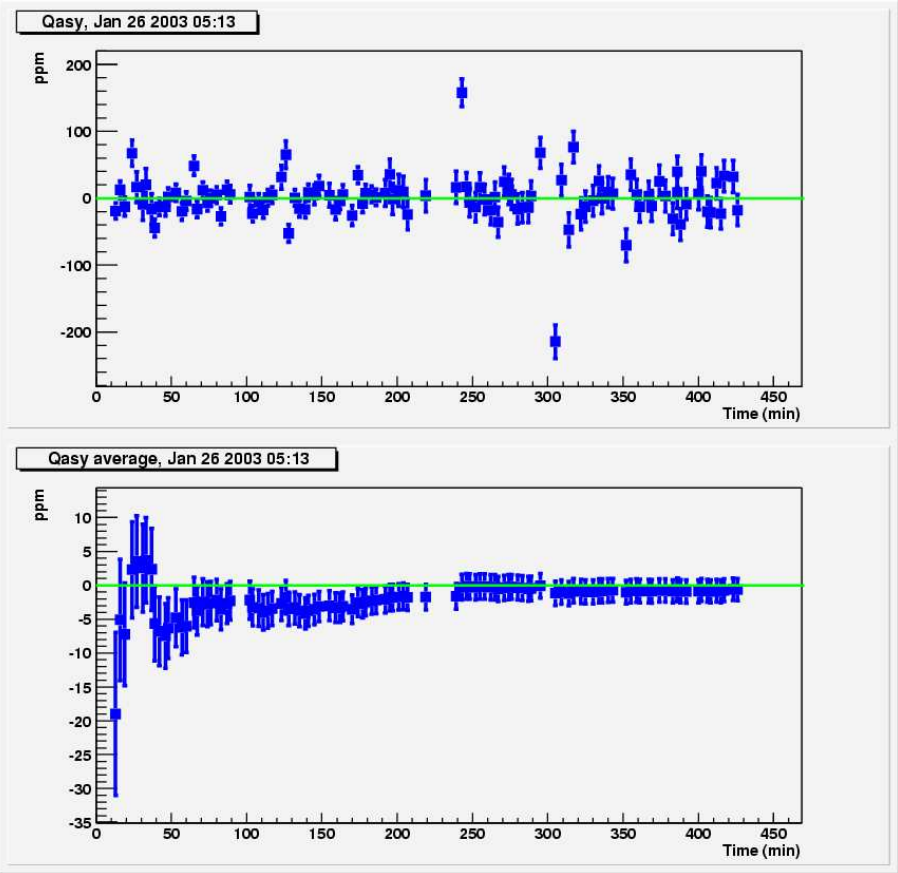

FIG. 3.10: *Typical performance of the charge feedback system using the IA cell. The top panel shows the intensity difference as measured every 5 minutes. The bottom panel shows the run-averaged intensity difference converging to zero as time goes on.*

PZT

The PZT is a device used to correct for helicity-correlated beam position. This device is a mirror mounted on a Thor Labs KC1-PZT kinematic mount. The PZT is an electro-ceramic lead-zirconae-titanate ceramic which is piezoelectric. The PZT can be set to different independent positions in both the X and Y directions. The PZT oscillates between these set positions and the null position at the helicity-flip frequency (each 1/30 s). This allows any helicity-correlated position differences in the electron beam to be corrected by changing the angle that the laser beam strikes the photo-cathode in a helicity-correlated manner.

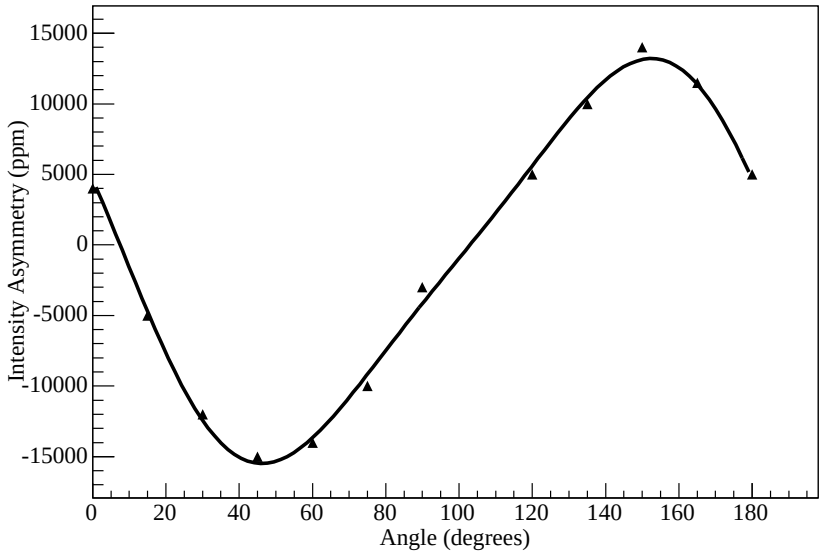

FIG. 3.11: *Measurement of the intensity difference as a function of rotatable halfwave plate angle. The rotatable halfwave plate is set to an angle to null the charge asymmetry. In this plot the null point would have been chosen to be near 100°.*

Another issue with the PZT was related to the orthogonality of the PZT X and PZT Y motion. If this motion is not orthogonal, one may not be able to effectively and independently correct for x and y position differences. For example, if the PZT X and PZT Y motion was exactly at 180° then it would be impossible to correct for both X and Y motion. Note that rotations are fine since some combination of PZT X and PZT Y would still correct for X and Y beam motions. Hence the calibration of the PZT requires not just measuring the calibration slope for PZT X in X (denoted as XX) but also what affect PZT X has on Y (denoted at YX), motion and how PZT Y not only affects Y (denoted at YY) motion but X motion (denoted as XY) of the beam. Table 3.5.2 lists the calibration slopes of the PZT.

date	XX (nm/V)	YX (nm/V)	XY (nm/V)	YY (nm/V)
Jan 24	541.3 ± 25.5	573.2 ± 25.1	-206.7 ± 25.1	150.3 ± 24.8
Jan 14	606.5 ± 37.9	843.4 ± 37.0	-253.5 ± 40.7	521.9 ± 41.1
Jan 12	-478.1 ± 33.8	-510.4 ± 34.4	356.3 ± 34.2	490.6 ± 35.2

TABLE 3.4: *Table of the limited number of PZT calibration slopes in nm/V. The PZT did not perform well during the engineering run. XX (YX) denotes the affect of PZT X on the X (Y) beam motion. YY (XY) denotes the effect of PZT Y on the Y (X) beam motion.*

Position Feedback

This feedback system was intended to be used to vary the position of the laser beam on the photo-cathode in a helicity-correlated manner. This feedback loop insures that the helicity-correlated beam position as measured in Hall C by beam position monitors G0 and G0B is kept small. The PZT's calibration constants were unstable on time scales of the order of minutes during the 2002-2003 G^0 commissioning run. This meant that the position feedback to control the helicity-correlated position differences was not used. Even though the position feedback was not used, the measured mean position differences (ΔX and ΔY) were on the order of 50 nm with a σ of 6 μm.

3.5.3 Helicity Generation

The electronics (known as the G^0 Helicity Digital Controls) that determine the helicity are located in the Injector Service Building above the polarized source. The helicity of the electrons is determined by the helicity Pockels cell. The G^0 Helicity Controls adjusts the Pockels cell, thus controlling the helicity of the electrons injected into the accelerator. The make-up of the G^0 Helicity Digital Controls include a pseudo-random bit pattern stored in two 1Mbit EPROM's and control code, which includes multiplexers, registers, counters, and a state machine [53].

The output of the G^0 Helicity Digital Controls is either 1 or 0. The helicity state of the electrons in turn is based on whether the output from the G^0 Helicity Controls is a 1 or 0. In order to reduce helicity-correlated crosstalk and ground loops, the helicity signal from the helicity electronics is fed to the G^0 electronics and DAQ in Hall C via a fiber optic cable. Furthermore, this signal sent to Hall C is delayed by eight helicity windows, thereby ensuring no in-time helicity correlation between the helicity Pockels cell and the signals sent to Hall C.

3.5.4 Photocathode

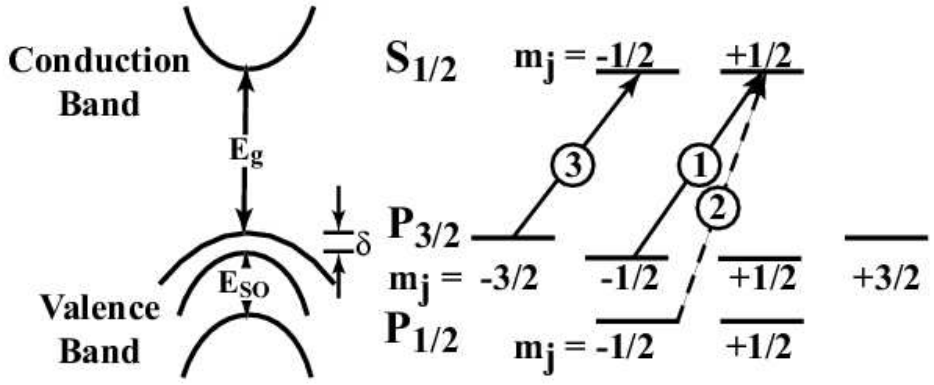

FIG. 3.12: *A schematic of the strained GaAs band structure and energy level diagram. The circled numbers indicate the relative transition strengths.*

The strained GaAs crystal acts as the photo-cathode for the polarized source. GaAs is a direct band-gap crystal, which means that the valence band maximum and the conduction band minimum are aligned in momentum space, allowing for optical transitions between the energy bands that follow the angular momentum selection rules for optical transitions in atoms. These transitions are shown in Figure 3.12. The strained layer GaAs photo-cathodes are produced by Bandwidth Semiconductor. By photo-emission, polarized electrons can be liberated from the crystal

to be used in the polarized electron beam for the accelerator. In photo-emission, an electron in the valence band ($P_{3/2}$ and $P_{1/2}$ levels) absorbs a circularly polarized photon and is excited to the conduction band. The crystal has been specially treated with Cesium Fluoride to increase the quantum efficiency of the cathode by reducing the work function of the GaAs. This also produces a negative electron affinity to allow the electrons to escape from the crystal. A typical quantum efficiency for the photo-cathode is about 1% for light with a wavelength of 780 nm. The cathode is held at a bias voltage of -100 kV in order to liberate the electrons from the cathode.

The GaAs crystal is "strained" in order to the electron beam polarization. The maximum polarization of the strained GaAs crystal is about 80% compared to typical polarizations of 40% for bulk GaAs crystal. This is done by growing a thin layer of about 100 nm of GaAs on a substrate of GaAsP, which breaks the degeneracy of the $P_{3/2}$ and $P_{1/2}$ levels.

An issue with the strained GaAs crystal is that a large quantum efficiency anisotropy is produced, which in turn can produce a charge asymmetry. The light emerging from the Pockels cell is not typically perfectly circularly, but has a residual linear component. The axis of the residual linear component of the light can be different for the two helicity states. In this case there will be two different orientations of the light's polarization axis with respect to the "strain axis" of the crystal. Because these axes are different, the number of electrons liberated from the crystal is different in a helicity-correlated way, producing a charge asymmetry for the resulting electron beam.

The crystal is located in the electron gun and is kept under very high vacuum. Still, residual gases can contaminate the crystal surface thereby lowering the quantum efficiency. This residue needs to be removed periodically by performing a "bake-out". This is when the temperature of the gun is raised until the contaminated molecules have evaporated away.

3.5.5 The CEBAF Accelerator at Jefferson Lab

The Continuous Electron Beam Accelerator Facility at Jefferson Lab can deliver up to 5.5 GeV of 200 μA polarized electron beam. A Wien filter in the injector sets the launch angle of the polarization vector to compensate for g-2 precession, thereby assuring that longitudinally-polarized electrons arrive at the experimental halls. The polarized electrons are injected at 45 MeV into the main accelerator. The electrons are accelerated in two linacs that make up the straight portions of the accelerator racetrack. The linacs are connected by recirculating arcs located at both ends of the linac. Acceleration is provided by the CEBAF-Cornell superconducting radio frequency cavities that operate at 1497 MHz. The electron beam can take up to 5 passes around the accelerator before being sent to one of the three experimental halls. This is done by using an electromagnetic "kicker" to send every third electron bunch to the appropriate hall, resulting in a beam structure of 499 MHz in the halls.

3.5.6 Beam Instrumentation

Beam Current Monitors

Hall C is equipped with three different beam current monitors (BCMs). Two of these BCMs, BCM1 and BCM2, are cylindrical resonant cavities [54, 55]. The current is monitored by using the electron beam to excite the resonant modes in the cylindrical waveguide. The cavity is sensitive, by design, to the TM_{010} mode. Inside the cavity is a loop antenna which couples to the resonant modes. The measured signal is proportional to the beam current. In addition to the two cavity monitors, Hall C is also equipped with a parametric current transformer (also known as the Unser) [56]. The Unser has a very stable and well-measured gain but it suffers from large unstable offsets. The Unser is not used to measure the beam current but due to its stable gain it is used to calibrate the BCMs. The noise in BCM1 is found to

be about 300 ppm which is much smaller than the statistical width of the measured asymmetry from one quartet (see Section 4.2).

Beam Position Monitors

The beam position monitors (BPMs) used during the first engineering run in both the injector and Hall C were standard strip-line BPMs [57,58]. These BPMs are made up of four antennae situated symmetrically around the beam at 45° angles. The BPMs operate at 1500 MHz and inductively pick up the RF signals of the electron beam as it passes through the device. The signals are then amplified and down-converted to 1 MHz. The signals for beam position can then be computed knowing that the signal in the antenna is proportional to the beam position and beam intensity:

$$\text{BPM Antenna Signals} \propto \text{(Beam position)} \times \text{(Beam Intensity)}$$

The relative X' and Y' beam positions can be calculated

$$X' = k\frac{(X_+ - X_{\text{offset}+}) - \alpha_X(X_- - X_{\text{offset}-})}{(X_+ - X_{\text{offset}+}) + \alpha_X(X_- - X_{\text{offset}-})} \tag{3.3}$$

and similarly for Y'. $X_{\text{offset}+(-)}$ is the offset for the $X_{+(-)}$ antenna. Since the gain of each antenna may be different, α_X is a measure of the different gain between the X_+ and X_- antenna. This measure of this gain difference is

$$\alpha_X = \frac{X_+ - X_{\text{offset}+}}{X_- - X_{\text{offset}-}}. \tag{3.4}$$

Since the BPMs are oriented at 45 degrees, the position of X is given by

$$\begin{pmatrix} X \\ Y \end{pmatrix} = \frac{1}{\sqrt{2}} \begin{pmatrix} 1 & -1 \\ 1 & 1 \end{pmatrix} \begin{pmatrix} X'Y' \end{pmatrix}. \tag{3.5}$$

The position (or position difference) calculated from the beam monitors has a certain amount of noise associated with it. This noise is due both to beam noise and to electronic noise. The measured noise can be written as:

$$\sigma^2_{\text{measured}} = \sigma^2_{\text{beam}} + \sigma^2_{\text{instrumental}}.$$

The instrumental noise can be found by using three BPMs along the beam line without magnetic optics between the monitors. The first two BPMs can be used to determine the position of the beam in the third monitor. This predicted behavior can then be removed from the measured signal of the third BPM leaving behind only the instrumental noise. The noise of the BPMs was found to be about 2 μm.

3.6 Halo Monitors

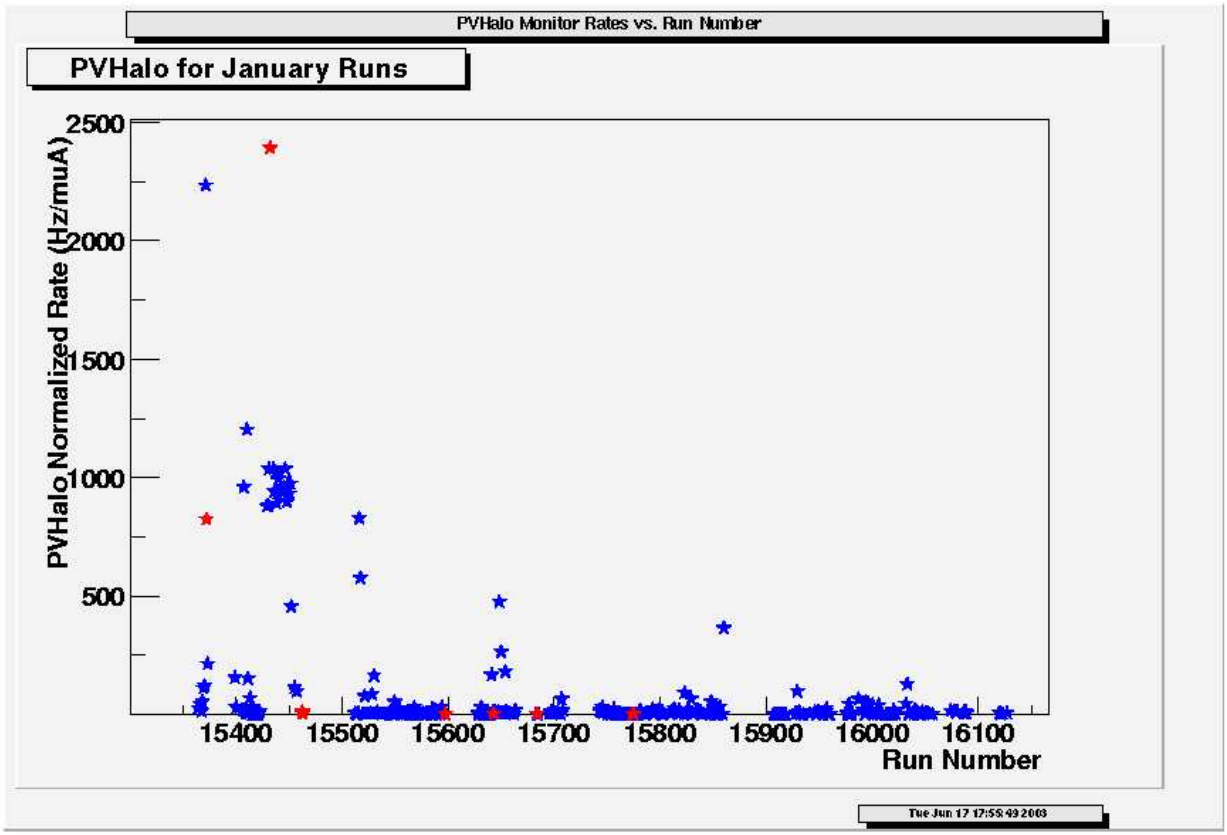

FIG. 3.13: *Plot of normalized rates as a function of run number for the 2003 G^0 Engineering run as measured by the Lucite Halo Monitor. The red (blue) points correspond to the halo target 'in' ('out') data. The baseline value for 'good' beam is approximately 5 Hz/μA)*

Electrons outside the core of the electron beam are defined as the beam halo. This halo could be produced in a variety of processes. The halo could be formed by space-charge effects, beam scraping on an aperture, interactions of residual gas in the beam line, etc. This halo can cause numerous troubles. These halo electrons could cause an increase in the dead time by producing higher singles rates in the G^0 detectors from inelastic scattering and they could also contribute to the inelastic background. This higher unwanted radiation could also cause radiation damage to the PMTs. It is for these reasons that the G^0 experiment requires a limit on the beam halo of 1 ppm outside a 6 mm radius of the electron beam. The halo monitors are used to detect beam halo and time-dependent halo behavior of the electron beam in Hall C. This system was designed to be non-invasive, so that the beam halo could be monitored continuously during data taking. This detector system was made up of a bare Hamamatsu 931B low gain PMT, a Phillips XP2262 PMT coupled to a piece of 10 cm long, 5 cm diameter Lucite cylinder, and a PMT coupled to a lead glass brick that measured 4 cm $\times$ 4 cm $\times$ 43 cm. Multiple detector types were used as a part of a study to determine which was the optimal design for the halo detector. A 2 mm thick carbon target with a 6 mm diameter square hole was located at the hall C pivot. The main portion of the electron beam would pass through the hole but halo electrons would interact with the target. Besides the ability to read out the beam halo rates, the halo target also had a Fast Shut Down output so that if the beam halo rate became too high the electron beam would be turned off.

From the engineering run, it was found that not all the prototype halo monitors were suitable for use. The bare PMT was damaged by work done at the Hall C target pivot. The lead glass halo monitor had a large amount of noise associated with it and was insensitive to the target 'in' and 'out' differences. The Lucite halo monitor worked the best. It was fairly insensitive to low-energy background and was sensitive to the position of the halo target. It was found that for good beam, the Lucite halo

monitor observed a baseline value of 5 Hz/μA (see Figure 3.13).

3.7 Lumi Monitors

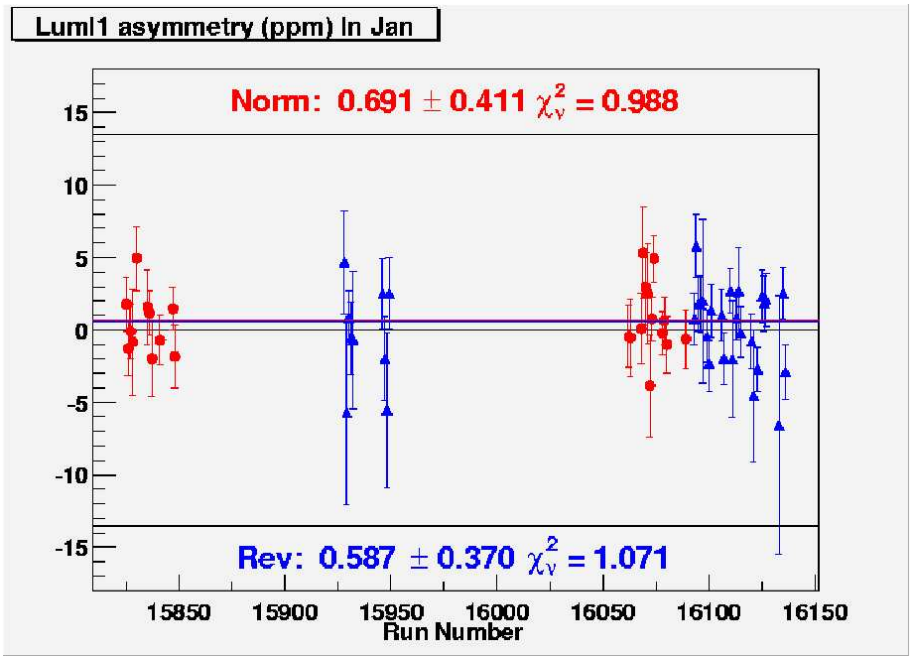

FIG. 3.14: *Plot of Lumi asymmetry as a function of run number for the 2003 G^0 commissioning run. Due to the extreme forward angle of the Lumi monitors, measured asymmetries may be due to beam boiling effects on helicity correlated properties of the beam. The red circles (blue triangles)indicate when the insertable halfwave plate was in the 'out' ('in') position.*

Downstream of the G0 target is a detector package that measures the luminosity. The luminosity is the product of the beam current and target density. This detector package consists of a pair of bare PMTs, a pair of PMTs with Lucite (Cerenkov light is produced in the Lucite and the signal is picked up by the PMT), and a prototype water Cerenkov detector from Mainz experiment PVA4. After dividing out the beam charge, target density fluctuations can be monitored along with helicity-correlated properties of the electron beam. The luminosity monitors are at extreme forward angles and thus the parity-violating asymmetry should be

near zero. If an asymmetry is measured by the detectors, this implies that a false asymmetry is being generated, presumably due to helicity-correlated beam parameter differences or electronics artifacts. Results from the LUMI monitors are shown in Figure 3.14 indicating that the target was neither boiling nor were there large effects from helicity-correlated beam properties.

3.8 Moller Polarimeter

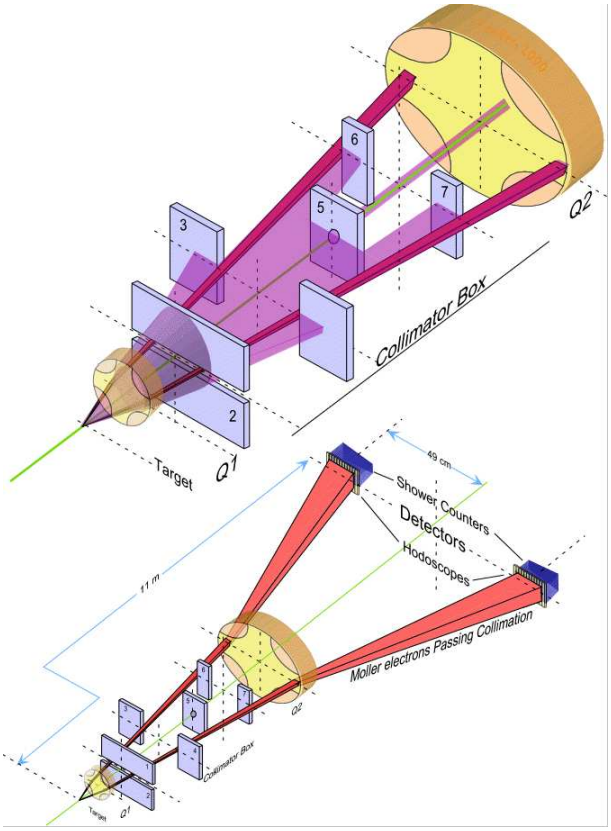

FIG. 3.15: *The Hall C Polarimeter. The top schematic shows the collimators and quadrupole magnets used to select scattered electrons of interest. The bottom schematic shows the scattered electrons focused onto the polarimeter detectors.*

The beam polarization was measured by the Hall C Moller (polarized $\vec{e}+\vec{e}\rightarrow e+e$) polarimeter [59] which is located in the beam alcove upstream of Hall C. Ob-

serving differences in the scattering rates, depending on whether the beam and target electrons are polarized parallel or anti-parallel with one another, provides a measurement of the beam polarization. Since this is a QED process, the cross sections has been calculated precisely (up to α^4_{QED}). The cross section for a longitudinally-polarized electron beam striking a polarized target electron is:

$$\frac{d\sigma}{d\Omega} = \frac{d\sigma_0}{d\Omega}\left[1 + P_t^{\parallel} P_b^{\parallel} A_{ZZ}(\theta)\right] \tag{3.6}$$

where the unpolarized cross section $\frac{d\sigma_0}{d\Omega}$ is given by

$$\frac{d\sigma_0}{d\Omega} = \left(\frac{\alpha(4 - \sin^2\theta)}{2m_e\gamma \sin^2\theta}\right)^2 \tag{3.7}$$

and in the high energy limit, the analyzing power is given by

$$A_{ZZ}(\theta) = \frac{-\sin^2\theta(8 - \sin^2\theta)}{(4 - \sin^2\theta)^2}. \tag{3.8}$$

One can measure the beam polarization by comparing the cross section asymmetry for the beam and target spins aligned parallel and anti-parallel:

$$\epsilon = \frac{\dfrac{d\sigma^{\parallel}}{d\Omega} - \dfrac{d\sigma^{\perp}}{d\Omega}}{\dfrac{d\sigma^{\parallel}}{d\Omega} + \dfrac{d\sigma^{\perp}}{d\Omega}} = A_{ZZ}(\theta) P_t^{\parallel} P_b^{\parallel}. \tag{3.9}$$

Knowing the target polarization $P_t^{\parallel}$ allows one to isolate the beam polarization.

The target electrons are provided by atomic electrons associated with the iron atoms in the target. Typically, about 2 electrons of the iron's 26 electrons are polarized, leading to a target polarization $\sim 8\%$. The target is a thin foil of iron oriented perpendicular to the electron beam which is magnetized by a superconducting solenoid producing a 4 T field. The scattered electron and recoiled target electron that emerge in the horizontal plane between 1.83° and 0.75° in the lab frame are focused by a quadrupole magnet Q1. The desired scattering angles are set by collimators. The electrons are then defocused using another quadrupole magnet,

Q2, and the electrons detected in coincidence using two symmetrically placed hodoscope counters and lead glass counters. This system of movable collimators and a pair of quadrupoles allow this device to be tuned to operate at any beam momentum between 0.9 and 6.0 GeV/c.

The need to correct the elastic asymmetry for the polarization can be demonstrated as follows from considering the scattering cross sections. One of these components is a parity-conserving electromagnetic part (σ_{EM}) that is equal for both helicity states. Then there is a parity-violating part, σ_{PV}, which is caused by the interference between the weak and electromagnetic amplitudes. This parity-violating part has opposite signs depending upon the helicity, thus the contribution of (σ_{PV}) will scale with the beam polarization. The right-handed component of the cross section can be written as

$$\sigma_+ = \sigma_{EM} + P_b\sigma_{PV} \tag{3.10}$$

while the left handed component can be written as

$$\sigma_- = \sigma_{EM} - P_b\sigma_{PV}. \tag{3.11}$$

Assuming that $\sigma_{PV} << \sigma_{EM}$, the asymmetry equation can be written as

$$A_{el} = \frac{(\sigma_{EM} + P_b\sigma_{PV}) - (\sigma_{EM} - P_b\sigma_{PV})}{(\sigma_{EM} + P_b\sigma_{PV}) - (\sigma_{EM} + P_b\sigma_{PV})} \approx P_b\frac{\sigma_{PV}}{\sigma_{EM}} = P_bA_{physics}. \tag{3.12}$$

3.9 Data Acquisition

The data acquisition system (DAQ) used by the G^0 experiment is CODA (CEBAF Online Data Acquisition system) [60]. CODA was developed by Jefferson Lab. The G^0 DAQ runs on a 1 GHz Pentium III computer running Linux (kernel 2.4.18). The DAQ reads out the time-encoding scaler data (see Section 3.10) at a rate of 30 Hz during the 500 μs window for the Pockels cell to settle down after flipping

helicity. The time encoding data is read from the North American Scalers and from the French DSP concentrator on the DMCH-16X boards (see Section 3.10). During an MPS $\sim$ 50 kB of data is collected. Besides the 30 Hz time-encoding data, other types of data events are interleaved in the data stream. FASTBUS ADC and TDC data (see Section 3.10) were collected at a rate of 1/30 Hz. These FASTBUS data are useful for monitoring and calibrating the detector system. In addition, "slow control" EPICS [61] events are taken at 30 Hz; these events record data from the beam position monitors, beam current monitors, temperature and pressure of the target, temperature and current in the SMS, etc. The DAQ computer running CODA communicates with each of the electronic crates via a single board computer on each crate called a ROC (Read Out Controller). There are six ROCs: ROC1, ROC2, and ROC3 all contain North American scalers, ROC3 contains the French DMCH-16X modules, ROC5 contains the FASTBUS monitoring electronics ADCs and TDCs, and the last ROC known as TS0 is the trigger supervisor that also reads out beam and slow control electronics. The CODA datafiles are copied to the tape silo system and to a group of three computers where G0Analysis, the replay engine, produces ntuples and histograms to be read by ROOT and fills a MySQL database.

3.10 The G^0 Electronics

The signals from the G^0 detectors in Hall C are routed upstairs to be processed by the G^0 electronics. The signals coming from the North American (French) detectors are handled by a North American (French) subset of the electronics. Having two different sub-systems allows for a powerful cross check between the North American and French data.

Both North American and French electronics can be described as falling into two classes: monitoring/cross calibration FASTBUS electronics and the Time Encoding

Electronics (TEE). The data obtained from the TEE is in the form of Time-of-Flight (ToF) histograms accumulated over a macropulse. The other set of electronics are used to monitor detector efficiencies, to calibrate the gains of the detectors, etc. Common to both sets of electronics is the need to minimize both dead time and helicity-correlated systematics.

As mentioned above, the North American (French) electronic sub-systems receives 256 input signals from the North American (French) octants 1,3,5,7 (2,4,6,8) and the implementation of the electronics follow two different philosophies with the North American electronics being highly modular and the French electronics being highly compact.

3.10.1 North American electronics

A schematic of the NA electronics chain is shown in Figure 3.16. The following sections describe in further detail the signal's journey from the PMT signal to accumulated data. Signals from the PMTs first go to a patch panel in Hall C through 36 meters of RG58 cables. They are then sent up to the electronic counting room in 107 meter long RG8 cables for reduced attenuation. Due to the high rate, event-by-event data collection is excluded in the Time Encoding Electronics (though the monitoring electronics record a sample of event-by-event data). The hardware must then be chosen to reduce the time resolution of the signals arriving at the Time Encoding Electronics. The nominal 1 ns wide bins are determined by a clock signal. Commercial constant fraction discriminators minimize the walk in time of logic pulse, and meantimers are employed to average the pulse times of the PMTs at opposite ends of the scintillator.

.

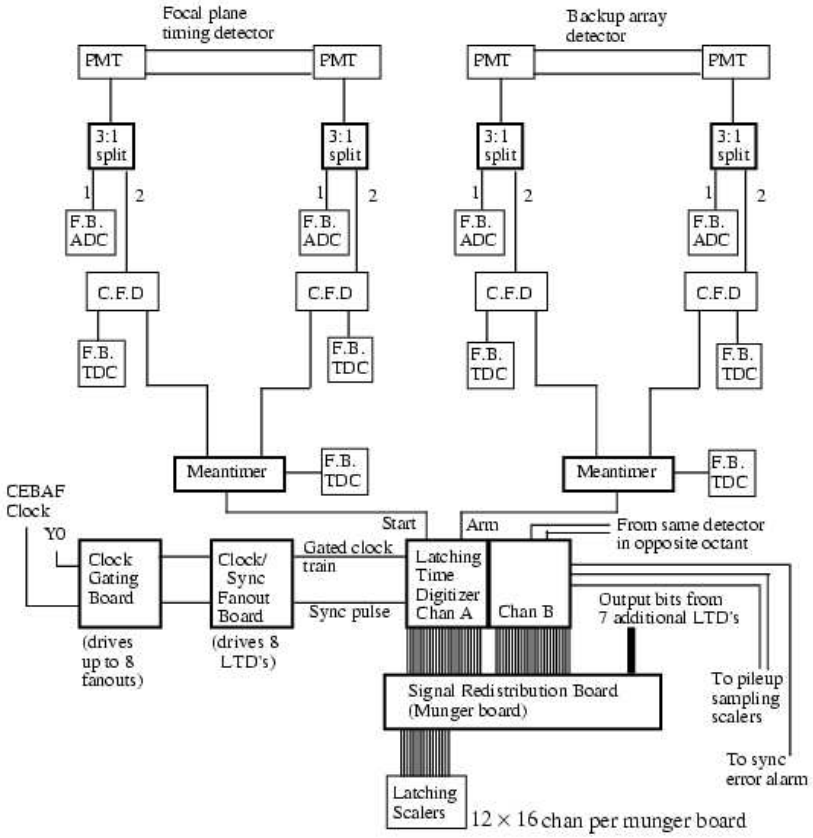

FIG. 3.16: *Schematic of the North American electronics for the G^0 forward running mode. Custom built electronics are denoted by dark boxes.*

Splitter

There are 16 custom built splitter modules. Each splitter module asymmetrically (70:30) and passively splits 16 PMT signals to provide 16 inputs to the Constant Fraction Discriminator and 16 inputs to the FASTBUS ADCs.

Constant Fraction Discriminator

The high counting rates on the detectors implies that the signals must be of low amplitude in order to reduce the instantaneous and integrated currents on the PMTs. With these low amplitude signals, a good precision on the elastic proton time information is required and time-walk could be a problem, hence the use of

the constant fraction discriminators. There are 16 Lecroy 3420 Constant Fraction Discriminators (CFDs). These CFDs take the PMT analog signal from the splitter and produce a logic signal if the signal is above some threshold, which was typically about 35 mV. This is done by generating the logic signal at some constant fraction of the peak height to produce a nearly walk-free signal. The output signals from the CFDs are then sent to the FASTBUS TDCs and to the TEE meantimers.

Meantimer

There are 8 custom built modules with 16 meantimer channels in each module. Each meantimer (MT) has inputs from two CFDs. One input is for each PMT signal from each end of a detector. The output signal is the mean time of the two PMT input signals. The mean timing of the input signals is performed by custom Application Specific Integrated Circuits.

This is done because the proton can hit anywhere along the scintillator. This will produce variations in the signals on an event-by-event basis. In order to produce a Time-of-Flight histogram that is constant, the meantime of the signals is produced.

This can be seen by considering when a detector is hit by a particle. Let t_1 and t_2 be the time of the signal from each PMT, d_1 and d_2 the distance from where the particle hits along the scintillator to the PMT, and $d = d_1 + d_2$. By taking the average of the propagation times:

$$\frac{t_1 + t_2}{2} = \frac{d_1 + d_2}{2} = \frac{d}{2c}$$

where the result should be a constant.

In total there are 128 meantimed signals that are sent to the FASTBUS TDCs and the TEE Latching Time Digitizer.

Latching Time Digitizers

The purpose of the Latching Time Digitizers (LTD) is to accumulate time spectra for data rates of several MHz. There are 32 custom built LTD modules. The LTDs have a cycle time of 32 ns. Twelve clock pulses are used to clock a shift register. The LTDs take 2 signals from the front and back meantimers of a detector in coincidence and latches for a single beam burst. The time since the beam sync signal of the latched input is determined by using two 16 bit shift registers which are clocked 180° out of phase with respect to one another. The status of the shift registers are latched into another set of registers at the end of the beam pulse. These registers then drive 24 VME scaler channels (see below) which count how many times the bits were set. The depth of penetration of the input signal into the shift register during the shifting sequence then depends upon the time of the coincidence within the 32 ns cycle. This depth of penetration of the signal thus encodes the time of the coincidence. The LTDs also monitor the quality of the clock train for errors of "too many" or "too few" clock pulses. These gated clock trains for the LTDs are produced and distributed by two other sets of electronics:

- Clocking Gating Board: The custom built Clocking Gating Board (KGB) takes the 499 MHz clock signal from the CEBAF accelerator master oscillator and the "YO" signal provided by a beam pickoff monitor upstream of the G^0 target. This produces an $\sim$ 2 ns sync and the twelve $\sim$ 1 ns pulses of the clock train.

- Signal Duplication Boards: The custom built Signal Duplication Boards (SDBs) take a single copy of the gated clock train and a copy of the sync signal and provides 9 copies of each to be fanned out to the LTDs.

Scalers

The scalers which capture the time spectra from the LTDs are custom built VME latching scalers designed by LPSC-Grenoble. Data are accumulated for a 1/30 s macropulse. During the settle time of 500 μs between macropulses, the scaler data is latched into on-board memory and the scaler channels are cleared. The G^0 DAQ system then reads out the latched data for a macropulse while the scalers are accumulating data for the next macropulse.

3.10.2 French electronics

Splitter

There are 4 custom built splitter modules. Each splitter module symmetrically (1:1) and actively splits 64 PMT signals to provide inputs to the Constant Fraction Discriminator on the DMCH-16 X and FASTBUS ADCs.

DMCH-16X

The heart of the French time encoding electronics are 8 custom built boards known as the DMCH-16X (Discriminator, Mean-timer, time digital Converter, Histogramming, 16 channels within the vXi standard). Each board receives 32 PMT analog signals and builds 8 Time-of-Flight histograms associated with the detectors of two quarters of two octants. Most of the board's settings such as the CFD thresholds and differential non-linearity (DNL) for the TDCs are controlled via software.

Each DMCH-16X board contains 3 daughter boards containing: 16 CFD-MTs, 1 S-DMCH, and 1 G-DMCH. The G-DMCH is a generator used occasionally to check CFD thresholds and MT outputs. The S-DMCH keeps track of individual counts for the CFDs and MTs. Each DMCH-16X motherboard holds 2 TDCs which distribute data through FiFo buffers to 4 front-end digital signal processors (DSP)

where the ToF spectra are accumulated in different memory registers associated with each detector. At the end of an MPS, the 4 front-end DSPs and the DSP on the scaler S-DMCH send their data to another DSP known as the DSP concentrator, which transfers the block of data associated with one DMCH-16X board over the VME bus to the CPU board.

CHAPTER 4

Data Analysis

The first G^0 engineering run took place between October 2002-January 2003. The data analysis from this run was performed in several steps. First the raw measured asymmetries must be formed from the detector yields. Then the dead time must be corrected. False asymmetries due to helicity-correlated beam properties must be calculated and corrected. There is a correction for the background dilution factor and the background has an asymmetry associated with it that must be taken into account. Then the physics asymmetry can be extracted after correcting for the beam polarization, and radiative corrections can be applied.

4.1 Measured Asymmetry

The detector signals are accumulated during a helicity state (MPS). When the helicity is reversed by the Pockels cell that flips the helicity at 30 Hz, the data is read out by the electronics. The detectors count the desired elastically scattered protons as well as particles from other processes such as inelastic scattering from the aluminum windows of the target [62] and production of pions in the hydrogen target. An example of a time-of-flight spectrum is shown in Figure 4.1. These histograms

count how many particles have been detected in a detector. These histograms contain either 24 (NA electronics) or 128 (French electronics) time bins. Other types of data are also recorded during this spin-flip period, such as the integrated charge by the beam current monitors and integrated positions from the beam position monitors. For these ToF histograms the yield (Y) is the number of events (N) measured in each time bin normalized to the beam charge (Q) accumulated during that MPS. This charge normalization is needed since the event rate is a function of the beam intensity.

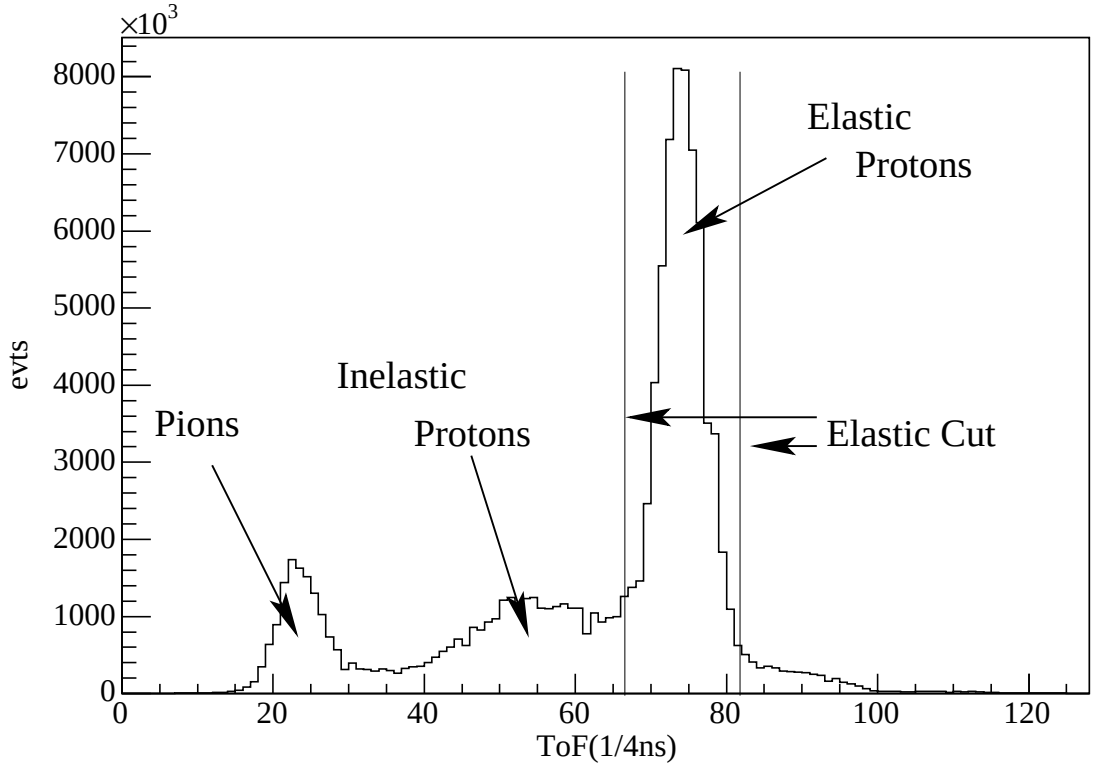

FIG. 4.1: *An example of a typical French Time-of-Flight spectrum from detector 8 with data taken during a one hour run..*

From the quartet, an asymmetry can then be computed for events within the elastic cut window, which is about 4 ns wide. This asymmetry for each detector

measured over a quartet can be written as:

$$A_{meas,det,qrt} = \frac{\left(\frac{N_1^+}{Q_1^+} + \frac{N_2^+}{Q_2^+}\right) - \left(\frac{N_1^-}{Q_1^-} + \frac{N_2^-}{Q_2^-}\right)}{\left(\frac{N_1^+}{Q_1^+} + \frac{N_2^+}{Q_2^+}\right) + \left(\frac{N_1^-}{Q_1^-} + \frac{N_2^-}{Q_2^-}\right)} \tag{4.1}$$

where N_i^s is the number of counts recorded for the i^{th} MPS of this quartet with beam helicity of sign s, and Q_i^s is the beam charge incident on the target during that MPS. Since the yield is the number of counts normalized to the charge, Equation 4.1 can be written as:

$$A_{meas,det,qrt} = \frac{Y_1^+ + Y_2^+ - Y_1^- - Y_2^-}{Y_1^+ + Y_2^+ + Y_1^- + Y_2^-}. \tag{4.2}$$

The measured asymmetry from all quartets within a run are averaged in each detector to give $A_{meas,det,run}$. The precision $\sigma_{meas,det,run}$ on the measurement is the root mean square of the standard deviation of the quartet asymmetry distribution divided by the square root of the number of quartets.

The next step is to take the weighted average and error of the measured asymmetries for all the runs for each detector:

$$A_{meas,det} = \frac{\sum_{run} \frac{A_{meas,det,run}}{\sigma^2_{meas,det,run}}}{\sum_{run} \frac{1}{\sigma^2_{meas,det,run}}} \tag{4.3}$$

$$\sigma_{meas,det} = \frac{1}{\sum_{run} \frac{1}{\sigma^2_{meas,det,run}}} \tag{4.4}$$

However, this is not the full story. Within the elastic proton peak cut window, there is some contamination, since not all the events are from elastic protons. Some of these events are inelastic protons produced in scattering within the target. This contamination must be removed in order to evaluate $A_{physics}$ for the elastic protons.

The measured asymmetry for each detector must be corrected to subtract the inelastic contribution (note the quartet helicity ordering denoted at “1” and “2”

above will now be suppressed for readability):

$$A_{meas,det} = \frac{Y_{el}^{+} - Y_{el}^{-} + Y_{inel}^{+} - Y_{inel}^{-}}{Y_{el} + Y_{inel}} \quad (4.5)$$

$$= \frac{Y_{el}}{Y_{el} + Y_{inel}}(A_{el}) + \frac{Y_{inel}}{Y_{el} + Y_{inel}}(A_{inel}) \quad (4.6)$$

where $A_{inel(el)}$ is the inelastic(elastic) asymmetry and $Y_{el(inel)}^{+(-)}$ is the number of right(left) handed elastic (inelastic) events. One can define the so-called 'inelastic dilution factor' as $d = \frac{Y_{inel}}{Y_{el}}$ and solve for the elastic asymmetry for each detector:

$$A_{el} = (1 + d)A_{meas} - dA_{inel}. \quad (4.7)$$

The error on the elastic asymmetry is given by:

$$\Delta A_{el} = \sqrt{(A_{meas} - A_{inel})^2 \Delta d^2 + d^2 \Delta A_{inel}^2 + (1 + d)^2 \Delta A_{meas}^2}. \quad (4.8)$$

After correcting for the inelastic contributions, other corrections must be applied to the elastic asymmetry to obtain the physics asymmetry, A_{phy}. The physics asymmetry must be corrected for not having 100% beam polarization, radiative effects, and false asymmetries due to helicity-correlated beam systematic effects.

The error on the elastic asymmetry has several contributions, as can be seen in Equation 4.8. For the G^0 forward angle production run, an error on the elastic asymmetry of ≤ 0.5 ppm is desired.

4.2 Statistical Widths

The statistical distribution of quartet asymmetries have a minimum variance width, $\sigma_{stat}(A_{qrt})$, determined solely from counting statistics, given by

$$\sigma_{stat} = \frac{1}{\sqrt{N_{proton}}} \quad (4.9)$$

where N_{proton} is the number of detected protons in one quartet. Thus if the measurement is purely statistical, the width of the distribution of the measured asymmetries,

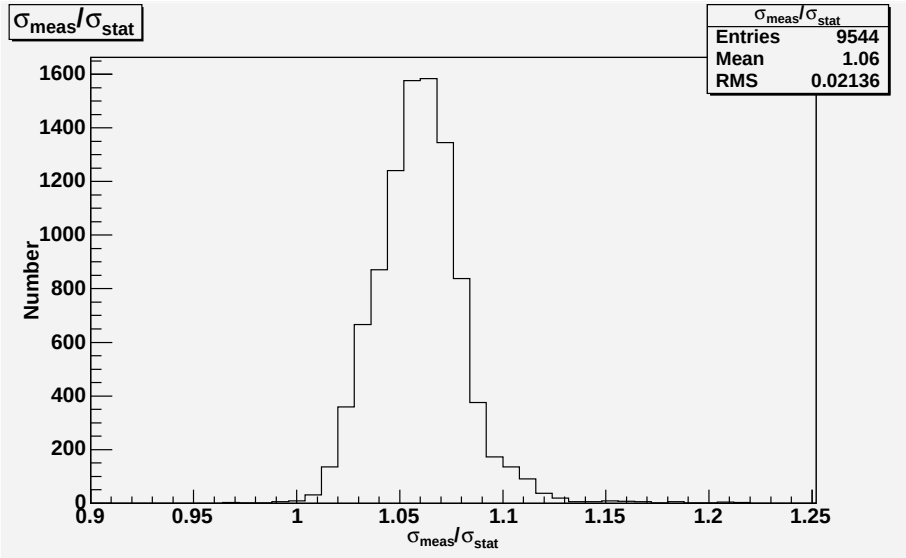

FIG. 4.2: *The ratio of the measured quartet asymmetry distribution widths to the width expected solely from counting statistics for the detectors* $\frac{\sigma_{meas}}{\sigma_{stat}}$. *Deviations from 1.0 indicate the presence of instrumental noise in the measurements.*

σ_{meas}, is:

$$\sigma_{meas} = \frac{1}{\sqrt{N_1^+ + N_2^+ + N_1^- + N_2^-}} \tag{4.10}$$

for each helicity period.

A comparison between the measured quartet asymmetry distribution widths with the statistical width is an indicator of systematic effects, since instrumental noise can broaden the width of the measured distribution. The number of counts used in this calculation has been corrected for dead time (see Section 4.6). The measured statistical widths due to the number of counts for each detector is on the order of 3800 ppm. This makes sense, since the detector rate is about 0.5 MHz, the measurement interval is 1/30 second, so the number of scattered protons/macropulse

$$0.5\,\text{MHz} \times 1/30\,\text{second} = 16667. \tag{4.11}$$

Obtaining the number of events in a quartet requires the result from Equation 4.11 to be multiplied by 4 for four helicity windows in one quartet. Using Equation 4.2 yields

$A_{meas,qrt,det} \sim 3800$ ppm. All detectors were measured to have $\frac{\sigma_{meas}}{\sigma_{stat}} \sim 1.06$ (see Figure 4.2) implying that all measurements are dominated by counting statistics.

4.3 Cuts

The measured raw asymmetry had several cuts applied event by event in order to improve the statistical properties of the results. These were applied by the G0Analysis replay engine which produces the histograms and NTuples, to be read by ROOT, from the raw CODA data files. The first check is to be sure that an event in the MPS make up a good quartet. The code will check the reported helicity (which has been delayed by 8 helicity windows) against an algorithm for helicity prediction in G0Analysis. These cuts defined a good MPS. A good quartet requires that all MPSs in a quartet are good and have the correct helicity pattern. Asymmetries are calculated for good quartets only. After this cut, two more sets of cuts were applied:

- Beam Cuts:

  If the beam current read out by the beam current monitor (see Section 3.5.6) is less than 5μA, that MPS along with the next 2000 MPS after beam recovery are removed. This is because it has been noted, by looking at the luminosity monitors, that the target takes approximately a minute to settle down after beam is restored.

- Detector Cuts

  Both North American and French electronics have error indicators in the data stream. The North American electronics (see Section 3.10.1) have error indicators on the LTD boards to note if the LTD is seeing "too many" or "too few" micropulses within the 30 Hz helicity window. The French electronics (see Section 3.10.2) are armed with "alerts" which count the number of overflow words in

a DMCH module. These counters are looked over first, then data from a detector is tagged as "bad" when the associated counter reads a non-zero value.

Sometimes a detector yield would "jump" up or down in a non-statistical manner which thereby creates a large systematic asymmetry. To identify this, G0Analysis takes the first 100 MPS of each run for each detector and calculates the mean and width of the yield distribution, for each detector and for each ToF bin, as a reference value. A $\pm 10\sigma$ cut around the reference value is then applied to each ToF bin and a detector is tagged as "bad" if any ToF bin fails the cut.

4.4 Raw Asymmetry

The raw asymmetry is calculated for each quartet for each detector from the normalized yield

$$A_{qrt,det} = \frac{Y_1^+ + Y_2^+ - Y_1^- - Y_2^-}{Y_1^+ + Y_2^+ + Y_1^- + Y_2^-}. \tag{4.12}$$

The normalized yield is the yield for one MPS divided by the beam charge accumulated during that MPS

$$Y_{+\text{ or }-}^{MPS=1\text{ or }2} = \frac{(d\sigma/d\Omega) L \Delta\Omega T_{MPS}}{Q_{MPS}} \tag{4.13}$$

$$= N_{MPS}/Q_{MPS} \tag{4.14}$$

where $d\sigma/d\Omega$ is the differential cross section for $\overrightarrow{e}$p scattering, L is the luminosity, $\Delta\Omega$ is the solid angle acceptance, N_{MPS} is the number of counts in a detector during a macropulse, Q_{MPS} is the charge accumulated during a macropulse and T_{MPS} is the length of time for one macropulse. Figure 4.3 is a plot of the measured raw asymmetries as a function of detector number.

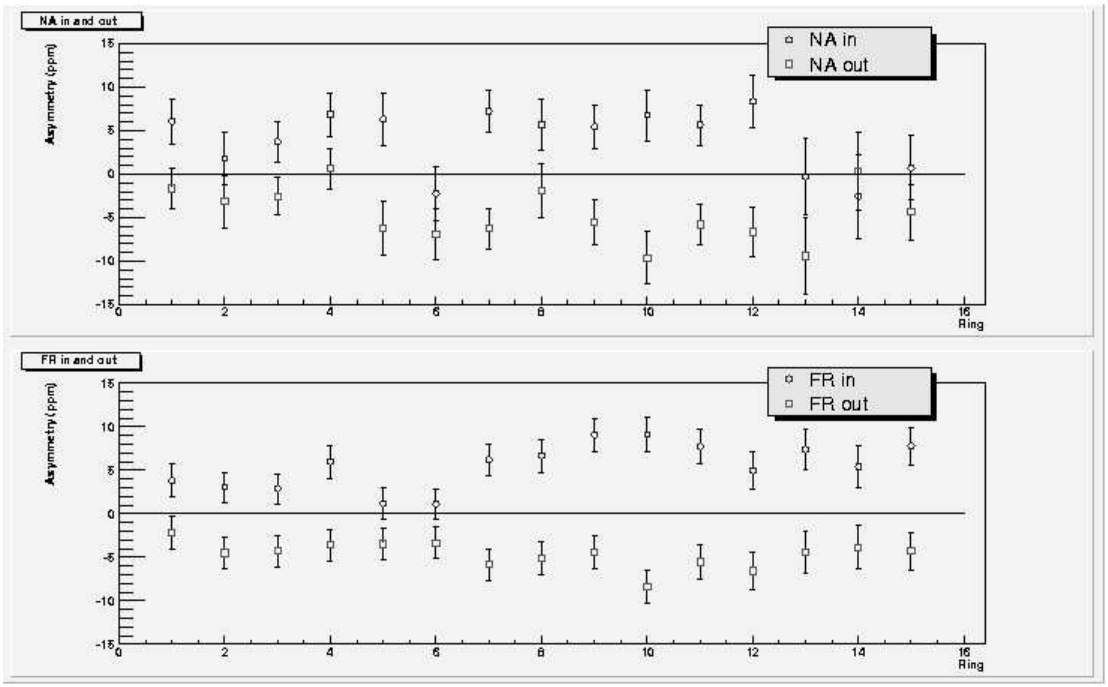

FIG. 4.3: *North American and French (out-in) raw asymmetries. The insertable halfwave plate reverse the sign of the raw asymmetry. By subtracting the 'in' asymmetries from the 'out' asymmetries, one can combine the two sets of results. The error bar is found by adding the 'in' and 'out' errors in quadrature*

4.5 Passive Sign Reversal

In order to establish the validity of the measured raw asymmetry in a parity violation experiment it is important to demonstrate that the results are being produced by helicity-dependent dynamics in the cross section instead of by spurious electronic effects. Passively reversing the sign of the measured raw asymmetry is a powerful way of searching for potentially unforeseen systematic effects.

By periodically (every two or three days) inserting a halfwave plate at the source, the helicity of the circularly polarized light produced by the G^0 TIGER laser (see Section 3.5.1) is passively reversed. This in turn reverses the electron helicity pattern without changing any other device systematics. If the analysis software does not take into account the insertion of the halfwave plate, the opposite sign for the

asymmetry will be calculated.

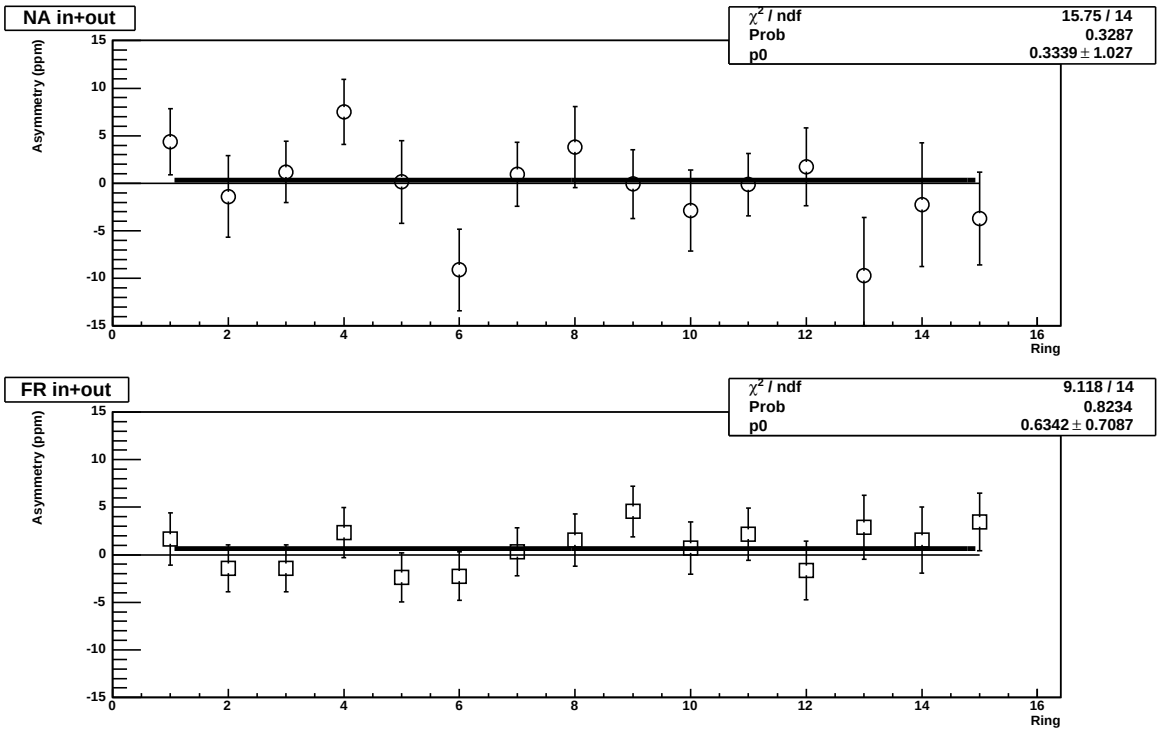

FIG. 4.4: *North American (NA) and French (FR) (in+out) raw asymmetries. Under the raw asymmetry sign reversal, due to the insertable halfwave plate, adding the 'in' and 'out' states should yield a zero result.*

It is clear from Figure 4.3 and Table 4.1 that there is a correlation between the presence of the halfwave plate and the sign of the asymmetry. From Figure 4.4, it can be seen that adding the 'in' and 'out' data results in zero, as expected. When the halfwave plate is inserted, the sign of the asymmetry is corrected when combined with the data set.

Det	NA OUT (ppm)	NA IN (ppm)	NA OUT-IN (ppm)	Fr OUT (ppm)	Fr IN (ppm)	Fr OUT-IN (ppm)
1	-1.7 ± 2.3	6.1 ± 2.6	-3.63 ± 1.71	-2.1 ± 2.0	3.8 ± 1.9	-3.00 ± 1.37
2	-3.2 ± 3.0	1.8 ± 3.0	-2.48 ± 2.14	-4.5 ± 1.8	3.1 ± 1.7	-3.78 ± 1.24
3	-2.6 ± 2.2	3.7 ± 2.3	-3.11 ± 1.60	-4.3 ± 1.8	2.9 ± 1.7	-3.60 ± 1.24
4	0.6 ± 2.3	6.9 ± 2.5	-2.89 ± 1.71	-3.6 ± 1.9	6.0 ± 1.9	-4.80 ± 1.32
5	-6.2 ± 3.1	6.3 ± 3.1	-6.26 ± 2.17	-3.5 ± 1.8	1.1 ± 1.8	-2.31 ± 1.29
6	-6.9 ± 3.0	-2.2 ± 3.1	-2.57 ± 2.14	-3.4 ± 1.8	1.1 ± 1.8	-2.22 ± 1.27
7	-6.3 ± 2.3	7.2 ± 2.5	-6.70 ± 1.68	-5.9 ± 1.8	6.2 ± 1.8	-6.04 ± 1.26
8	-1.9 ± 3.1	5.7 ± 2.9	-3.92 ± 2.12	-5.1 ± 2.0	6.7 ± 1.9	-5.90 ± 1.37
9	-5.5 ± 2.6	5.5 ± 2.6	-5.49 ± 1.81	-4.5 ± 1.9	9.0 ± 1.9	-6.80 ± 1.33
10	-9.6 ± 3.0	6.8 ± 3.0	-8.17 ± 2.12	-8.4 ± 2.0	9.1 ± 1.9	-8.76 ± 1.37
11	-5.8 ± 2.3	5.7 ± 2.3	-5.74 ± 1.65	-5.5 ± 2.0	7.7 ± 1.9	-6.65 ± 1.38
12	-6.7 ± 2.8	8.4 ± 3.0	-7.45 ± 2.04	-6.6 ± 2.2	4.9 ± 2.2	-5.75 ± 1.53
13	-9.4 ± 4.3	-0.3 ± 4.4	-4.57 ± 3.08	-4.5 ± 2.4	7.4 ± 2.4	-5.95 ± 1.68
14	0.4 ± 4.4	-2.6 ± 4.8	1.39 ± 3.24	-3.9 ± 2.5	5.4 ± 2.4	-4.65 ± 1.74

TABLE 4.1: *Comparison of North American and French raw asymmetries under reversal of the halfwave plate. When the halfwave plate is inserted into the laser path, the handedness of the light reverses thus causing the handedness of the liberated electrons to be opposite to that of the Pockels cell. If there aren't any systematic effects, the asymmetry magnitudes should be the same but with opposite sign.*

4.6 Dead Time Corrections

The asymmetry had to be corrected to take into account electronic dead time. The electronic dead time is caused when the electronics are still busy after/during the processing of an event. The G^0 custom electronics have been designed to measure high rates on the order of 1 MHz with a controlled dead time. Dead time from the North American electronics can come from the LTDs and the CFDs. Both North American and French electronics are set to neutralize the next pulse after an event (known as Next-Pulse-Neutralization or NPN) and allows for an exact calculation of dead time. The probability of being dead, f, is proportional to the rates of events triggering the electronics. This will cause the measured yield Y_{meas}, to differ from the true yield, Y_{true} as

$$Y_{meas} = (1 - f)Y_{true} \tag{4.15}$$

Controlling the dead time is mandatory since the number of events are expected to vary in a helicity-correlated manner arising from the charge asymmetry A_q. Thus the dead time can introduce a false asymmetry

$$A_{false} = -f \times A_q \tag{4.16}$$

The North American LTDs and French time encoding electronics record only a four-fold coincidence and therefore cannot be used to correct for single events, where singles occur when one to three (but not all four) PMTs fire. The singles are mainly pions that come before the protons in the time spectrum, and so a singles hit will then cause the loss of the proton count. This means that on average the electronics are dead to protons for one micropulse.

In the North American electronics, the dead time was dominated by the CFDs. The CFDs should work by taking the original signal and producing two more signals. One signal is a duplicate of the original but delayed in time and the other signal is a fraction of the original signal amplitude. The CFD then will fire when the original signal is above a certain threshold and the two duplicate signals intersect. What happened during the 2002-2003 engineering run was that sometimes a smaller detector signal would precede a larger detector signal, and this would cause the duplicate signals to intersect before the original signal would cross threshold. This produces an apparent dead time in the electronics. This effective dead time was about 70 ns for the North American electronics. This problem will be corrected in future running by adjusting the delay and fraction in the CFDs to prevent these sub-threshold particle signals from affecting the larger particle detector signals.

The dead time correction is

$$N_{true} = \frac{N_{raw}}{1 - f} \tag{4.17}$$

where N_{true} is the true yield, N_{raw} is the raw yield, and f is the dead time fraction. The overall dead time fraction for the NA detectors was found to range from 3%

to 11% for detectors 1 through 14. The technique for extracting the dead time fraction is to plot the detector yield versus beam current or detector asymmetry versus charge asymmetry. The overall dead time fraction is the sum of the dead time due to singles and the dead time due to coincidence

$$f = R_{coinc}\tau_{coinc} + R_{singles}\tau_{singles} \tag{4.18}$$

where $R_{coinc}(R_{singles})$ is the rate due to the coincidence(singles), and $\tau_{coinc}(\tau_{singles})$ is the dead time due to coincidence(singles). The dead time due to coincidences is given by

$$\tau_{coinc} = 0.5 + (j-1) + 6.5 + 32 \tag{4.19}$$

where j is the timebin of the detected particle. The dead time due to singles was found to be 70 ns (as explained above) and this dominates the dead time, thus the dead time fraction can be written as

$$f = (R_{coinc} + R_{singles}) \times 70 \text{ ns} \tag{4.20}$$

where R_{coinc} is determined from the LTDs and $R_{singles}$ is determined from FASTBUS data.

The French electronics singles dead time from the CFDs was found to be 35 ns. The dead time due to the meantimers was found to be 32 ns.

4.7 Correcting Helicity-Correlated Beam Properties

Helicity-correlated fluctuations in the beam parameters such as position, angle, energy and charge can cause false asymmetries to appear in the data. This can be seen if one of the beam parameters mentioned above is on average, different between

the two different helicity states. If this is the case, then the measured yield will be different between the two different helicity states, thus producing a false asymmetry. These fluctuations are the results of reversing the voltage on the helicity Pockels cell. Besides producing circularly polarized light, this voltage reversing might produce some helicity-correlated systematic, e.g. the angle of the emerging laser light might be different in one state versus another. This systematic then translates to slightly different types of helicity-correlated laser light hitting the GaAs crystal differently in a helicity-correlated manner which in turn produces an asymmetry in the electron beam between helicity states (see Figure 4.5). These helicity-correlated fluctuations in beam parameters manifest themselves as false asymmetries that appear in the data. This false asymmetry requires a systematic correction to the measured asymmetry.

This can be illustrated assuming a linear relationship between the measured yield Y and the beam parameter x_i, where the beam parameter can be any of the six mentioned above. The yield due to beam fluctuations can be written as

$$Y = \alpha x_i. \tag{4.21}$$

The measured yield, $Y^{+,-}_{meas}$, is then a combination of the parity-violating yield, $Y^{+,-}$, and the yield due to the correlation with the beam parameter

$$Y^{+,-} = Y^{+,-} + \alpha x_i^{+,-}. \tag{4.22}$$

The beam parameter difference can be written as

$$\delta x_i = x_i^+ - x_i^- \tag{4.23}$$

where the superscript +(-) indicates positive (negative) helicity state.

Forming the asymmetry

$$A_{meas} = \frac{Y^+ - Y^-}{Y^+ + Y^-} \tag{4.24}$$

substituting in the yield from Equation 4.22, one obtains

$$A_{meas} = \frac{Y^+ - Y^- + \alpha(x_i^+ - x_i^-)}{Y^+ + Y^- + \alpha(x_i^+ + x_i^-)}. \tag{4.25}$$

Assuming $Y^{\pm} >> \alpha x_i^{\pm}$

$$\begin{aligned} A_{meas} &= \frac{Y^+ - Y^- + \alpha\delta x}{Y^+ + Y^-} \\ &= \frac{Y^+ - Y^-}{Y^+ + Y^-} + \alpha\frac{\delta x}{Y^+ + Y^-} \\ &= A_{corr} + \alpha\frac{\delta x}{2 < Y >} \end{aligned} \tag{4.26}$$

where the average yield is given by $< Y >= \frac{1}{2}(Y^+ + Y^-)$, and α is identified as the detector response to the beam parameter. This can finally be written as

$$A_{meas} = A_{corr} + \frac{1}{2 < Y >} \sum_{i=1,6} \delta x_i \frac{\partial Y}{\partial x_i}. \tag{4.27}$$

The detector yield response to the various beam parameters, $\frac{\partial Y}{\partial x_i}$, must be extracted from the data. This can be done by looking at the natural motion of the beam by assuming a linear response of the yields to the beam parameters

$$Y_{corr} = Y_{meas} - \sum_{i=1,6} \delta x_i \frac{\partial Y}{\partial x_i} \tag{4.28}$$

where Y_{meas} is the raw yield of the detector, x_i is one of the six beam parameters (x and y position at target, x and y angle at the target, charge at the target and the energy). The helicity-correlated beam position and angle are calculated using two BPMs closest to the G^0 target. The energy difference is measured using a BPM in a dispersive region in the arc. The beam charge is measured from the standard Hall C BCMs.

The slopes, $\frac{\partial Y_{meas}}{\partial x_i}$, are found by inverting the covariance matrix in the following equation that relates the slopes to the mean correlation between the yield and

the various beam parameters

$$(< \delta Y \cdot \delta x_i >) = \sum_{i=1,6} (< \delta x_i \cdot \delta xj >) \left(\frac{\partial Y}{\partial x_i} \right) \tag{4.29}$$

where $(\delta x_i \cdot \delta xj)$ is a 6×6 beam parameter covariance matrix, and $(\delta Y \cdot \delta x_i)$ is the covariance of the yield and beam parameters. This variation in the yield to the beam parameters characterizes the sensitivity of the G^0 apparatus to changes in beam properties. Figure 4.6 shows the percent yield on detector 1 for all the octants as the beam properties are being changed. In general, diametrically opposing octants should have opposing sensitivities and thus opposing signs. It is due to this behavior that the sensitivities due to changes in beam position and angle are largely canceled out between diametrically opposing octants when one takes the mean.

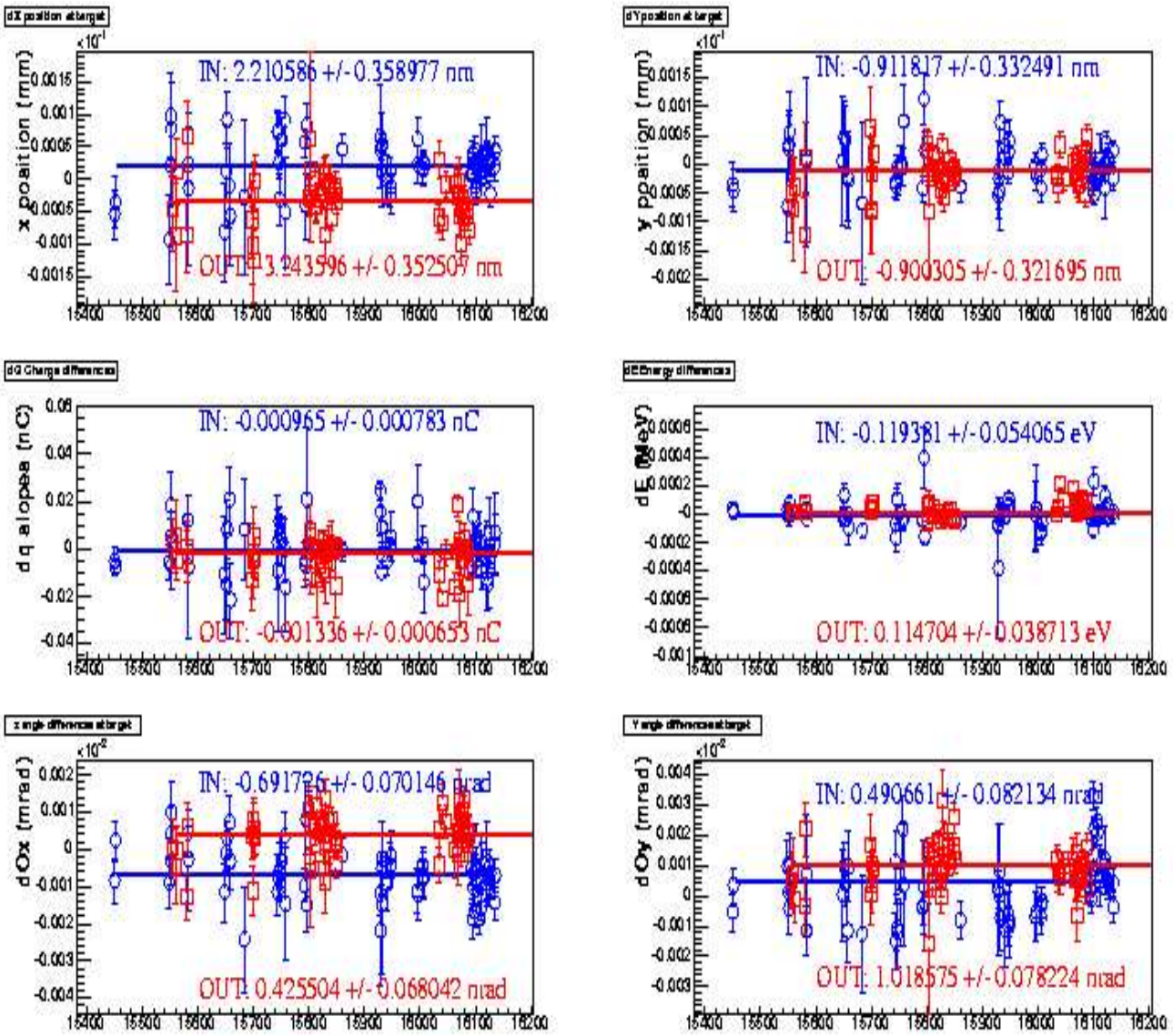

FIG. 4.5: *Plots of the helicity-correlated beam properties. The position differences and angle differences are the values projected onto the target from the BPMs G0 and G0B. The energy difference is measured from BPM 3C12.*

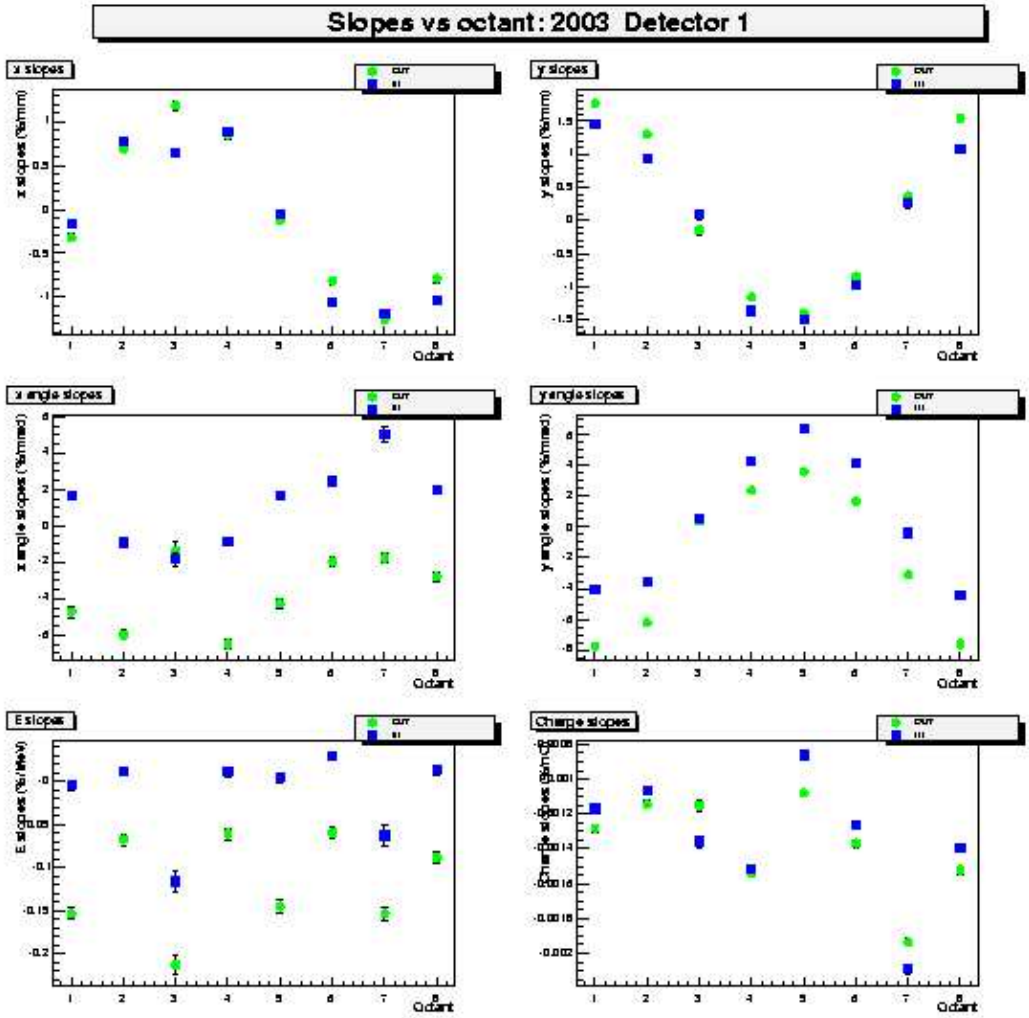

FIG. 4.6: *Detector sensitivity slopes plotted as a function of octant.*

Beam Parameter	x position	y position	x angle	y angle	Energy	charge
Octant Average slopes	0.04 %/mm	0.17 %/mm	-1.73 %/mrad	-1.08 %/mrad	-0.08 %/MeV	-0.001 %/nC
helicity-correlated difference	-3.24 nm	-0.9 nm	0.43 nrad	1.02 nrad	1.15 eV	-0.001 nC
False Asymmetry correction	-0.015 ppm	-0.015 ppm	-0.074 ppm	-0.11 ppm	-0.01 ppm	0.013 ppm

TABLE 4.2: *IHWP out false asymmetries. The data are from 49 asymmetry runs.*

Beam Parameter	x position	y position	x angle	y angle	Energy	charge
Octant Averaged slopes	0.06 %/mm	0.090 %/mm	0.92 %/mrad	0.30 %/mm	0.01 %/MeV	-0.001 %/nC
helicity-correlated differences	2.21 nm	-0.91 nm	-0.69 nrad	0.49 nrad	-1.19 eV	-0.001 nC
False Asymmetry correction	0.014 ppm	-0.008 ppm	-0.063 ppm	0.015 ppm	-0.001 ppm	0.008 ppm

TABLE 4.3: *IHWP in false asymmetries. The data are from 58 asymmetry runs.*

The resulting octant averaged slopes as well as the associated asymmetries are shown in Table 4.2 for the insertable half wave plate out state and in Table 4.4 for the insertable halfwave plate in state. The false asymmetry A_{false} due to the helicity-correlated beam parameters as a function of insertable halfwave plate is found to be:

$$\text{IHWP OUT: } A_{false} = -0.210 \pm 0.616\,\text{ppm} \tag{4.30}$$

$$\text{IHWP IN: } A_{false} = -0.037 \pm 0.522\,\text{ppm} \tag{4.31}$$

$$\text{IHWP IN+OUT } A_{false} = -0.11 \pm 0.40\,\text{ppm}. \tag{4.32}$$

The measured asymmetry is then corrected for helicity-correlated false asymmetry by

$$A_{corr} = A_{meas} - A_{false} \tag{4.33}$$

where A_{corr} is the corrected measured asymmetry.

Det	NA A_{corr}	Fr A_{corr}
1	-3.74 ± 1.76	-3.11 ± 1.43
2	-2.59 ± 2.18	-3.89 ± 1.30
3	-3.22 ± 1.65	-3.71 ± 1.30
4	-3.00 ± 1.75	-4.91 ± 1.38
5	-6.37 ± 2.20	-2.42 ± 1.35
6	-2.68 ± 2.18	-2.33 ± 1.33
7	-6.81 ± 1.73	-6.15 ± 1.32
8	-4.03 ± 2.16	-6.01 ± 1.43
9	-5.60 ± 1.85	-6.91 ± 1.39
10	-8.28 ± 2.16	-8.87 ± 1.43
11	-5.85 ± 1.70	-6.75 ± 1.43
12	-7.56 ± 2.08	-5.85 ± 1.58
13	-4.68 ± 3.10	-6.06 ± 1.73
14	1.28 ± 3.27	-4.76 ± 1.79

TABLE 4.4: *The measured asymmetries corrected for false asymmetries due to helicity-correlated beam properties for detectors 1-14.*

4.8 Inelastic Dilution Factors

4.8.1 French Results

The French time-of-flight (ToF) spectra with its fine 128 binning (versus the North American ToF with its more coarse and non-equal 24 binning) is the first data set to be looked at for extracting the inelastic dilution factors for each detector. Each spectrum was fit with one Gaussian for each of the three particle distributions: pion, inelastic proton and elastic proton (see Figure 4.7). Numerical integration was employed to find the contributions due to the elastic and inelastic protons within the 4 ns wide elastic cut window. A total of 106 runs were fit. The inelastic dilution factors of each detector were stable to 3% over the set of runs assuming the cut does not change (see Figure 4.8).

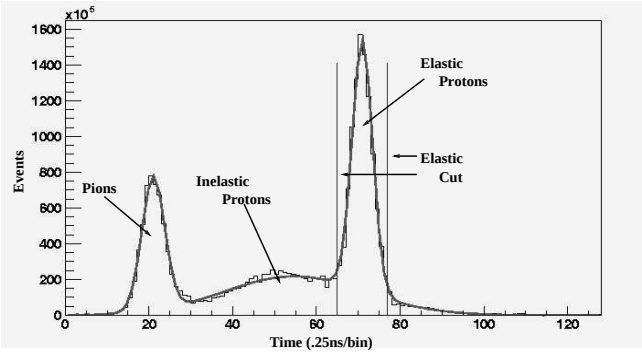

FIG. 4.7: *An example of a 3 Gaussian fit to French Detector 9 Octant 2. Each particle distribution has been fit to a Gaussian. The vertical lines around the elastic peak constitute the elastic cut for this spectrum.*

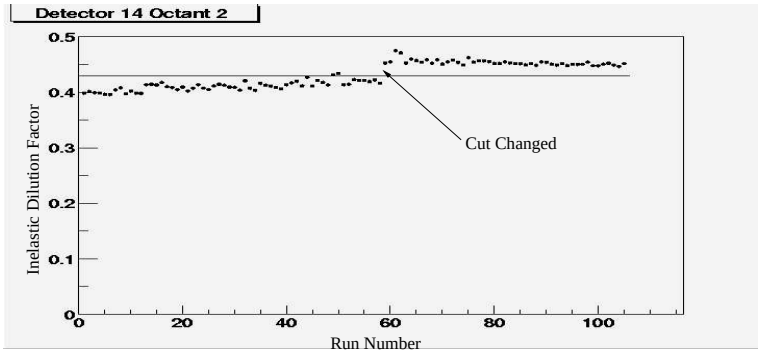

FIG. 4.8: *An example of the stability of the inelastic dilution factor over 106 runs for detector 14 Octant 2. The abrupt change near run 60 is due to the elastic cuts being changed.*

The contributions to the percent errors on the extracted inelastic dilution factors (which are added in quadrature to produce the final percent error) are :

- Error on the fit:
  - Statistical precision of the fit: the dispersion between the inelastic dilution factors for the same detector and same octant, with the same cuts for different runs. This was found to be 0.3%.
- Error on the shape of the fit: the dispersion between using different plausible mathematical equations to describe the same spectra. This was found to be 1%.

- Error on the average over the octants: the dispersion between the dilution factors for different octants. Having different cuts for the same detector but for a different octant or having different signal amplitude compared to the thresholds might cause this dispersion. This was found to be 4%.

Since there was a 5% error between dilution factors for each detector between the octants, the inelastic dilution factors for each detector was averaged over the 4 French octants (see Figure 4.9 and Table 4.5).

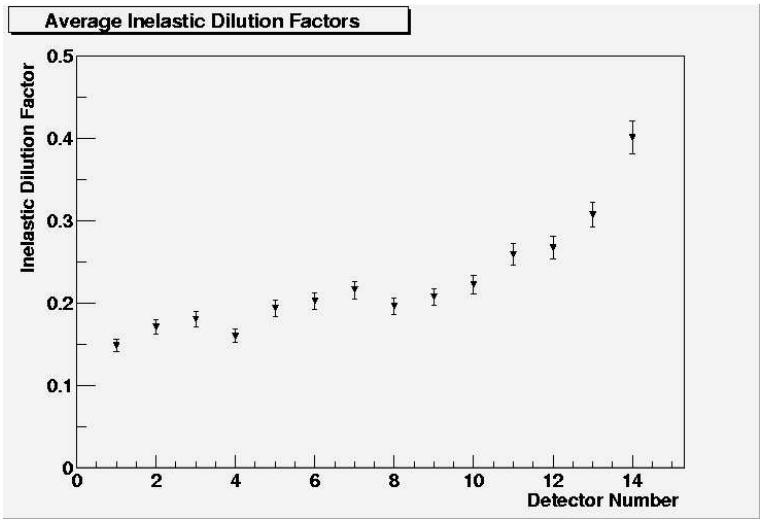

FIG. 4.9: *French inelastic dilution factors as a function of detector number, averaged over 4 French octants, using the 3 Gaussian fit.*

4.8.2 North American Results

The North American (NA) time-of-flight (ToF) spectra were plagued by differential non-linearity (DNL) (see Figure 4.10). The NA ToF spectra was expected to have time bins that were 1 ns wide (except for the first bin which was 6.5 ns wide by design). The DNL manifested itself as deviations from the 1 ns width. The DNL

Det	Inelastic Dilution Factor	Error
1	0.148	0.007
2	0.171	0.009
3	0.180	0.009
4	0.160	0.008
5	0.194	0.010
6	0.202	0.010
7	0.216	0.011
8	0.200	0.010
9	0.210	0.010
10	0.222	0.011
11	0.259	0.013
12	0.267	0.013
13	0.307	0.015
14	0.401	0.020

TABLE 4.5: *The average inelastic dilution factors for the French detectors for the cuts on the elastic peak which were $\sim$ 4 ns. The error represents the final absolute error on the dilution factor for each detector.*

created time bins ranging from $\sim$ 0.5-2 ns. The DNL was significantly larger than expected, and the cause(s) for this large DNL are only imperfectly understood at the present, but appear to be at least partly due to the clock signal.

The North American electronics dictate the width of the bins of the North American ToF spectra by forming the beginning and ending of the bins on the rising and falling edge of a clock signal supplied by accelerator. If the clock train is made up of perfect square waves, then the bins in the North American ToF spectra will be 1 ns wide. If the clock train is asymmetric, then the bins will deviate from 1 ns, as observed during the 2002-2003 G^0 commissioning run. This makes fitting the North American ToF spectra to find the inelastic dilution factors more difficult than for the French ToF.

The DNL can be measured with "white noise" runs. A white noise run consists of an LED shining on a photo-multiplier tube whose signal is then fed into the North American electronics. For bins of equal width, a flat ToF spectrum should be produced for bins 2 though 24. Since the North American ToF does suffer from

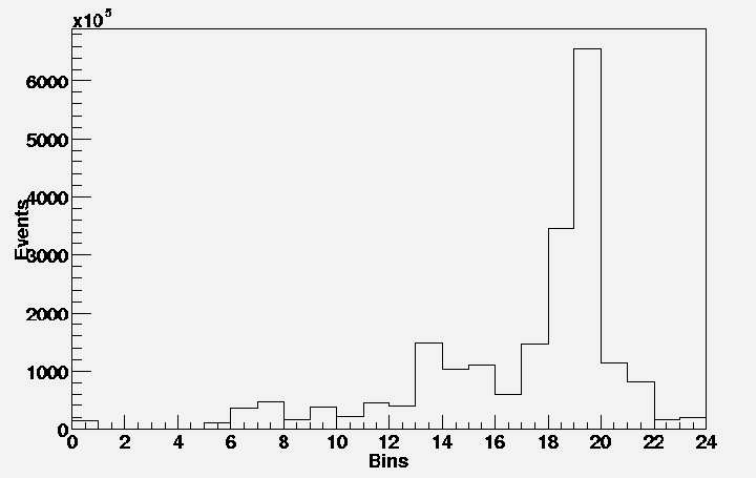

FIG. 4.10: *An example of a time-of-flight spectra from a North American detector. The jagged binning is due to the differential non-linearity that causes the bins not to be of equal time widths.*

the DNL problem, the bins are not of equal widths and by normalizing each of the bins, the width of each bin can be found (see Figure 4.11). The qualitative pattern of the DNL tends to alternate between ~ 0.5 and ~ 1.5 ns wide bins although there are significant deviations from this pattern. Another difficulty with the DNL is that it changes with time, on time scales of the order of a day, as can be seen in both Figures 4.11 and 4.12.

To evaluate what effect the DNL had on extracting the inelastic dilution factors, a simulation of the ToF spectra without DNL for each detector was produced. Using the fit parameters obtained from the French ToF for the elastic and inelastic proton distributions, the ToF spectra for detectors 1-14 were simulated with very fine binning (see Figure 4.13).

Three white noise spectra were taken during the G^0 commissioning run and three white noise runs were taken later after the commissioning run; with these six

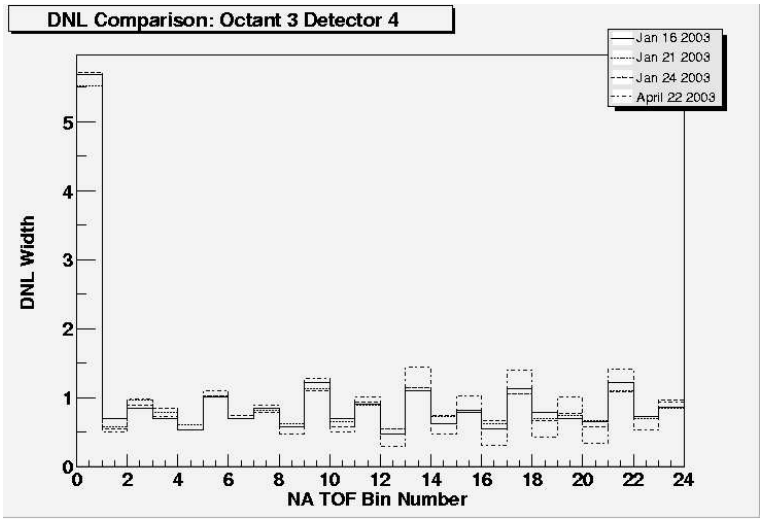

FIG. 4.11: *An example of several white noise spectra for North American octant 3 detector 4. The ordinate axis is the width of each bin along the abscissa axis. Note that the bins deviate from the expected 1 ns width. This deviation is the so-called 'differential non-linearity' or DNL. Also note that the DNL changes with time.*

runs, a total of 212 measurements[1] of the DNL exist. The simulated spectra were then recast into North American binning and the 212 measured DNLs were applied (see Figure 4.13).

These spectra were then fit to 2 Gaussians (one for the inelastic proton and one for the elastic proton distributions) and numerical integration was applied to find the inelastic dilution factors. When the results for each detector were histogrammed, a bimodal distribution was found (see Figure 4.14). This bimodal distribution was due to how the DNL was applied to the ToF spectra. The DNL creates a bias weighting within the elastic cut (the first bin after the cut is typically either 0.5 ns wide or 1.5 ns wide). The actual inelastic dilution factor[2] was distributed around only one value (see Figure 4.14). This implied that the DNL must be corrected to extract the inelastic dilution factors correctly.

[1] *[(16 × 4) detectors] × [6 measurements] = 256 DNL measurements of which 44 had to be excluded because of detector malfunction.*

[2] *Computed with the initial binning.*

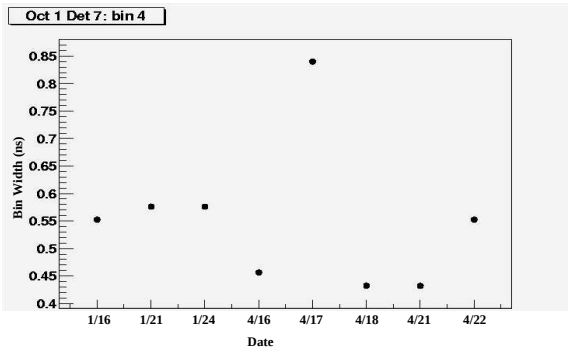

FIG. 4.12: *An example of one bin's variation over 8 measurements over 4 months for detector 7 octant 1. Note that on April 17th the bin width changed by nearly a factor of two from the day before and the day after.*

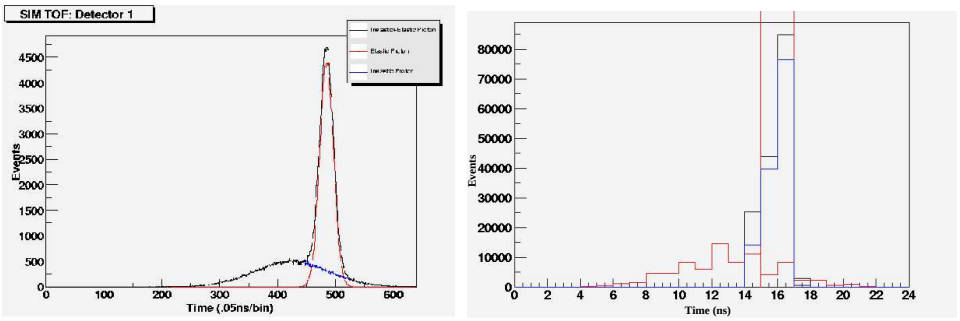

FIG. 4.13: *The plot on the left is a simulated North American ToF spectrum using the fit parameters obtained from the French ToF. The plot on the right is a simulated North American ToF spectra with DNL. Each simulated North American ToF spectra was produced 212 times with different DNLs.*

The DNL was corrected by using variable binning and normalizing each bin to the variable bin width. Only the three sets of North American white noise runs taken during the 2002-2003 G^0 commissioning run were utilized to fix the North American ToF spectra. An example of a corrected and uncorrected North American ToF spectrum is shown in Figure 4.15.

Since the DNL changes with time, one set of white noise measurements will not fix the whole North American data set. Figure 4.17 shows a ToF spectra for the same detector with the same DNL correction but for different runs where one run passes the subjective test (the ToF spectrum is "smoothed" out) and the other

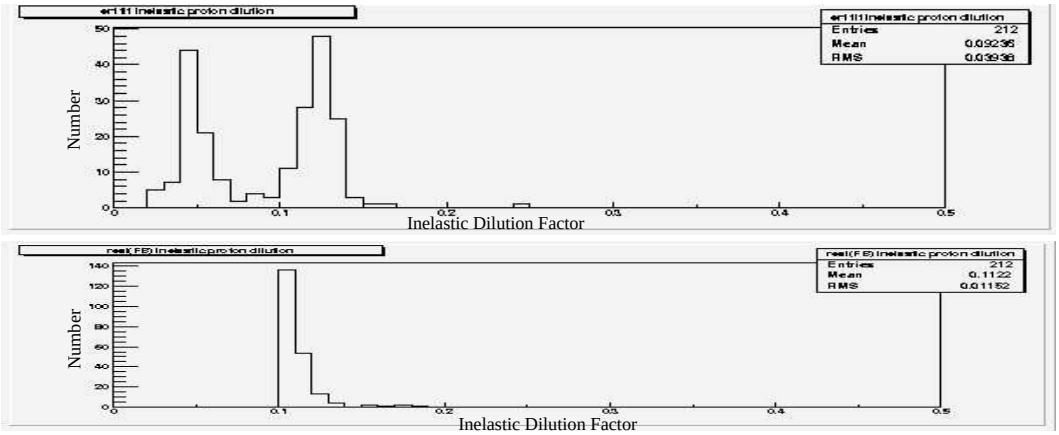

FIG. 4.14: *The top histogram is an example of the simulated extracted inelastic dilution factors for a North American detector. The bottom histogram are the results of the "true" inelastic dilution factor from the simulated corrected North American ToF spectra.*

fails (the ToF spectrum still appears "jagged"). To further complicate this, since the DNL can change one day to the next day, one white noise spectra might fix the DNL for many runs while failing for some of the intermediate runs within the run set (see Figure 4.16). Looking at the relative minimum in relation to all other runs, the sum of the differences between the fit and the data (as shown versus run number in Figure 4.18) was a useful (though not definitive) guide in determining which runs were fixed by which white noise spectra.

With only three sets of white noise spectra which correct the asymmetry runs near it in time to the white noise run, only 46 runs out of 124 were able to be corrected. There was an overlap of 8 runs between the 3 sets of data corrected by the 3 different white noise runs.

After the DNL was corrected on the 46 runs, a three Gaussian fit to each particle distribution and the standard 4 ns database cuts were applied. Numerical integration was employed to find the inelastic dilution factors.

The contributions to the percent errors (added in quadrature to obtain the final

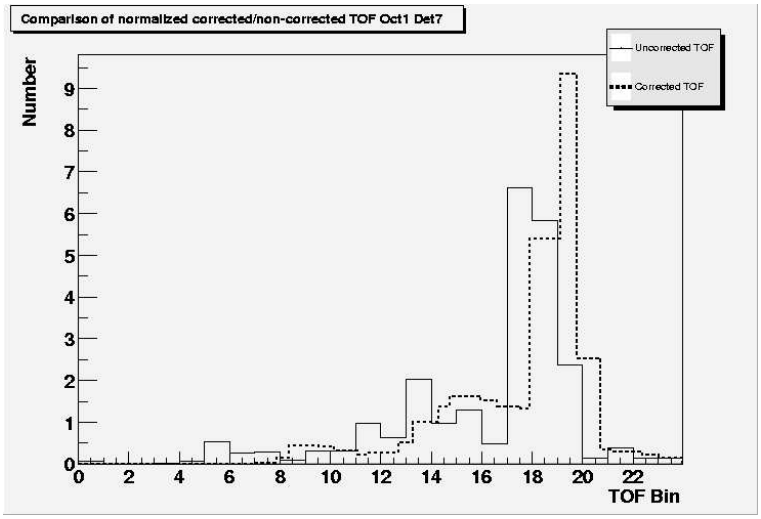

FIG. 4.15: *Corrected and uncorrected North American ToF spectrum.*

percent error) on the inelastic dilution factors are:

- Error on the fit: the dispersion of the fit on a detector over 46 runs. This is important since the dilution factors are sensitive to the size of the cut window which is known to change over the data set. This was found to be 14%.

- Error on the knowledge of the DNL: the dispersion between the results from the 8 runs that are corrected by the 3 white spectra. This was found to be $\sim 1\%$.

- Error on the shape of the fit: the dispersion between different mathematical equations to describe the same spectra. This was found to be 1%.

- Error on the average over octants: the dispersion between the dilution factors for different octants. Having different cuts for the same detector but for a different octant or having different set of thresholds might cause this dispersion. This was found to be 12%. This is important in that it suggests that instead of quoting an inelastic dilution factor for each detector for each octant, one can quote the inelastic dilution factor for each detector averaged over the octants.

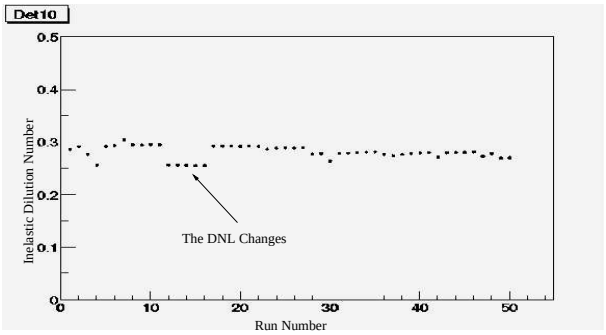

FIG. 4.16: *Stability of the North American inelastic dilution factors over ∼50 runs for a typical detector. Note that for ∼5 runs the inelastic dilution factors have changed in a similar fashion as noted in Figure 4.12. This is presumably due to the DNL changing with time. ToF spectra for these runs resemble the failing ToF spectra in Figure 4.17. These failing runs were not used in calculating the inelastic dilution factors.*

The results of the extraction of the North American inelastic dilution factors can be found in Figure 4.19 and in Table 4.6.

Det	Inelastic Dilution factor	Error
1	0.118	0.022
2	0.145	0.027
3	0.182	0.034
4	0.216	0.040
5	0.203	0.038
6	0.253	0.047
7	0.277	0.051
8	0.272	0.050
9	0.287	0.053
10	0.284	0.052
11	0.304	0.056
12	0.297	0.055
13	0.311	0.057
14	0.378	0.070

TABLE 4.6: *The average inelastic dilution factors and the final absolute errors for the North American detectors.*

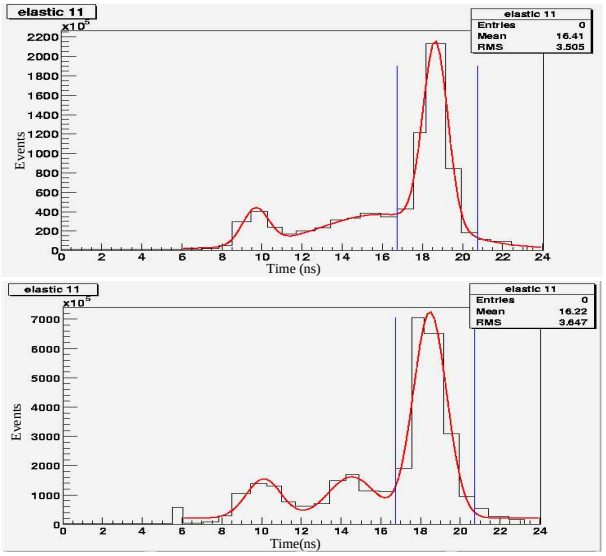

FIG. 4.17: *Both ToF spectra have been corrected using the same white noise run. The top ToF is taken to be a "passing" corrected spectrum. The bottom ToF spectrum is not as smooth as the top ToF spectrum and it "fails" under the assumption that the DNL has changed.*

4.8.3 Inelastic Dilution Factor Results

The North American and French inelastic dilution factors have been extracted (see Tables 4.5 and 4.6) for the 2002-2003 G^0 commissioning run. The errors associated with the inelastic dilution factors allow for the extraction of the elastic asymmetry with an error that is tolerable. The North American errors on the inelastic dilution factors are considerably larger than the French results. This is presumably, in part, due to the width of the elastic cut window which is affected by the DNL.

The DNL that plagued the North American ToF spectra should be reduced in the second G^0 commissioning run with the replacement of the RF translator board. White noise runs will be taken on a frequent basis ($\sim$ 1/day) until the DNL is under control and understood.

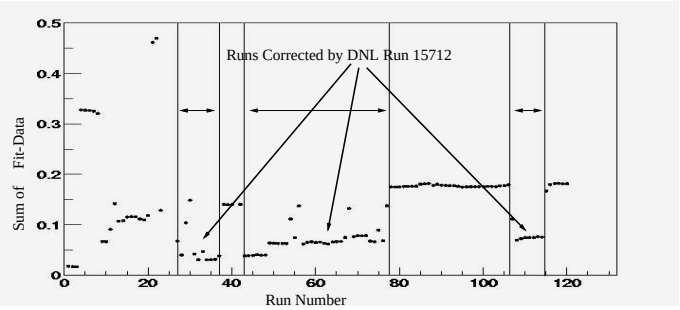

FIG. 4.18: *In deciding which runs are fixed by which white noise spectra, looking by eye at the DNL corrected ToFs in conjunction with looking for minimums of the sum of the fit-data was used. This quantitative method, though useful, was not definitive. Notice fluctuations between runs 43 and 78 might be considered failing but when examined by eye these ToFs appeared corrected.*

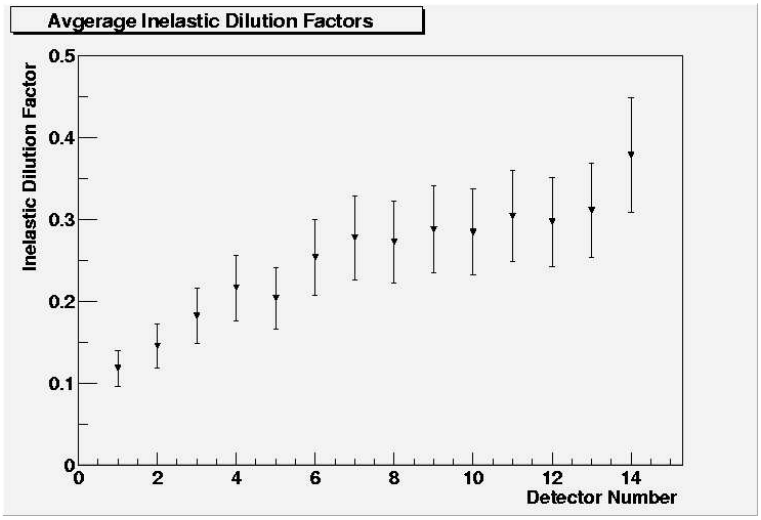

FIG. 4.19: *North American inelastic dilution factors as a function of detector number, averaged over the North American octants.*

4.9 Background Inelastic Asymmetry

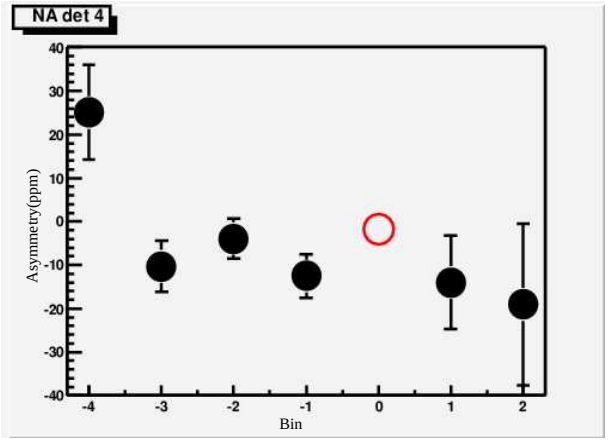

FIG. 4.20: *Example of the coarser asymmetry binning to find the background inelastic asymmetry for North American detector 4. The Time-of-flight asymmetries have been broken down into 7 bins. The elastic proton bin is denoted in red. The asymmetry bins above and below the elastic proton bin were interpolated to find the background inelastic asymmetry under the elastic proton peak.*

In order to extract the physics asymmetry, the background inelastic asymmetry must be known, since inelastic events overlap with the elastic peaks and dilute the elastic asymmetry. This is calculated as

$$A_{el} = (1 + d)A_{corr} - dA_{inel} \tag{4.34}$$

where A_{el} is the elastic asymmetry, A_{corr} is the corrected measured asymmetry from false asymmetries due to helicity-correlated beam properties, A_{inel} is the inelastic asymmetry, and d is the inelastic dilution factor. The main contribution to the background comes from processes involved in scattering from the downstream aluminum window of the target. This background represents 13-25% of the events within the elastic cut window. The background fraction rises with higher detector number (and thus momentum transfer, Q^2). This background has a sizable asymmetry associated with it, on the order of 10 ppm. This background is thought to be due mainly to photo-disintegration of quasi-deuterons in the aluminum windows of the target.

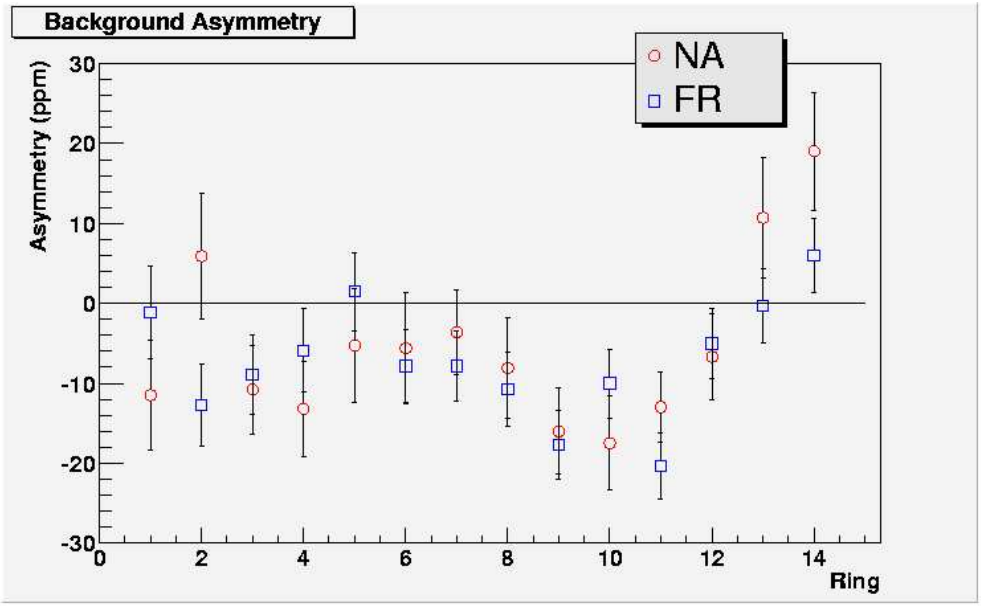

FIG. 4.21: *North American and French extracted background asymmetries. These asymmetries were obtained by dividing the ToF asymmetries into 7 bins and interpolating the bin above and below the elastic cut window.*

With only Time-of-Flight histograms, the background inelastic asymmetry was extracted by dividing the Time-of-Flight spectra into 7 bins with the 5th bin being the elastic proton cut (see Figure 4.20). A linear interpolation was made between the side band bins below and above the elastic proton bin. The results can be seen in Figure 4.21 and Table 4.7.

In the next commissioning run, the downstream window thickness will be reduced from 11 mils to 3 mils, which should reduce the background by nearly 60%. The background asymmetries and yields will be directly measured during the next run with dedicated dummy target runs with a 30 mil aluminum foil dummy target (known as the "flyswatter") and a 3.4 mil tungsten radiator. The purpose of the flyswatter and radiator will be to confirm the expected fraction of events from the downstream window and to be able to quickly collect asymmetry data on aluminum to the level of a few ppm in a short amount of time.

Det	NA A_{inel} (ppm)	FR A_{inel} (ppm)
1	-11.5 ± 6.9	-1.1 ± 5.8
2	5.9 ± 7.8	-12.7 ± 5.1
3	-10.8 ± 5.6	-8.9 ± 4.9
4	-13.2 ± 6.0	-5.9 ± 5.2
5	-5.3 ± 7.1	1.5 ± 4.9
6	-5.6 ± 6.9	-7.8 ± 4.6
7	-3.6 ± 5.3	-7.8 ± 4.4
8	-8.1 ± 6.3	-10.7 ± 4.6
9	-16.0 ± 5.4	-17.7 ± 4.3
10	-17.5 ± 5.9	-10.0 ± 4.3
11	-13.0 ± 4.4	-20.3 ± 4.1
12	-6.7 ± 5.4	-5.0 ± 4.4
13	10.7 ± 7.5	-0.3 ± 4.6
14	19.0 ± 7.4	6.0 ± 4.6

TABLE 4.7: *The extrapolated background inelastic asymmetries for North American and French detectors. These asymmetries were interpolated from averaging the N bins above and N bins below the elastic cut window. These results are reported by detector number, where the results for a detector number were averaged over the 4 detectors from the NA (Fr) Octants, e.g. results reported for Fr A_{inel} Det 1 are the weighted average of detectors 1 from French Octants 2,4,6,and 8.*

4.10 Polarimetry

The Moller polarimeter described in Section 3.8 was used to correct the physics asymmetry for each detector

$$A_{phy} = \frac{A_{el}}{P_b} \tag{4.35}$$

where P_b is the beam polarization.

A limited number of measurements were made during the month of data taking as can be seen in Figure 4.22. The average beam polarization was found to be (77.3 ± 0.4)%.

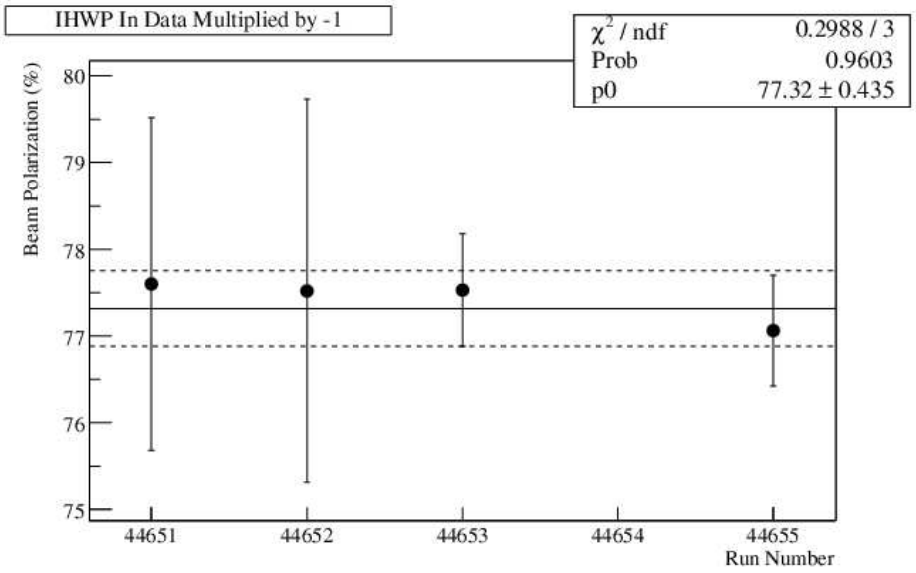

FIG. 4.22: *Polarization measurements made during the engineering run. Polarization measurements made with the insertable halfwave plate 'in' must be multiplied by -1 to compare to the insertable halfwave plate 'out' measurements.*

4.11 Radiative Corrections

Since the statistical error bars of this work are so large, the data have not been corrected for electromagnetic radiative effects. This is because the radiative effects are expected to be small, on the order a few percent of the measured asymmetry. In order to carry out a complete analysis, radiative corrections should be taken into account. In order to do this the following references are invaluable [63, 64].

There are two types of radiative corrections: External Bremsstrahlung corrections and internal Bremsstrahlung corrections. External corrections are when the beam electrons lose energy by bremsstrahlung from the target aluminum entrance window or in the hydrogen itself before scattering off of a second proton and into the detector. Internal corrections are when a beam electron interacts by more than one photon with the proton. These internal corrections are further divided into "real" and "virtual" processes. In real processes the photon is a real photon that

is emitted during the scattering. In virtual processes, during the scattering virtual photons are emitted and re-absorbed in the scattering process.

These higher-order interactions have two effects on the measured parity violating asymmetry

- The electron energy is reduced leading to a lower value of Q^2 and asymmetry for a given scattering angle.
- The spin of the electron can be flipped, yielding a net depolarization.

These effects will reduce the measured asymmetry with respect to the tree level asymmetry. Emission of the photons after the parity-violating interaction will reduce the energy of the scattered proton leading to a reduction in the detector signal. The effect of the internal and external bremsstrahlung is to remove protons from the elastic peak and put them into a long tail.

In order to calculate the radiative correction, R_c, it is necessary to calculate two different parity-violating asymmetries: A_t, the tree level asymmetry from single boson exchange and A_R, the asymmetry including electromagnetic radiative effects. The radiative correction is the ratio of the two asymmetries:

$$R_c = \frac{A_t(Q^2)}{A_R(Q^2)}. \tag{4.36}$$

4.12 Q^2 Determination

Knowing the elastic electromagnetic form factors from other experiments allows for the extraction of the strange electric and magnetic form factors. In order to perform this extraction, the Q^2 must be known. The total error on the extracted strange form factors should be smaller than 10%; this requires that Q^2 be known to the 1% level. In order to reach this precision, one should know the absolute ToF with an accuracy better than 50 ps.

The average momentum transfer, $< Q^2 >$, was determined by comparing the detector ToF at different magnetic fields with a Monte Carlo simulation [65]. As the magnetic field is varied, the pion peak will remain stationary while the proton trajectory will shift and may even reach another detector system.

As mentioned above, this study relied on the results from simulation (G0GEANT, G0TRACE, and GRAAL). The simulation takes into account the electronics, the effects of the spectrometer magnetic field and the detector positions. These results allow one to determine the value of all these parameters directly from the measured ToF. Using these values allows one to find the $< Q^2 >$ for each detector.

When the magnetic field varies, the particle trajectories are modified; they might even reach another detector. The elastic proton peak is modified by different field strengths though the pion peak remains unchanged. The idea is to study the magnetic field variation using the relative position between the pion and elastic proton peak. From simulation one can see how the ToF should change with magnetic field and then compare this to measurements.

With the French electronics, the proton peak may be determined within a few ps (since the French electronics has 250 ps bins). Unfortunately, in the case of the North American electronics, it is not possible to know the peak positions to better than 60 ps for the Time Encoding Electronics; this was further complicated by the North American DNL.

In conclusion, the simulation correctly reproduces the experimental data. The $< Q^2 >$ were found (see Table 4.8) with a 1% precision.

Det	$< Q^2 >$ (GeV/c)^2
1	0.12
2	0.13
3	0.14
4	0.14
5	0.15
6	0.16
7	0.18
8	0.19
9	0.21
10	0.23
11	0.26
12	0.30
13	0.34
14	0.40

TABLE 4.8: $< Q^2 >$ *values determined by comparing Time-of-Flight differences between pions and the elastic protons at various magnetic fields. Only data from the French detectors were used to determine* $< Q^2 >$ *due to the fine time binning of the French electronics (0.25 ns).*

CHAPTER 5

Conclusions

Parity-violating electroweak asymmetries have been measured in elastic scattering of polarized electrons from the proton at forward angles. The asymmetries are compared to the Standard Model assuming no strange quark contribution. Various models for predicting strange quark contributions to the proton are discussed for completeness. Future experiments using parity violation are described.

5.1 Discussion of Engineering Run

The first G^0 engineering run (from October 2002 through January 2003) was very successful. Each sub-system of the apparatus was commissioned.

Many of the challenges associated with generating and maintaining the unique beam properties were met during the first engineering run. The time structure for the electron beam was 32 ns which differs from CEBAF's typical beam structure of 2 ns. This produces a higher bunch charge, due to having 16 times as many electrons in one bunch, which in turn produces space-charge effects that complicate beam transport through the injector. Most of the critical beam properties were delivered in January 2003:

- beam current of 40 μA,
- beam fluctuations in position Δ x, Δ y < 20 μm, beam fluctuations in intensity Δ I/I < 2000 ppm.

Feedback systems used to minimize the helicity-correlated beam properties were tested. The charge feedback system worked but the position feedback system requires some investigation into its unstable behavior (the calibration slopes for the PZT mirror seemed to change very quickly over a 3 hour period). The false asymmetries due to helicity-correlated beam properties were small and kept under control.

The G^0 detectors performed well. The high voltages for the PMTs were set at values that allowed for high detection efficiency and the PMTs were able to stand rates at the nominal beam current of 40 μA. The gains were matched and their stability was monitored and deemed satisfactory over time and for different beam currents. The discriminator's thresholds were adjusted to eliminate noise and low-energy background while not rejecting the elastic proton signals. Typical detector rates were on the order of 1-2 MHz with a typical dead time of 10%. This induces a false asymmetry when coupled to a non-zero charge asymmetry with an uncorrected effect of $\sim 15\%$; after correction $\sim 1\%$. The G^0 detectors observed yield sensitivities to six beam properties: helicity-correlated x and y beam motion, x and y beam angle, the energy and beam charge.

There was higher background in Hall C than what was expected. This problem had to be taken care of early on since the projected anode currents of the PMTs in the higher numbered (larger Q^2) detectors would have been too high at the nominal current of 40 μA with the nominal gain settings. This higher background was due to neutrals coming from the downstream beam pipe. This was taken care of by adding a 4 inch thick lead box around the beam pipe.

The G^0 magnet ran at full design current at 5000A for the first time on Decem-

ber 18, 2002 and then throughout the January 2003 running.

The G^0 target was well behaved with density fluctuations at 40 μA being negligible. Various target density studies were carried out to extract the contribution from the target windows.

The background yields and asymmetries are needed to correct for the elastic asymmetries. The inelastic yield under the elastic cut due to inelastic protons was found to be about 13-25% of the signal. In order to cut down on the background signal, in the forward angle run the downstream window thickness will be reduced and an insertable dummy target will be added to help quantify the background.

5.2 Measured Physics Asymmetry

The physics asymmetry is given by

$$A_{phy} = \frac{1}{P_e}((1+d)A_{meas} - dA_{inel}). \tag{5.1}$$

Table 5.1 contains a list of the electroweak parity-violating asymmetries measured by the first G^0 engineering run.

The errors are determined by Equation 4.8 along with considering the error on the polarization. Explicitly writing these out: the contribution to the error from the measured asymmetry is given by

$$\sigma^2_{A_{meas}} = \left(\frac{1}{P_e}\right)^2 (1+d)^2 \Delta A^2_{meas}, \tag{5.2}$$

the contribution to the error from dilution factor is given by

$$\sigma^2_d = \left(\frac{1}{P_e}\right)^2 (A_{meas} - A_{inel})^2 \Delta d^2, \tag{5.3}$$

the contribution to the error from the background inelastic asymmetry is given by

$$\sigma^2_{A_{inel}} = \left(\frac{1}{P_e}\right)^2 d^2 \Delta A^2_{inel}, \tag{5.4}$$

and the error from the polarization is given by

$$\sigma^2_{P_e} = \left(\frac{1}{P_e}\right)^2 A^2_{el} \Delta P^2_e. \tag{5.5}$$

Table 5.2 contains a list of different error contributions to the physics asymmetry.

Det	Q^2 (GeV/c)^2	NA A_{phys} (ppm)	Fr A_{phys} (ppm)
1	0.122	-3.8 ± 2.5 ± 1.6	-4.9 ± 2.0 ± 1.6
2	0.128	-4.5 ± 3.2 ± 2.1	-3.9 ± 1.9 ± 1.5
3	0.135	-2.6 ± 2.5 ± 1.9	-3.8 ± 1.9 ± 1.5
4	0.143	-1.2 ± 2.7 ± 2.3	-6.6 ± 2.0 ± 1.5
5	0.152	-8.0 ± 3.4 ± 2.5	-4.1 ± 2.0 ± 1.7
6	0.163	-2.5 ± 3.5 ± 3.0	-2.0 ± 2.0 ± 1.6
7	0.177	-9.1 ± 2.8 ± 2.5	-7.3 ± 2.0 ± 1.7
8	0.192	-3.4 ± 3.5 ± 3.0	-6.7 ± 2.1 ± 1.6
9	0.209	-3.8 ± 3.0 ± 2.8	-6.6 ± 2.1 ± 1.6
10	0.231	-8.7 ± 3.5 ± 2.9	-11.3 ± 2.2 ± 1.7
11	0.260	-5.8 ± 2.8 ± 2.3	-5.6 ± 2.3 ± 1.9
12	0.298	-10.9 ± 3.4 ± 2.7	-9.1 ± 2.5 ± 2.0
13	0.341	-14.0 ± 5.2 ± 4.2	-10.3 ± 2.9 ± 2.4
14	0.404	-6.1 ± 5.8 ± 4.8	-10.3 ± 3.2 ± 3.0

TABLE 5.1: *Extracted North American and French physics asymmetries. The first(second) error is the statistical(statistical error on systematic effects) error. These results are reported by detector number, where the results for a detector number were averaged over the 4 detectors in a ring from the NA (Fr) Octants, e.g. results reported for Fr A_{phys} Det 1 are the weighted average of detectors 1 from French Octants 2,4,6,and 8.*

The data shows good agreement with the expected statistical properties. The parity-violating asymmetries behave as expected. The asymmetries have the correct sign and change sign under the influence of the insertable halfwave plate. The results are consistent between the North American and French sets of detectors/electronics. It is important to keep in mind when looking at the results of this work that the amount of data taken during the first engineering run represents only $\sim \frac{1}{16}$ of the expected final statistics from the final forward production run. The statistical error bars should be about 4 times smaller for the forward production run asymmetries.

Detectors 15 and 16 are not included in this analysis. Detector 15 contains two Q^2 points ($0.45 < Q^2 < 0.9$ (GeV/c)^2) in the elastic TOF spectrum. This

complicates extracting the inelastic background. Decector 16 contains no elastic protons in the TOF spectrum. This detector is used as a background detector. For these reasons, detectors 15 and 16 are missing from the extracted asymmetry results.

Det	NA σ_d^2 (ppm)^2	Fr σ_d^2 (ppm)^2	NA $\sigma_{A\_meas}^2$ (ppm)^2	Fr $\sigma_{A\_meas}^2$ (ppm)^2	NA $\sigma_{A\_inel}^2$ (ppm)^2	Fr $\sigma_{A\_inel}^2$ (ppm)^2	NA $\sigma_{P_e}^2$ (ppm)^2	Fr $\sigma_{P_e}^2$ (ppm)^2
1	0.04	0.00	6.21	4.17	2.06	2.13	0.00	0.00
2	0.05	0.00	10.16	3.55	3.86	2.02	0.00	0.00
3	0.09	0.00	6.064	3.60	3.17	2.06	0.00	0.00
4	0.24	0.00	7.29	3.94	4.83	2.00	0.00	0.00
5	0.00	0.00	11.47	3.97	5.94	2.48	0.00	0.00
6	0.03	0.00	12.19	3.95	8.57	2.35	0.00	0.00
7	0.00	0.00	7.79	3.95	6.03	2.48	0.00	0.00
8	0.11	0.00	12.31	4.55	8.22	2.25	0.00	0.00
9	0.41	0.01	9.15	4.37	7.29	2.22	0.00	0.00
10	0.14	0.00	12.56	4.73	7.89	2.51	0.00	0.00
11	0.12	0.02	7.80	5.06	5.05	3.13	0.00	0.00
12	0.04	0.00	11.84	6.37	6.96	3.80	0.00	0.00
13	2.15	0.01	27.51	8.17	14.86	5.44	0.00	0.00
14	2.07	0.04	3.72	10.04	20.55	8.87	0.00	0.00

TABLE 5.2: *Individual contributions to the errors given by Equations 5.2 through 5.5. A_{meas} contains corrections due to helicity-correlated beam properties and dead time.*

This can be compared to the Standard Model strangeness-independent asymmetry, $A_{th} = \eta + \psi G_A^e$, taken from Equations 2.46 through 2.51, which is written again here for convenience

$$A_{th} = -\frac{G_F Q^2}{4\pi\alpha\sqrt{2}}\left[(1-4\sin^2\theta_W) - \frac{\epsilon G_E^{\gamma,p} G_E^{\gamma,n} + \tau G_M^{\gamma,p} G_M^{\gamma,n} + 2(1-4\sin^2\theta_W)\epsilon' G_M^{\gamma,p} G_A^e}{\epsilon (G_E^{\gamma,p})^2 + \tau (G_M^{\gamma,p})^2}\right].$$

Deviations from A_{Th} would imply the presence of strangeness in the proton. The standard model strangeness-independent asymmetry in Figure 5.1 was calculated using the dipole parameterization of the proton's electric (with an uncertainty of 2%) and magnetic form factors (with an uncertainty of 2%) , the dipole parameterization

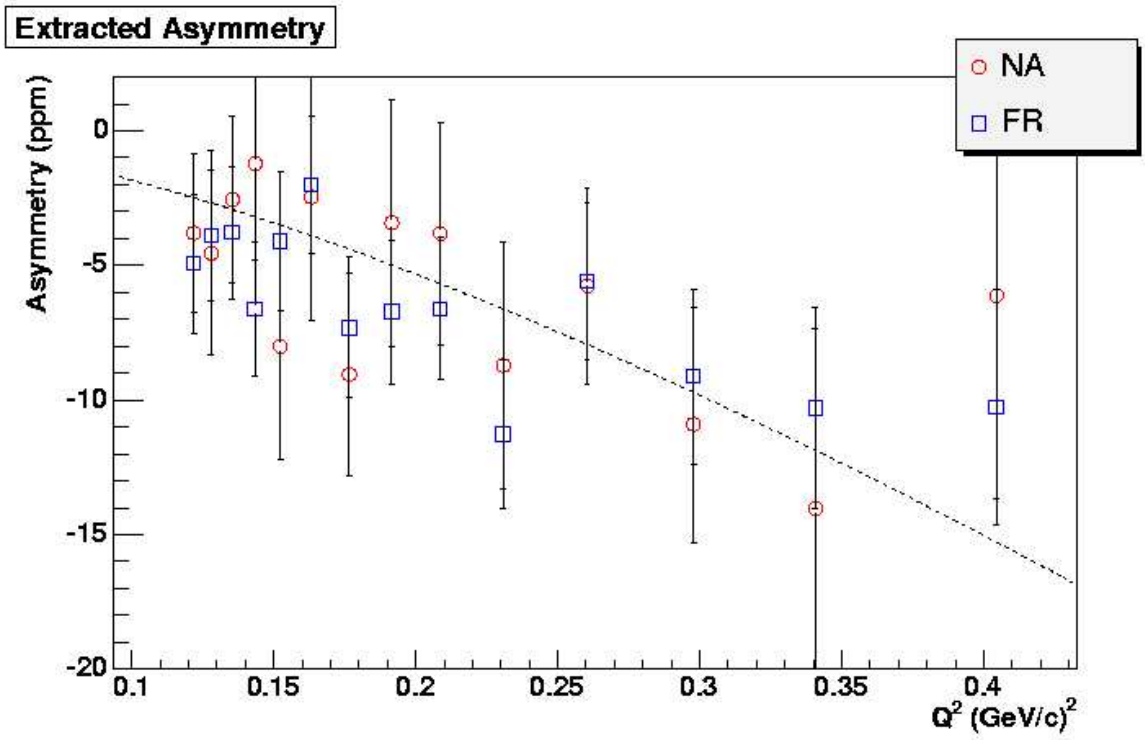

FIG. 5.1: *Plot of the extracted North American and French asymmetries vs. momentum transfer. The errors are statistical and systematic errors added in quadrature. The dashed line represents the Standard Model calculation of the parity-violating asymmetry assuming no contributions from the strange quarks.*

of the neutron's magnetic form factor (with an uncertainty of 3%) and the Galster parameterization of the neutron's electric form factor (with an uncertainty of 20%).

5.3 Theoretical Predictions

A proper description of the strange form factors should be based on QCD. The problem is that the mass of the strange quark, $m_s \approx 150$ MeV is comparable to the QCD scale factor λ_{QCD}, thus not easily allowing for a small expansion parameter as used for the heavier quark calculations. This forces the theorist into the territory of models and chiral perturbation theory. Several review articles on this subject can be

found in the literature [66–68]. Even the applicability of chiral perturbation theory is called into question here since the strange quark mass may not be light enough to make the SU(3) chiral perturbation valid since $\frac{m_K}{\lambda_\chi} \sim \frac{1}{2}$ which is not particularly small. Even if the SU(3) chiral expansion is well behaved, there appears to be various counter terms (low energy constants) that have not been measured in experiment and must be extracted from various models. Typically the form factors associated with $\bar{s}\gamma_\mu s$ are characterized by the strange magnetic moment μ_s,

$$\mu_s \equiv G_M^s(Q^2 = 0) \tag{5.6}$$

and by the strangeness radius, r_s^2,

$$r_s^2 \equiv -6 \left[\frac{dG_E^s}{dQ^2}\right]_{Q^2=0}. \tag{5.7}$$

Loop Models

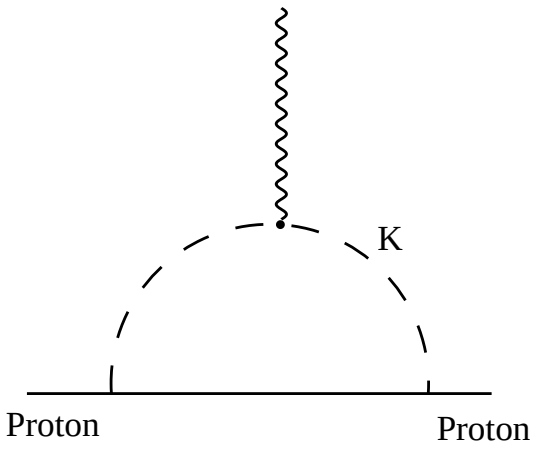

FIG. 5.2: *Kaon loop diagram.*

A set of models known as "loop models" describes the strangeness content of the nucleon in terms of pairs of $K\Lambda$,$K\Sigma$, or ηN components. The nucleon fluctuates into a $q\bar{q}$ pair to form a meson and an intermediate baryon state. The meson and baryon later recombine as the $q\bar{q}$ pair annihilates and the original nucleon is

left in the ground state. Only diagrams involving kaons and strange baryon states contribute to yield non-zero strangeness. Koepf [69] first evaluated μ_s and r_s^2 but did not include the so-called "seagull" diagrams. These diagrams are needed to satisfy the Ward-Takahashi identity. These were later added by M. Burkhardt et al. [70]. The predictions of r_s^2 in the kaon loop calculation tends to be smaller than the pole-fit analysis. To reconcile this difference, the kaon loop model was merged with VMD and $\omega - \phi$ mixing.

Lattice QCD

Lattice QCD computations can provide a means of obtaining values for the low energy constants that have not been measured. These calculations are typically carried out in the "quenched" approximation where the $s\bar{s}$ pairs appear only via operator insertion. To achieve a firm lattice QCD prediction requires resolving several issues. One is to perform an unquenched calculation. Another issue is that one would like to have light quark masses that one can extrapolate to physical values using chiral perturbation theory.

Dispersion Relations (Pole-Fit Analysis)

This is a first-principles approach to calculating G_E^s and G_M^s. This analysis involves various inputs such as form factors and experimental scattering amplitudes. The nucleon strangeness arises from the nucleus coupling to a strange meson. In this case, the exchanged vector boson (Z^0 or γ) fluctuates into an isoscaler meson (ω or ϕ) which interacts with the nucleon. The ω and ϕ are linear combinations of strangeness and non-strangeness components.

Jaffe [71] was the first to make theoretical predictions of μ_s and r_s^2. Jaffe based his analysis on the work of Hohler [72]. Hammer et al. [73] updated this analysis using a new dispersion-theoretic analysis of the nucleon electromagnetic form factors.

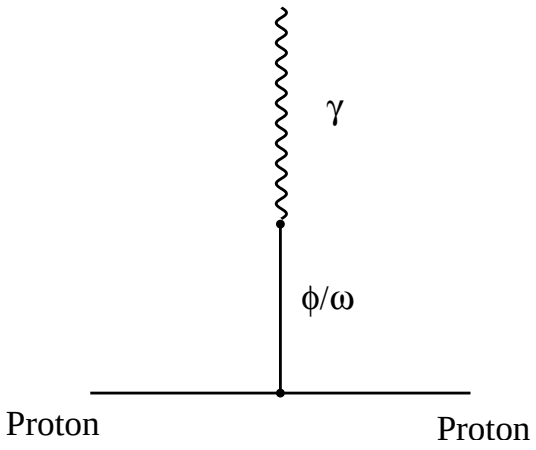

FIG. 5.3: *Pole loop diagram.*

A noticeable point with these analyses is that they typically yield a different sign of the strange electric radius compared to most other models.

5.4 Future Parity-Violation Experiments

HAPPEX-II and HAPPEX-He

The HAPPEX II [84] experiment at Jefferson Lab, in Hall A, proposes to constrain the nucleon strangeness radius of the proton:

$$\rho_s + \mu_p \mu_s$$

where ρ_s is the strangeness radius defined as $\rho_s = \frac{G_E^s}{d\tau}$, μ_p is the proton magnetic moment and μ_s is the strange magnetic moment. This will be done by measuring parity-violating asymmetries in elastic scattering of 3.2 GeV polarized electrons from an unpolarized hydrogen target. The measurement is made at a forward scattering angle ($\theta = 6^\circ$) corresponding to a Q^2 of 0.11 (GeV/c)^2 (see Figure 5.4). The expected physics asymmetry will be about 1.7 ppm. This measurement is complementary to the SAMPLE [13] measurement at MIT Bates at the same Q^2 but

Model	Author	$\mu_s(n.m.)$	$r_s^2(fm^2)$
Pole	Jaffe [71]	-0.31±0.09	0.11 - 0.22
Pole	Hammer [73]	-0.24±0.03	0.19±0.03
Pole	Meissner [74]	0.003	0.002
Pole	Forkel [75]	-0185±0.075	0.14±0.06
Loop	Burkhardt [70]	-0.355±0.045	-0.0297±0.0026
Loop	Geiger [76]	0.035	-0.04
Loop	Koepf [69]	-0.026	-0.01
Loop+VMD	Cohen [77]	-0.28±0.04	-0.0425±0.0026
Skyrme	Park [78]	-0.13	-0.11
Skyrme	Park [78]	-0.33	-0.19
Lattice QCD	Dong [79]	-0.36 ±0.20	-0.16±0.06
HBχPT	Hemmert [80]	0.18±0.34	0.05±0.09
NJL Soliton	Abada [81]	0.10 ±0.15	-0.15±0.05
χSM	Goeke [82]	0.115	-0.095
PχQM	Gutsche [83]	-0.048±0.012	-0.011±0.003

TABLE 5.3: *Some predicted values of strangeness radius r_s^2 and strange magnetic moment μ_s.*

different kinematics. At the same kinematics, there is another proposed experiment in the HAPPEX family: the HAPPEX-He [85] experiment will measure the parity-violating asymmetries of polarized electrons scattering from ^{4}He nuclei. Scattering from ^{4}He will be sensitive only to G_E^s and not G_M^s or G_A^e due to the fact that ^{4}He is a 0^{++} nucleus. With the ^{4}He measurement of $G_E^s(Q^2 \to 0) = \rho_s$ and the HAPPEX-II proton measurement, HAPPEX will be able to separately extract both ρ_s and μ_s.

PVA4

The PVA4 experiment [51], besides making forward angle measurements as described in Section 2.7, will be performing backward angle measurements. The detector system will be reversed relative to the target to measure back-scattered electrons between $140^\circ < \theta_e < 150^\circ$. These measurements will be made at two values of $Q^2 = 0.23$ (see Figure 5.4) and 0.48 (GeV/c)^2 in order to complement the forward angle PVA4 and HAPPEX measurements.

G^0 Forward Angle

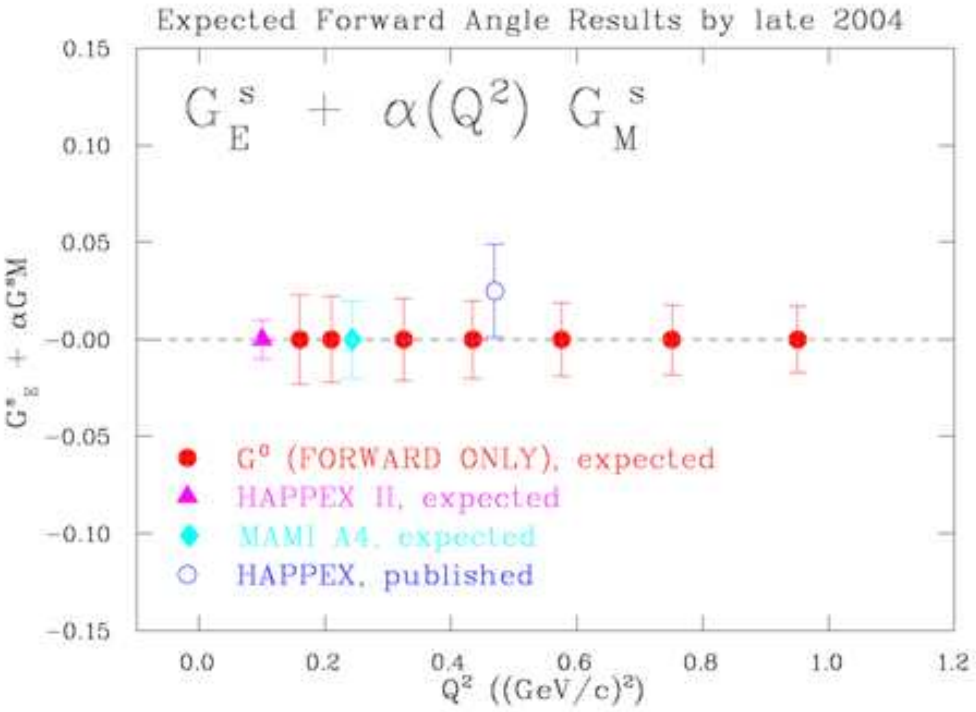

FIG. 5.4: Expected forward angle results from the G^0, HAPPEX II [84], and A4 [51] along with result from the HAPPEX [14] experiment. A linear combination of the strange and electric form factors are accessible from forward angles. This linear combination is of the form of $G_E^s + \alpha(Q^2)G_M^s$ where $\alpha(Q^2)$ is dependent on kinematic factors.

In the winter of 2004, G^0 will make forward angle measurements of electroweak asymmetries on polarized electrons scattering from unpolarized hydrogen. These measurements will be made over a momentum transfer of 0.1-1.0 $(\mathrm{GeV/c})^2$ (see Figure 5.4). This will allow for an extraction of the vector neutral weak form factors. Combining the neutral weak form factors with the known electromagnetic form factors allows for an extraction of the linear combination of strange electric, $G_E^s(Q^2)$, and strange magnetic, $G_M^s(Q^2)$, form factors over this momentum transfer range.

G^0 Backward Angle

Beginning in 2006, G^0 will begin the backward angle measurement phase of the experiment. Electroweak asymmetries will be measured in backward-scattered electrons from polarized electron scattering from hydrogen and deuterium targets. This asymmetry allows for an extraction of a linear combination of strange magnetic, $G_M^s(Q^2)$, and the electron-nucleon axial, $G_A^e(Q^2)$, form factors. Three sets of measurements will be made in order to obtain these asymmetries at three different momentum transfers: 0.3, 0.5, and 0.8 $(\mathrm{GeV/c})^2$. Combining these linear combination of $G_A^e(Q^2)$ and $G_M^s(Q^2)$ with the G^0 forward angle measurements, which extract a linear combination of $G_E^s(Q^2)$ and $G_M^s(Q^2)$, will allow a separation of the strange electric, strange magnetic, and axial form factors as a function of Q^2.

APPENDIX A

G^0 Abbreviation & Acronym Glossary (GAAG)

A_{corr}: The measured elastic asymmetry that has been corrected for helicity correlated false asymmetries due to beam properties.

A_{el}: The measured asymmetry.for elastic events.

A_{inel}: The asymmetry for inelastic protons that must be removed from the corrected measured asymmetry.

A_{meas}: The experimentally measured raw elastic and inelastic proton electroweak asymmetry.

A_{phy}: The final fully corrected measured elastic electroweak asymmetry.

A_{th}: Tree-level Standard Model prediction of the electroweak asymmetry.

BCM: The Beam Current Monitor (BCM) is a cylindrical cavity whose resonant frequency is adjusted to 1497 MHz (the frequency of the typical CEBAF beam). Inside the cavity is a loop antenna located where the electric field is minimum and the magnetic field is at a maximum. The antenna is coupled to one of the resonant modes of the cavity and the output signal is proportional to the beam current.

BPM: The Beam Position Monitor (BPM) consists of four metal strips surrounding the beamline. When the electron bunches pass through the BPM, a signal is produced by induction. The output signals from the four strip lines are then combined to yield beam position information.

CFD: The Constant Fraction Discriminator (CFD) are designed to produce accurate timing information from analog signals of varying heights but with the same rise time. This will reduce the "walk" of the output signal.

χPT: χPT is a short-hand notation for Chiral Perturbation Theory.

DMCH-16X: The DMCH-16X (Discriminator, Mean-Timers, time digital Converter, Histogramming, 16 channels, and X is for VXI standard) is the French electronics.

DNL: The Differential Non-Linearity (DNL) is defined as deviations from the nominal 1 ns wide bin structure of the North American time-of-flight spectra.

FPD: The Focal Plane Detectors (FPD) are 16 iso-Q^2 double layered scintillator detectors located at the focal plane of the spectrometer.

Fr: Fr is a short-hand notation for “French”.

GMS: The Gain Monitoring System (GMS) shines laser light onto the scintillators in order to monitor the gain changes in the photo-multiplier tubes.

IA: The Intensity Attenuator (IA) is a charge feedback device that controls the helicity correlated charge asymmetry.

IHWP: The Insertable Halfwave Plate (IHWP) is used to change the helicity of the polarized light coming from the G^0 laser on the laser table in the injector.

LTD: The Latching Time Digitizers (LTDs) are specialized electronics used to bin detector signals into 1 ns time bins for inputs to the scalers.

MPS: A Macro-pulse (MPS) is one helicity state that lasts for 33 ms (1/30 second).

NA: “NA” is an acronym for North American.

NPN: Next Pulse Neutralization (NPN) is the disabling of the LTDs for the next beam burst (32 ns) after a hit has been recorded from a detector. This allows the mean-timers to clear and allows for an exact calculation of the deadtime.

PMT: “PMT” is an acronym for Photo-Multiplier Tube.

ppm: “ppm” represents parts-per-million.

PZT: "PZT" is an acronym for Lean Zirconate Titante. This device is a mirror attached to a piezo-electric mount that changes the angle of the laser beam before entering the Pockels cell. This is used to minimize helicity correlated position differences.

QRT: A quartet (QRT) is a sequence of 4 macro-pulses from which an asymmetry can be formed. The helicity of the first macro-pulse is chosen pseudo-randomly with the next two macro-pulse helicities the complement of the first macro-pulse. The fourth macro-pulse is the same helicity as the first macro-pulse. This allows for two different quartet patterns (-++-) and (+−+).

RHWP: The Rotatable Halfwave Plate (RHWP) is used to minimize the charge asymmetry by rotating the residual linear component of the slightly elliptical light emerging from the helicity Pockels cell..

SMS: The Superconducting Magnet System (SMS) is the 1.6 T·m magnet used in the G^0 experiment.

ToF: The Time-of-Flight (ToF) is amount of time it takes for a particle to reach the detectors from the G^0 target.

APPENDIX B

Detector Testing and Calibration

B.1 Output signals of the North American Focal Plane Detectors

During the G^0 experiment, a particle is detected if the signals it produces in each of the four photo-multiplier tubes (PMT) attached to the light pipe pair are above a certain discriminator threshold. The amplitude of the signal produced by each PMT can be approximated by the following expression :

$$Amplitude = N_{\gamma e} \times gain(HV) \times A_{cable} \tag{B.1}$$

where :

- $N_{\gamma e}$ is the number of photo-electrons[1] produced at the photo-cathode of the PMT,

- $gain(HV)$ is the gain[2] which increases as the HV applied to the PMT increases,

[1] A photo-electron is an electron produced by photo-electric effect when a (scintillation) photon hits the PMT photo-cathode.

[2] The gain of a PMT is the factor of amplification of the photo-electrons through the dynodes chain of the PMT.

- A_{cable} is the attenuation of the signal through the cables between the PMT output and the discriminator input.

In order to produce a signal of large enough amplitude to pass the discriminator threshold, one may consider increasing the gain. This option seems the most efficient although its long term effect in a radiation harsh environment should be considered. A large gain could produce a large anode current and as a consequence an early aging of the PMT.

Another method is to increase the amplitude of the signal by maxiimizing the number of photo-electrons. It has been determined that for the G^0 experiment a minimum number of 40 photo-electrons must be produced by particles hitting the scintillators [86]. The determination of this minimum output is described in the following section.

B.1.1 Light Pipe Characteristics

A light pipe is characterized the number of photo-electrons, $N_{\gamma e}$, produced by the PMT attached to it. This quantity is the following product:

$$N_{\gamma e} = \Delta E \times C \times PMT_{QE} \times PMT_{contact} \times A_{scint} \times A_{global} \tag{B.2}$$

where :

- ΔE is the energy lost by the particle passing through the scintillator, and C is the conversion factor between energy lost and photon produced. Those quantities are characteristic of the scintillator type and the energy of the detected particle, and are not in the scope of this report.

- PMT_{QE} is the quantum efficiency of the PMT photo-cathode, and $PMT_{contact}$ is the fraction of photons exiting the light guide end that actually hit the PMT

photo-cathode.

- A_{scint} is the attenuation of photons along the scintillator from the hit position to the glue joint between the scintillator and the light guide. A_{global} is the attenuation of the photons going through the glue joint between the scintillator and the light guide and the bulk attenuation along the light guide.

Measurements of the number of photo-electrons extracted from the G^0 NA FPD have been performed during the assembly of the detectors; they took place at JLab in the so-called Clean Room. They are described in the following section. For clarity, it has been decided to separate the characterization of the light pipe and the characteristic of the PMT. Therefore, the following results are given for an arbitrary but constant value of PMT_{QE} and $PMT_{contact}$ as described later. A_{scint} and A_{global} can vary from one light pipe to the other as they are a function of the quality of the scintillator surface and the length of the scintillator (A_{scint}), or the global quality of the light guide and the gluing between the scintillator and the light guide (A_{global}).

Setup and Calibrations

As soon as the light pipe have been mounted on one octant, the ends of the light pipe were equipped with PMTs and the assembly was rolled into a dark space. The signals were produced either by a radioactive source placed on the scintillator, a LED illuminating the faces of the PMTs, or cosmic rays. The systematic calibrations performed in order to estimate the number of photo-electrons produced by the light pipes were :

1. The photo-electron calibration :

   The signal produced by a particle passing through the scintillator is measured as a charge in an ADC channel. In order to determine the number of photo-electrons produced, it is necessary to know the charge produced by a single photon hitting

the PMT photo-cathode. The calibration was performed by shining a LED in front of the PMT face. The brightness of the LED was reduced by lowering the voltage applied to the LED down to a point were only one photon at a time was detected by the PMT. The ADC signal measured in that case was very small and usually overlapped with the pedestal of the ADC. Two independent methods were used to amplify the single photo-electron signal. In one hand the signal was amplified using a calibrated analog amplifier. The precision of this determination is $\sim 10\%$. In the other hand, the single photo-electron peak was measured with a large HV applied to the PMT, the calibration was then extrapolated to "regular" HV using a calibrated gain-HV curve. The precision of this calibration is also $\sim$ 10% due to the extrapolation. The two methods agree within error bars. For the tests performed in the Clean Room, only eight PMTs were used. Each PMT was mounted in the same position and tested. A photo-electron calibration was performed for each of those PMT before almost all measurements using the analog amplifier method. The gain of each tube was found to be constant in the 10% error bar during the course of the measurements (almost a year). The results in term of photo-electrons presented later are computed with the daily calibrations, therefore their precision is 10%.

2. The determination of PMT_{QE} and $PMT_{contact}$:

   The number of photo-electrons detected at the end of the light pipe depends on the quality of the PMT used for detection because of the quantum efficiency (PMT_{QE}) of the cathode. It also depends on the quality of the contact ($PMT_{contact}$) between the tube and the light-guide. The reproducibility of $PMT_{contact}$ was measured in the following way. The radioactive source was placed on a scintillator, and was not moved during the whole course of the test. The signal produced by the source was measured in an ADC channel. The contact

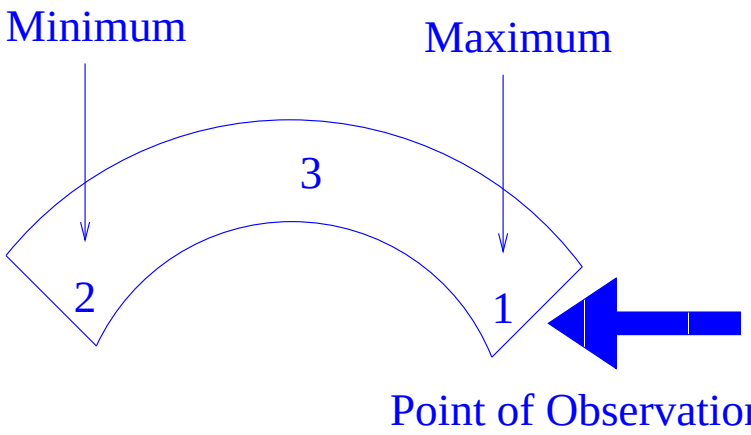

FIG. B.1: *Positions of interest along the G^0 scintillator. A signal produced in position 2 will undergo a maximum attenuation in its travel to the point of observation. Position 3 is the geometrical middle of the scintillator, a signal produced at this position therefore undergo an average attenuation to the point of observation. Signals produced in position 1 undergo a minimal attenuation into the scintillator before being detected.*

between the PMT face and the light pipe was broken by removing the PMT from its housing. The silicon cookie was unstuck from the face of the PMT. The PMT and the cookie were then put back in the housing therefore creating a new contact between the PMT face and the light pipe. The signal of the radioactive source was re-measured. The process was repeated ten times and the ADC value was found to be consistent within 5%. The measurement of the relative tube quantum efficiencies (PMT_{QE}) was performed using the same protocol. Again, the radioactive source stays fixed. The output signal is measured in terms of photo-electrons for different tubes inserted in the housing. It was found that the number of photo-electrons produced by four different tubes used during this testing differed by 15%. In the following, the different relative quantum efficiencies are corrected to normalize the signal measured with different tubes between themselves. Nevertheless, one should consider this uncertainty when quoting the number of photo-electrons produced at the end of the light pipes.

Measurements

To determine if the G^0 particle going through the scintillator will produce at least 40 photo-electrons, the signal in the worst case must be determined. Prelim-

inary measurements [87] and simulation [88] have shown that the worst case is for the particle hitting the far end of the scintillator at the bottom of the scintillator (position 2 in Figure B.1). The attenuation of the signal along the scintillator as well as the attenuation along the light pipe or through the glue joints were also measured by measuring the amplitude of signals produced in position 1, 2 and 3 of Figure B.1. Those data allow us to differentiate between bad glue joints and a bad scintillator. The data of attenuation along the scintillator can be compared to data after data-taking with beam to indicate possible yellowing of the scintillator.

The most straightforward way to do such measurements is to use a collimated radioactive source (known amount of energy deposit) located in different positions along the scintillator. The ratio of the signal for position 2 and 3 (see Figure B.1) gives the attenuation along the scintillator. The measurement in position 3 gives the average number of photo-electrons, useful to compare from one scintillator to another one. For this measurement, a Ru-106 source [89] was used. It emits betas up to a maximum energy of 3.5 MeV. By using the appropriate trigger (requiring the betas to traverse both scintillators and the plastic spacer) and discriminator threshold, one is able to select only the most energetic part of the beta spectrum. The energy deposited by the beta is 1.97 MeV per cm. Those measurements have been carried out for 41 scintillator pairs out of the total of 64.

This method is tedious and cannot be used once the detector is enclosed in the light tight box. Part of the calibration of the light pipes were carried out using cosmic (μ) rays with the octants oriented such that the scintillators were concave towards the earth and the scintillator faces perpendicular to the ground. The cosmic trigger required all four PMTs on one detector to fire and two of the PMTs from an adjacent detector to fire. This method is quicker as one can test many light pipes

at a time. Also, this method can be used once the detectors are in the hall (and enclosed in the light tight box). While the energy deposited (per cm) by cosmic rays is known, the path the cosmic takes through the scintillators is not known. For this reason, the signals produced by cosmic rays were calibrated by comparing them with the signals produced by the Ru source located in position 3 on Figure B.1. The calibration was performed on all scintillators of Octant 7. As a result it appears that one can use a constant multiplicative conversion factor between the cosmic and Ru-106 amplitudes. The ratio of Ru-106 to cosmic amplitudes is plotted in Figure B.2. The 10% dispersion in the data, is mostly due to the precision which which the cosmic peak was located on the ADC distributions. No significant variation of this ratio was found as a function of the size of the scintillator. Also, the data for cosmic runs were taken with the same HV being applied on the PMT, thus the photo-electron calibration precision does not contribute to the dispersion. Using this method, one can measure the average number of photo electrons produced by the light pipes. It is possible to measure the attenuation of the signal along the scintillator using the cosmic ray data. A careful measurement of the time arrival of signals between each other allows us to locate the hit position. Though the principle was demonstrated, the quality of the data taken at that time did not allow us to extract this information. The cosmic method was applied to the 23 scintillator pairs that were not measured using the source method.

Results and extrapolation to the G^0 case.

Raw results of the testing are presented in the upper plots of Figure B.3. The results are three-fold. Each scintillator end is characterized by :

1. the number $N_{\gamma e}(mid)$ of photo-electrons produced by a minimum ionizing particle crossing it in its geometrical middle (position 3 on Figure B.1).

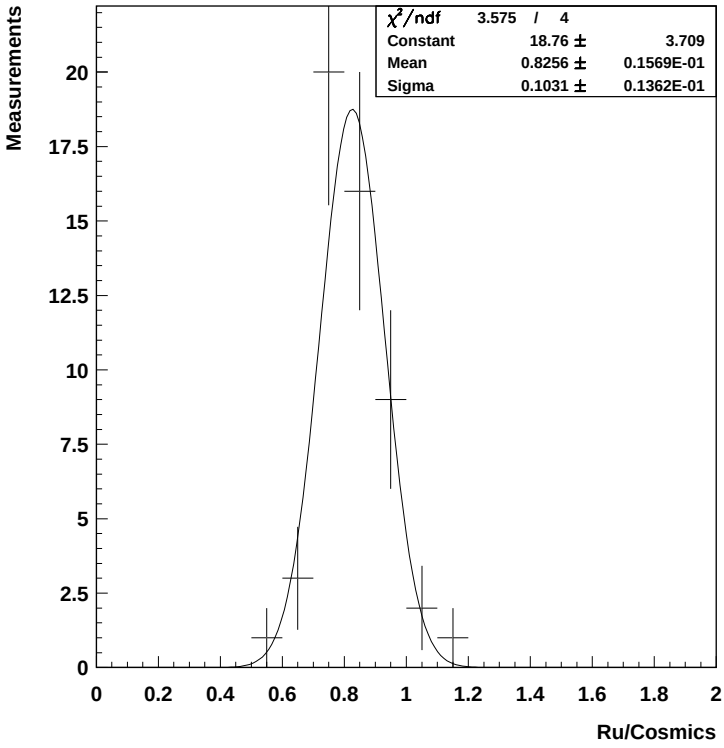

FIG. B.2: *Calibration of the signal produced by non-collimated cosmic rays crossing the scintillator against the signal produced by the Ru source located in the middle of the scintillator. Those data represent the calibration of the signal for all scintillators of Octant 7.*

2. the attenuation (A^{far}_{scint}) of the signal from the far end to the geometrical middle (signal of position 3 over signal on position 2 on Figure B.1)

3. the attenuation (A^{close}_{scint}) of the signal from the geometrical middle to the close end (signal on position 1 to signal on position 3 on Figure B.1)

The analysis of the raw data shows that scintillators of the same size with the same light-guide configuration[3] gives in average similar results (see lower plots of Figure B.3). Moreover the dispersion of 10% on $N_{\gamma e}$ can be interpreted as a result of the 10% precision on the photo-electron calibration. In other words, no scintillator

[3]Front light pipe and back light pipe do not have the same light-guide geometry.

shows a significantly better or worse performance than equivalent other detectors. This is also the case with A_{scint}^{close}, moreover for this variable, the analysis of the data shows that this attenuation is independent of the scintillator size and is found to be 1.44 ± 0.05. As a result, the average values (see Figure B.3: middle plots and Table B.1) are going to be used to extrapolate data to the G^0 case.

The following equation describes the extrapolation of the Clean Room data to the minimum number of photo-electrons $N_{\gamma e}(g0)$ produced by G^0 particles hitting the scintillators.

$$N_{\gamma e}(g0) = < N_{\gamma e}(mid) > \times \underbrace{\Delta E(g0)/\Delta E(Ru)}_{energy\ normalization} \times < A_{scint}^{far} > \tag{B.3}$$

For the G^0 backward running, the energy normalization is 1 as electrons are detected : $\Delta E(g0) = \Delta E(Ru)$ is the energy lost by minimum ionizing particles. For the G^0 forward running, $\Delta E(g0)$ is lost by low-energy protons hitting the scintillators. The variation of energy lost by protons from one scintillator size to the other one is significant [88]. For example the energy lost by the proton in scintillator 5 (1 cm thickness) is on average 9.3 MeV whereas the energy lost in scintillator 16 (1 cm thickness) is on average 3.0 MeV. Moreover, this energy loss can vary by up to 25% across the face of a single scintillator; the minimum energy lost is for protons crossing the scintillator on the top as they are the more energetic. This minimal energy loss is considered for the computation of $N_{\gamma e}(g0)$. This is the absolute worst case scenario, as one is combining the least energy deposited (top of the scintillator) with the worst transmission (bottom far end of the scintillator). The energies taken into account for the extrapolation to the G^0 forward running are given in Table B.2, they have been computed using the Bethe-Bloch formula. The computation takes into account the different materials crossed by the protons before hitting the scintillators ; the main losses occur in the LH2 target, the air gap and, when relevant, the

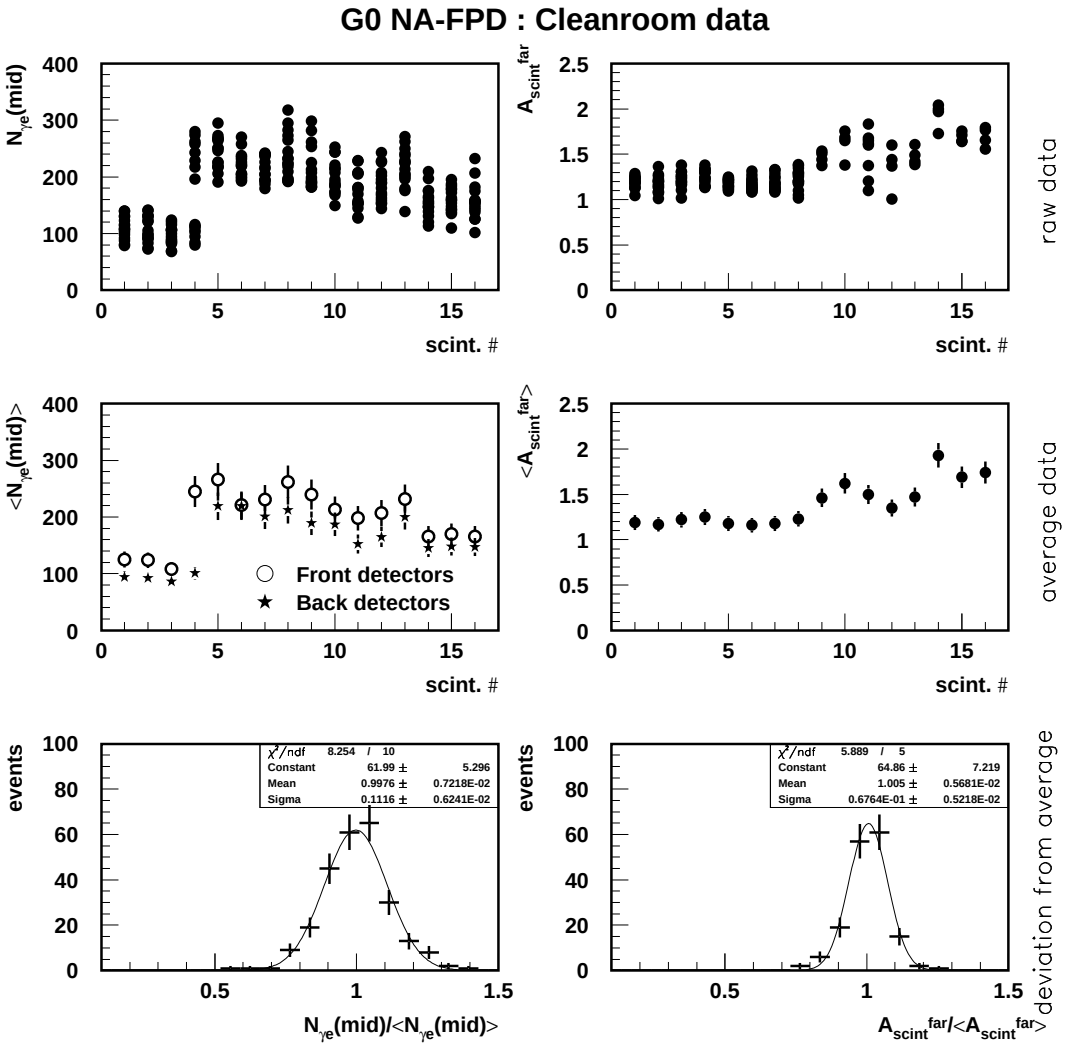

FIG. B.3: *Results of the testing with minimum ionizing particles. The tests were performed with the Ru radioactive source or with cosmic rays, following a procedure described in Section B.1.1. The left plots refer to the average number of photo-electrons, while the right ones refers to the attenuation of the signal from the far end of the detector to the average signal. Upper plots show the raw data, middle plots show the average value on a scintillator size to scintillator size basis, lower plots show the deviation of the actual data (upper plot) to the average value (middle plot) again on a scintillator size to scintillator size basis.*

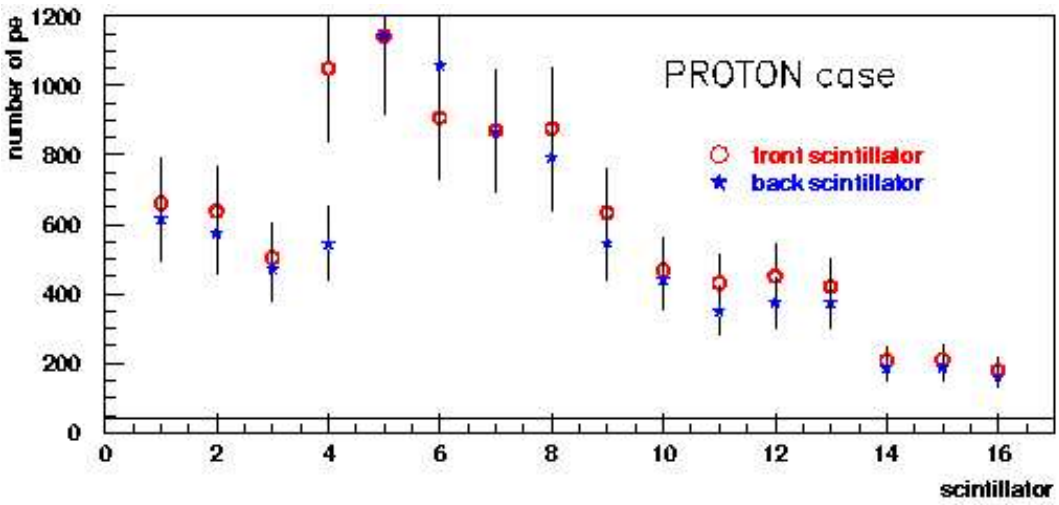

FIG. B.4: *Minimum number of photo-electrons detected by the G^0 NA FPD in the case of the proton forward angle running running. Error bars on these predictions are 20%. Note that detector 4 is made up of 1 cm thick front scintillator and 0.5 cm thick back scintillator. The horizontal line indicates the design minimum value of 40 photoelectrons.*

front scintillator and the polycarbonate. The minimum number of photo-electrons produced in the NA-FPD light pipes in the cases of the G^0 running is presented in Table B.2 as well as in Figure B.4. The error associated with this estimation is the quadratic sum of the precision on the photo-electron calibration (10%), the estimation on the stability (from one tube to another one) of the quantum efficiency of the PMTs (15%) and the precision of the energy loss computation (10%). The total precision is therefore 20%.

In this worst case estimation, the number of photo-electron produced by the North American Focal Plan Detectors (NA FPD) is always larger than 40 photo-electron. Moreover, the number of photo-electrons produced in the Forward case running is always larger than 100. This minimum should allow for the time of flight measurement. As a conclusion, the NA FPD produce more than enough light to insure a good measurement when mounted in the Clean Room.

The next section explains how the PMT were matched to the light pipes.

Clean Room data : minimum ionizing particle.								
Scintillator	1	2	3	4	5	6	7	8
$< N_{\gamma e}(mid) >$ front	125	124	108	245	266	221	231	262
$< N_{\gamma e}(mid) >$ back	94	92	86	101	219	219	201	212
$< A^{far}_{scint} >$	1.19	1.17	1.22	1.25	1.18	1.16	1.18	1.23

Scintillator	9	10	11	12	13	14	15	16
$< N_{\gamma e}(mid) >$ front	240	213	198	207	232	166	170	166
$< N_{\gamma e}(mid) >$ back	189	187	152	165	200	145	148	147
$< A^{far}_{scint} >$	1.46	1.62	1.50	1.35	1.47	1.93	1.69	1.74

TABLE B.1: *Results of the testing with minimum ionizing particles.* $N_{\gamma e}$ *front,*$N_{\gamma e}$ *back and* A^{far}_{scint} *(and their errors) are defined in the text.*

Proton case : forward running for G^0								
Scintillator	1	2	3	4	5	6	7	8
$\Delta E(g0)$ front	6.19	5.92	5.59	10.5	9.98	9.37	8.75	8.11
$\Delta E(g0)$ back	7.68	7.17	6.59	6.62	12.1	11.0	10.0	9.06
$N_{\gamma e}(g0)$ front	660	637	502	1049	1142	906	870	877
$N_{\gamma e}(g0)$ back	616	572	472	543	1143	1058	866	793

Scintillator	9	10	11	12	13	14	15	16
$\Delta E(g0)$ front	7.58	6.99	6.41	5.78	5.23	4.73	4.10	3.68
$\Delta E(g0)$ back	8.31	7.53	6.79	6.03	5.41	4.84	4.16	3.71
$N_{\gamma e}(g0)$ front	633	467	430	450	419	207	209	178
$N_{\gamma e}(g0)$ back	546	441	349	374	374	185	185	159

TABLE B.2: *Minimum energies left (in MeV) by the protons (G^0 forward running) hitting the G^0 scintillators and subsequent number of photo-electrons detected. The energies left take in account the variation of scintillator thickness.*

B.1.2 PMT attributes

To understand the characteristics of the scintillator and light pipes, the previous measurements were performed using the same eight PMTs. The characteristics of those eight PMT were very well known : their gains were tracked on a regular basis, and their relative quantum efficiencies measured. After these tests had been performed, each detector had to be fitted with its own PMT.

Gain Matching

The goal of the gain matching process was to pair the PMTs to specific light pipes such that if one applies a given HV value to all of them, the output signal will be roughly equivalent. In other words, one tried to compensate for the variation in the number of photo-electrons ($N_{\gamma e}(g0)$) produced by the G^0 particles (see Figure B.4) by carefully choosing the gain ($gain(HV)$) of the PMTs at a given HV. That is :

$$N_{\gamma e}(g0) \times gain(HV) \propto amplitude = constant. \tag{B.4}$$

For this computation, the PMT gains measurements performed at JLab [90] were used. Those measurements were performed using a regular resistive basis and not the final Zener-resistance G^0 basis. The number of photo-electrons ($N_{\gamma e}(g0)$) used for this pairing are the ones corresponding to the forward angle setup,in which protons will be measured. There was nearly a perfect gain match for detectors 1 through 12 (see Figure B.5). The last three detectors required a gain that could not as easily be matched to a PMT of sufficient gain to compensate the lower number of photo-electrons. The PMTs on these later detectors will have a higher voltage applied to them compared to the lower detectors.

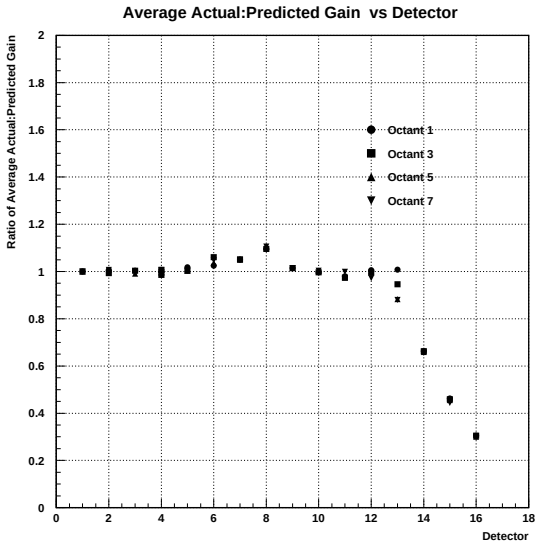

FIG. B.5: *Ratio of the gain of the actual PMT attached to the light pipe to the gain necessary to perfectly match the light pipe. For detectors 13 through 16, not perfectly matched PMT have to be used. This implies that the high voltage will be higher on these detectors in comparison with the other detectors.*

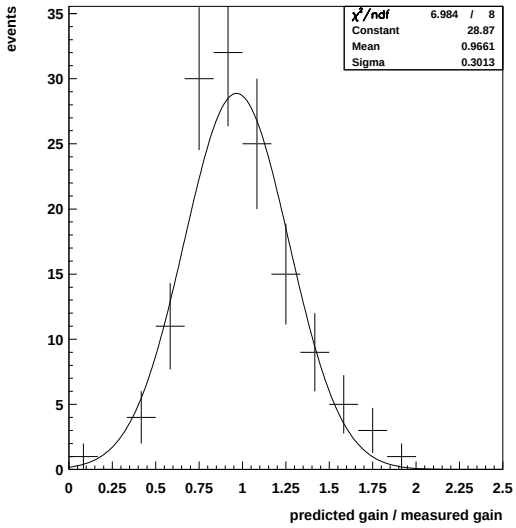

FIG. B.6: *Dispersion of the ratio of the measured to the predicted cosmic amplitudes in the Clean Room. The 31% error is due to the gain measurements, the assumed quantum efficiency, and to the fitting of the cosmic and pe peak for the Ru.*

Gain Balancing

The optimization described in the previous section is based on the use of various data sets. It also supposed that the quantum efficiency of all PMTs is equivalent. In order to check the validity of the previous matching as well as the running of the bases and the tubes, a cosmic measurement was performed on all the light pipe equipped with their proper PMTs. In addition, cosmics were available in both the Clean Room and down in Hall C. This meant that results in the Clean Room could be compared with results after moving the octants into Hall C. The amplitude of the signal produced by cosmics rays going through whatever scintillators is brought to a constant value by adjusting the HV applied to the PMT.

Using the procedure described in Section B.1.2, one is able to compute the HV which should be applied to the tube so that the cosmic peak will have a given amplitude[4]. In this case one should take care of correction factors not considered in Equation B.4, that is :

$$amplitude \propto N_{\gamma e}(g0) \times gain(HV) \times PMT_{QE} \times A_{cable} \tag{B.5}$$

where PMT_{QE} is the quantum efficiency of the tube and A_{cable} is the attenuation of the signal through the cable between the PMT and the ADC channel. For this measurement A_{cable} was known. The variation[5] of the attenuation from one cable to another one was corrected for.

Figure B.6 shows the ratio of the signal amplitude produced by the actual light pipe with the amplitude expected. The ratio is distributed as a Gaussian of sigma 31%. The larger part of this dispersion can be explained by taking in account the precision of the data used to compute this ratio :

[4]Note: In this case minimum ionizing particles are used and not protons as discussed in Section B.1.2

[5]Different types of Lemo cables were used, the older set eventually transmit only 88%($\pm$ 2%) of the portion transmitted by the newer set.

- The actual amplitude is measured with a precision of 10%.
- The precision on the number of photo-electron produced by each light pipe : 10%.
- The dispersion in the quantum efficiency of the tubes: 15%
- The knowledge of the gain of each tube : 15%. This value is estimated by comparing the gain of the eight tubes used for the initial calibration with the one given in [90].

This yields an error of 25%. Thus the gain balancing process appears as a successful cross check of our previous work and of the assumptions made during testing.

From these measurements the high voltage was then adjusted until the cosmic peaks were aligned within 10%. From this data, the high voltage can also be adjusted for the G^0 proton case for the experiment. In that case, one should take in account the appropriate energy loss in the scintillator.

APPENDIX C

Injector Studies

C.1 Overview of 2002 Results

The G^0 commissioning run began in August 2002 until the end of January 2003. This was an opportunity to test many of the systems under G^0 running conditions. This appendix discusses results of the commissioning run to understand the helicity correlated devices at the source that were monitored by the injector DAQ system.

C.1.1 BPM Noise

The BPMs used in the injector are the standard JLab stripline BPMs. These BPMs are made up of four antennae situated symmetrically about the beam pipe. When the electron beam passes through the stripline BPM, rf signals are picked up by the monitors:

$$\text{BPM Antenna Signals} \propto (\text{Beam position}) \times (\text{Beam Intensity}).$$

The position (or position difference) calculated from beam monitors have a certain amount of noise associated with it. This noise is due to beam noise and to electronic noise. The measured noise can be written as:

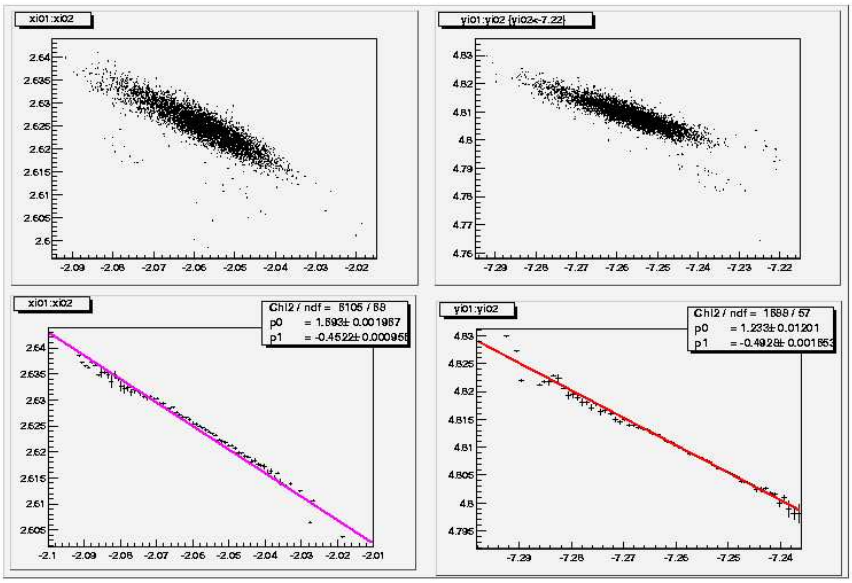

FIG. C.1: *The top two plots show the BPM resolution. The bottom two plots are the profile plots of the top scatter plots. These profile plots can now be fitted and one axis can be used to predict the position of one BPM from the measured position in another BPM.*

$$\sigma^2_{measured} = \sigma^2_{beam} + \sigma^2_{instrumental}.$$

The instrumental noise can be found by using three BPMs along the beamline without magnetic optics between the monitors. The first two BPMs can be used to determine the position of the beam in the third monitor. This predicted behavior can then be removed from the measured signal of the third BPM leaving behind only the instrumental noise. This analysis has been done when looking at absolute positions and position differences. See Table C.2 and Table C.1 for results.

Another method for finding the instrumental noise of the BPM is to take a run without beam but at a gain comparable to when beam is present. This is just a typical pedestal run in 'Forced Gain Mode', then in the analyzer code a typical beam signal is injected into the BPM ntuple channels. Results of this analysis can

be found in Table C.3.

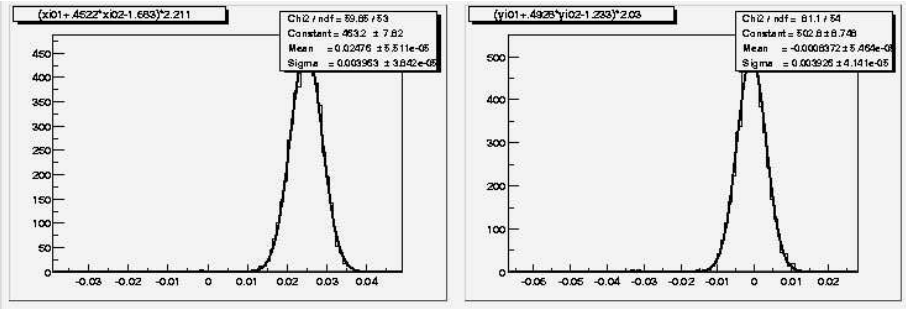

FIG. C.2: *These are plots of the instrumental noise of the BPMs. After predicting the position of the beam in a BPM from the above plots, the predicted position of the beam can be subtracted from the BPM signal leaving behind only the instrumental noise of the BPM.*

It is not known why these results do not agree with one another. One reason why these results might be inconsistent is that it takes two BPMs to predict the location of the beam in a third BPM. This was not done in the above analysis since there are magnetic elements between many of the BPMs in the injector.

Electronic BPM noise found by predicting and subtracting position differences		
BPM	X Instr Noise (μm)	Y Instr Noise(μm)
1i02	7.419 ± 0.077	9.793 ± 0.113
1i04	16.380 ± 0.172	11.360 ± 0.133
1i06	22.400 ± 0.226	6.363 ± 0.067
0L02	14.790 ± 0.232	16.799 ± 0.172
0L03	16.610 ± 0.162	30.150 ± 0.322
0I05	6.449 ± 0.066	13.200 ± 0.144
0I02A	-	-

TABLE C.1: *Electronic noise calculated from position differences.*

Electronic BPM noise found by predicting and subtracting positions		
BPM	X Instr Noise (μm)	Y Instr Noise(μm)
1i02	1.769 ± 0.016	1.932 ± 0.029
1i04	3.738 ± 0.037	3.702 ± 0.040
1i06	3.890 ± 0.037	5.277 ± 0.060
0L02	14.830 ± 0.207	3.584 ± 0.034
0L03	17.850 ± 0.209	11.970 ± 0.116
0I05	3.747 ± 0.034	2.875 ± 0.030
0I02A	-	-

TABLE C.2: *Electronic noise from calculating positions.*

Electronic BPM noise found by injecting a fake BPM signal		
BPM	X Instr Noise (μm)	Y Instr Noise(μm)
1i02	1.682 ± 0.120	30.735 ± 1.004
1i04	41.70 ± 3.172	4.756 ± 0.191
1i06	18.330 ± 2.183	7.813 ± 0.289
0L02	0.536 ± .0300	2.026 ± 0.057
0L03	9.008 ± 0.291	0.041 ± 0.002
0I05	2.398 ± 0.123	3.431± 0.090
0I02A	4.451 ± 0.144	5.121 ± 0.156

TABLE C.3: *Electronic noise by taking a pedestal run and injecting a fake signal.*

C.1.2 PZT

From the 2001-2002 G^0 commissioning run, the following PZT calibration slopes were measured by different monitors in the injector.

From December 19, 2002:

BPM	QPD		1i02		1i04		1i06		0L02	
	ΔX	ΔY	ΔX	ΔY	ΔX	ΔY	ΔX	ΔY	ΔX	ΔY
X-PZT	-464	-2393	3642	-6253	-2016	7916	-1403	4684	-213	-1162
Y-PZT	4876	-217	11750	4454	-1350	-2800	-7211	-984	-5596	-1424

TABLE C.4: *The responses of the injector BPM's position differences to the X and Y motion of the PZT mirror on December 19, 2002. These slopes are given in nm/V*

Device	QPD	1i02	1i04	1i06	0L02	BCM
	ΔQ	ΔQ	ΔQ	ΔQ	ΔQ	ΔQ
X-PZT	6	-147	-185	-183	-197	-251
Y-PZT	335	-577	-606	-523	-773	-955

TABLE C.5: *The responses of the injector BPM's charge asymmetries to the X and Y motion of the PZT mirror on December 19, 2002. These slopes are given in ppm/V.*

BPM	QPD	1i02	1i04	1i06	0L02
θ	34	98	88	79	64

TABLE C.6: *These results are the angle (in degrees) between the responses of the PZT motion in X and in Y on December 19, 2002 . This is a method of observing the orthogonality of the PZT motion.*

From January 14, 2003:

BPM	QPD		1i02		1i04		1i06		0L02	
	ΔX	ΔY	ΔX	ΔY	ΔX	ΔY	ΔX	ΔY	ΔX	ΔY
X-PZT	-1375	3204	-2595	4910	2036	-7083	824	-2913	1393	2534
Y-PZT	-1531	-818	9338	4684	-11550	-321	-4585	-346	-7029	-308

TABLE C.7: *The responses of the injector BPMs to the X and Y motion of the PZT mirror on January 14, 2003. These slopes are given in nm/V.*

Device	QPD	1i02	1i04	1i06	0L02
	ΔQ	ΔQ	ΔQ	ΔQ	ΔQ
X-PZT	256	6	2	4	-16
Y-PZT	603	-319	-331	-313	-162

TABLE C.8: *The responses of the injector BPM's charge asymmetries to the X and Y motion of the PZT mirror on January 14, 2003. These slopes are given in ppm/V.*

BPM	QPD	1i02	1i04	1i06	0L02
θ	95	91	104	102	115

TABLE C.9: *These results are the angle (in degrees) between the responses of the PZT motion in X and in Y on January 14, 2003. This is a method of observing the orthogonality of the PZT motion.*

From January 24, 2003:

BPM	QPD		1i02		1i04		1i06		0L02	
	ΔX	ΔY	ΔX	ΔY	ΔX	ΔY	ΔX	ΔY	ΔX	ΔY
X-PZT	18	2295	-1936	2436	3856	2138	735	-3553	931	919
Y-PZT	-2557	-810	5648	523	11570	500	-6078	-1067	-2397	-339

TABLE C.10: *The responses of the injector BPM's position differences to the X and Y motion of the PZT mirror on January 24, 2003. These slopes are given in nm/V.*

Device	QPD	1i02	1i04	1i06	0L02
	ΔQ	ΔQ	ΔQ	ΔQ	ΔQ
X-PZT	852	-71	-88	-77	2
Y-PZT	565	-238	-364	-314	-245

TABLE C.11: *The responses of the injector BPMs to the X and Y motion of the PZT mirror on January 24, 2003. These slopes are given in ppm/V.*

BPM	QPD	1i02	1i04	1i06	0L02
θ	108	123	149	92	143

TABLE C.12: *These results are the angle (in degrees) between the responses of the PZT motion in X and in Y on January 24, 2003 . This is a method of observing the orthogonality of the PZT motion.*

The PZT was calibrated with only G^0 beam in the injector on three days during the commissioning run. It is difficult to make a comparison with such a small sample. The PZT response as measured in Hall C showed erratic behavior that was not understood at the time. G^0 will investigate further the response of the PZT on the bench between the end of the February 2003 and the beginning of the second 2003 engineering run.

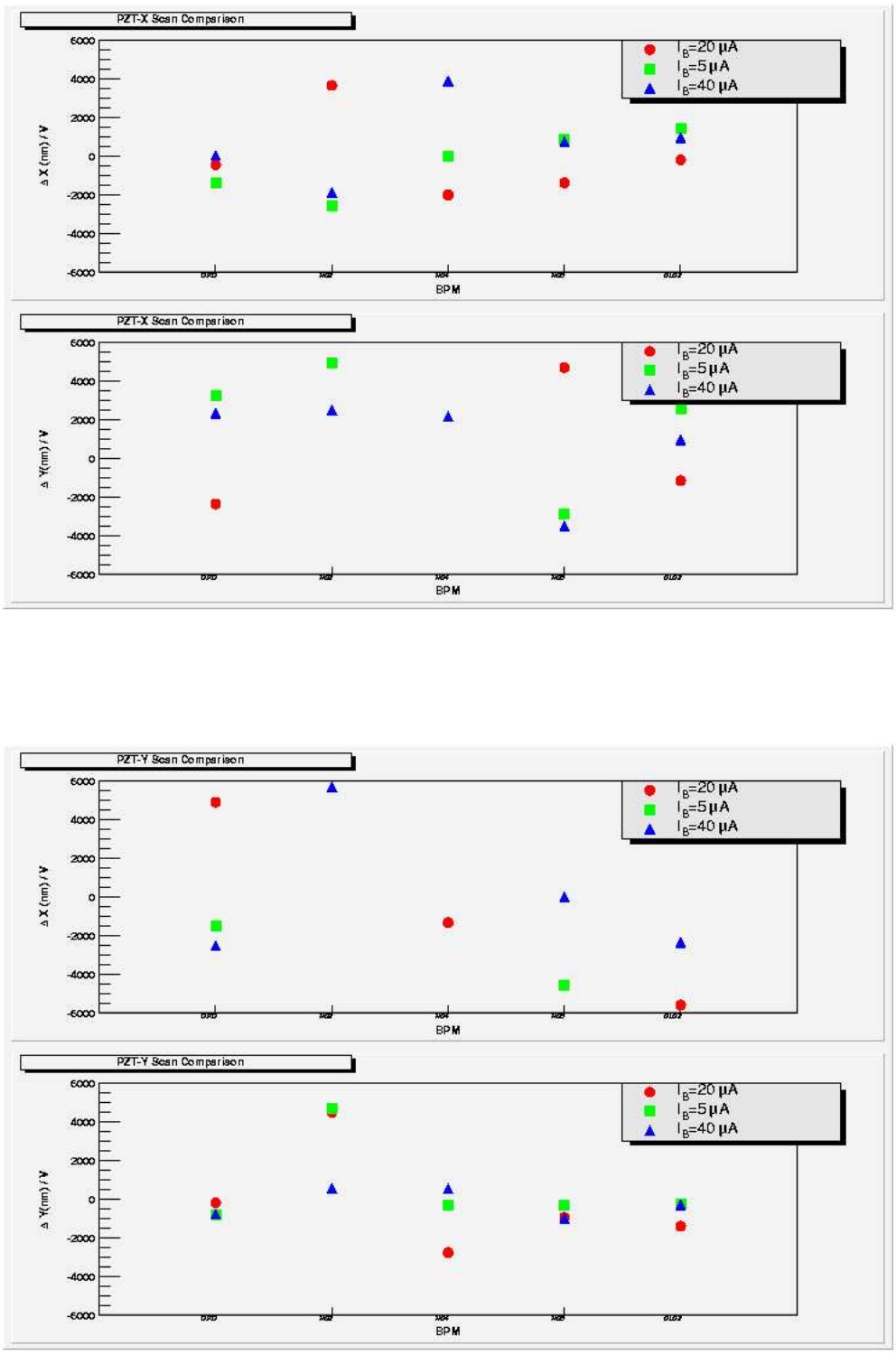

FIG. C.3: *These are plots of the helicity correlated position differences in X and Y as a function of PZT X and Y motion and as a function of beam monitor in the injector.*

Adiabatic Damping (Transverse Magnification)

If the energy of the electron beam increases much slower (adiabatically) than the betatron oscillations, then the normalized emittance will remain constant while the unnormalized emittance (that is the actual beam size) will shrink. This means that the transverse size of the beam as measured in Hall C should be smaller than what is measured in the injector. During the HAPPEX experiment there was so much adiabatic damping that they did not need to run position feedback. The adiabatic damping should be about a factor of 20 in suppression between the injector and Hall C. This was demonstrated during the HAPPEX running. Besides benefiting from the smaller position differences in the hall, adiabatic damping is an indicator of the quality of the accelerator setup.

The first measurements of the adiabatic damping factor was performed on March 18,2002. At this time, the adiabatic damping was defined as:

$$\frac{centroid\ \ \Delta X\ \ at\ \ Hall\ \ A\ \ \ target\ \ BPM}{centroid\ \ \Delta X\ \ at\ \ injector\ \ 0L02\ \ BPM}.$$

Measurements were made with both the Hall A diode laser and a homemade Ti:Sapphire laser, the following was observed for each laser respectively:

- $\frac{1100\pm100nm}{24568\pm1373} \sim 0.045 \pm 0.005 \rightarrow \sim 22 \pm 2$
- $\frac{1200\pm70nm}{34380\pm1584} \sim 0.035 \pm 0.003 \rightarrow \sim 29 \pm 3.$

During the G^0 commissioning run, three opportunities were available to measure the adiabatic damping between the injector and Hall C. The reason for so few opportunities was due to the fact that other experimental halls were operational meaning the other hall's beam would be present in the injector making the measurement difficult to do. From April 2002, BPM 0L02 was the reference BPM in the injector due to the fact that this BPM had the largest response. This response has

changed during the commissioning run and all the BPMs in the injector that were read out by the G^0 injector DAQ were examined.

The method for observing the adiabatic damping had further been improved for the commissioning run. Instead of only looking at the position differences between BPMs in the injector and in the hall the G^0 PZT mirror located on the laser table was utilized. Now the ratio of the responses of the PZT mirror in X and Y are used to find the adiabatic damping:

$$Adiabatic\ Damping\ in\ X = \frac{\sqrt{XX^2+YX^2}}{\sqrt{XX^2+YX^2}}$$

$$Adiabatic\ Damping\ in\ Y = \frac{\sqrt{XY^2+YY^2}}{\sqrt{XY^2+YY^2}}$$

where:

- XX = Δ X as one varies PZT X
- YX = Δ Y as one varies PZT X
- XY = Δ X as one varies PZT Y
- YY = Δ Y as one varies PZT Y

BPM	QPD	1i02	1i04	1i06	0L02
Varying PZTx(12/19/02)	1.0	3.5	3.5	2.1	0.5
Varying PZTy(12/19/02)	3.3	8.6	9.4	4.9	3.9
Varying PZTx(01/16/03)	3.4	5.3	7.1	2.9	2.8
Varying PZTy(01/16/03)	3.0	18.0	20.0	7.9	12.2
Varying PZTx(01/24/03)	2.9	3.9	5.6	4.6	1.7
Varying PZTy(01/24/03)	10.4	22.1	45.1	14.4	9.4

TABLE C.13: *Results of the adiabatic damping as measured during G^0 commissioning.*

In conclusion, the adiabatic damping as measured at BPM 0L02 falls short of the factor of 20 that is expected. This might be due to the fact that 0L02 now sits at

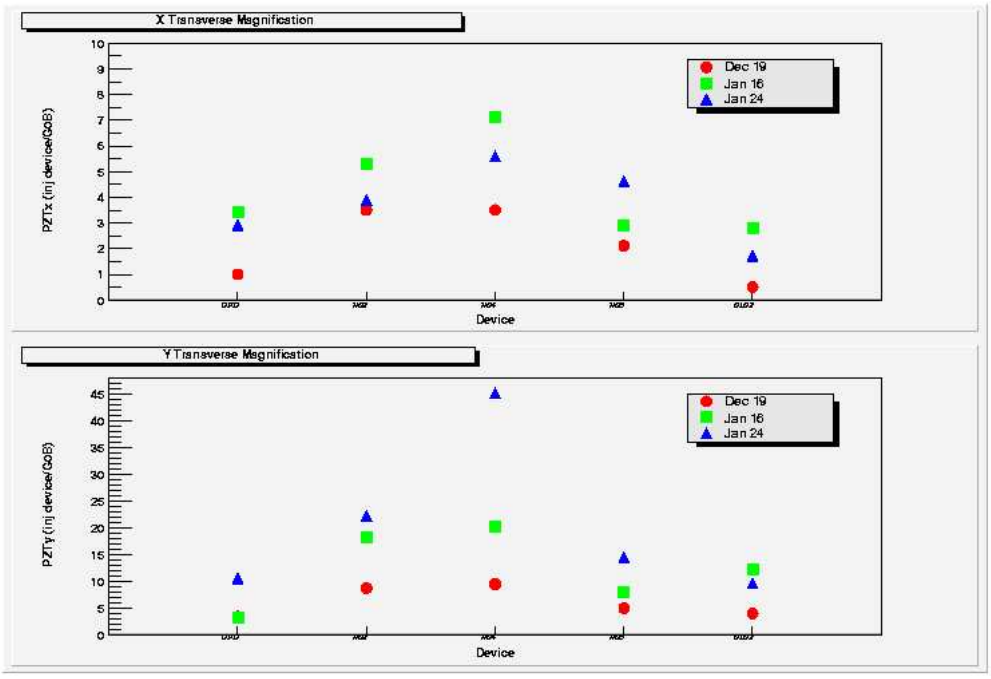

FIG. C.4: *Adiabatic damping is defined to be the ratio of position differences in the injector (quadrant photodiode, BPM 1i02, 1i04, 1i06, and 0L02) to the hall monitor (BPM G0B). The adiabatic damping as measured on the three dates indicated. Data taken on December 19, 2002 was at a beam current of 20 μA. Data taken on January 16, 2003 was at a beam current of 5 μA. The data taken on January 24, 2003 was at a beam current of 40 μA. The top plot is the adiabatic damping as one varies the x PZT. The bottom plot is the adiabatic damping as one varies the y PZT.*

the waist of the beta function of the machine when these measurements were made. After a better tune of the machine can be found for the G^0 beam, work should be done to find which BPM is most sensitive in the injector and use that as a reference.

C.1.3 Intensity Attenuator Cell

The following are results from the 2002-2003 G^0 commissioning run:

BPM	QPD		1i02		1i04		1i06		0L02	
	ΔX	ΔY	ΔX	ΔY	ΔX	ΔY	ΔX	ΔY	ΔX	ΔY
12/17	-383	55	-459	407	624	320	332	123	-238	-5
12/16	563	1149	-304	359	13	448	-342	229	-185	-32
12/15	23	9	-448	585	-129	460	-699	491	-1321	-354
12/15	181	210	-5343	4515	-178	-159	-439	613	-1104	-89
12/15	6	24	-401	506	n/a	619	-501	354	-258	71
12/12	123	116	-398	585	-533	535	-1164	781	-1894	-36
12/05	727	721	-1063	1260	-320	733	-842	756	157	131

TABLE C.14: *The IA slopes for position differences in nm/V measured in December 2002.*

Device	QPD	1i02	1i04	1i06	0L02	BCM	0L03
	ΔQ	ΔQ	ΔQ	ΔQ	ΔQ	ΔQ	ΔQ
12/17	553	497	504	403	348	436	416
12/16	531	472	370	327	267	352	310
12/15	549	496	492	424	221	238	267
12/15	551	505	511	450	375	481	463
12/15	550	305	485	218	272	272	270
12/12	542	502	497	424	84	94	95
12/05	543	467	520	438	237	288	301

TABLE C.15: *The IA slopes for charge asymmetry in ppm/V.*

The IA responded well during the commissioning offering a large (~ 400 ppm/V) charge asymmetry calibration though it did generate large position differences. The IA calibration constants were very stable over time requiring new measurements of this constant every couple of days. Work to minimize the position differences induced by the IA will begin after the 2002-2003 commissioning run.

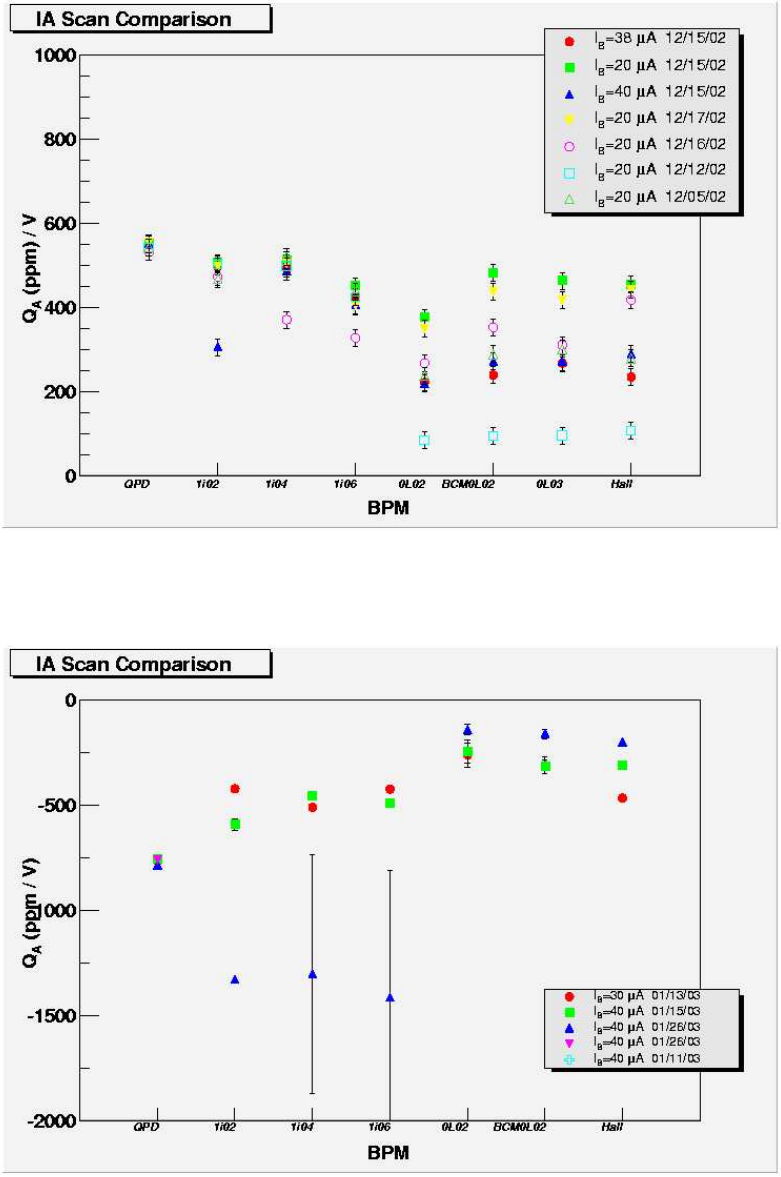

FIG. C.5: *Charge asymmetry calibration constants (ppm/V) for the IA. Note that the values at the QPD are consistent with one another over both months. Note the values from 1I02 to 1I06 are consistent with one another. Between 1I06 and 0L02 are a variety of apertures such as A1, A2, the Chopper, etc. It is due to scraping on these apertures that*

BIBLIOGRAPHY

[1] J. Gasser, H. Leutwyler and M.E. Sanio, Phys. Lett. B**253**, 252 (1991).

[2] J. Gasser, H. Leutwyler, Phys. Rep **87**, 77 (1982).

[3] J. Gasser, Ann. Phys. **136**, 62 (1981).

[4] K. Abe et al., Phys. Lett. B**405**, 180 (1997).

[5] G. Altarelli et al., Nucl. Phys. B**496**, 337 (1997).

[6] G.P. Zeller et al., Phys. Rev. Lett. **88**, 091802 (2002).

[7] S. Okubo, Phys. Lett. B**5**, 165 (1963); G. Zweig, CERN Report 8419/TH412 (1964); I. Iizuka, Prog. Theor. Phys. Suppl. **21**, 37 (1966).

[8] A. Bertin et al., Phys. Lett. B**388**, 450 (1996).

[9] M.P. Rekalo et al., Z. Phys. A**357**, 133 (1997).

[10] J. Ellis and R. Jaffe, Phys. Rev. D**9**, 1444 (1974).

[11] J. Ashman et al., Phys. Lett. B**206**, 364 (1988).

[12] T. Adams et al.,Strange Content of the Nucleon (NuTeV). In *Physics with a High Luminosity Polarized Electron Ion Collider*edited by L.C. Bland, A.P.Szczepaniak, and J.T. Londergan, p. 337 (World Scientific, 2000).

[13] D.T. Spayde et al., Phys. Lett. B**583**, 79 (2004).

[14] K.A. Aniol et al., Phys.Rev. C**69**, 065501 (2004).

[15] E.J. Beise et al., Nucl. Instrum. Meth. A**378**, 383 (1996).

[16] M.N. Rosenbluth, Phys. Rev. **79**, 615 (1950).

[17] N.F. Mott, Proc. Roy. Soc. A**124**, 425 (1929).

[18] P.Bosted et al., Phys. Rev. Let. **68**, 3841 (1992).

[19] A.F. Sill et al., Phys. Rev. D**48**, 29 (1993).

[20] J. Arrington, Phys. Rev. C**68**, 034325 (2003).

[21] E.J. Brash et al., Phys. Rev. C**65**, 051001 (2002).

[22] A.I. Akhiezer and M.P. Rekalo, Sov. J. Part. Nucl. **3**, 277 (1974); R. Arnold, C. Carlson, and F. Gross, Phys. Rev. C**23**, 363 (1981).

[23] J. Litt et al., Phys. Lett. B**31**, 40 (1970).

[24] Ch. Berger et al., Phys. Lett. B**35**, 87 (1971).

[25] L.E. Price et al., Phys. Rev. D**4**, 45 (1971).

[26] W. Bartel et al., Nucl. Phys. B**58**, 429 (1973).

[27] R.C. Walker et al., Phys. Rev. **49**, 5671 (1994).

[28] L. Andivahis et al., Phys. Rev. D**50**, 5491 (1994).

[29] B. Milbrath et al., Phys. Rev. Lett. **80**, 452 (1998); erratum Phys. Rev. Lett. **82**, 221 (1999).

[30] M.K. Jones et al., Phys. Rev. Lett. **84**, 1398 (2000).

[31] O. Gayou et al., Phys. Rev. Lett. **88**, 092301 (2002).

[32] P.G. Blunden, W. Melnitchouk, J.A. Tjon, Phys. Rev. Lett. **91**, (2003).

[33] P.A.M. Guichon, M. Vanderhaeghen, Phys. Rev. Lett. **91**(2003).

[34] A. Lung et al., Nucl. Rev. Lett. **70**, 1719 (1993).

[35] S. Galster et al., Nucl. Phys. B**32**, (1971).

[36] T. Eden et al., Phys. Rev. C **50**, 1749 (1994).

[37] C. Herberg et al., Eur. Phys. J A**5**, 131 (1999).

[38] M. Ostrick et al., Phys. Lett. **83**, 276 (1999).

[39] D. Rohe et al., Phys. Rev. Lett. **83**, 4257 (1999).

[40] J. Becker et al., Eur. Phys. J A**6**, 329 (1999).

[41] M.Meyerhoff et al., Phys. Lett. B**327**, 201 (1994).

[42] F. Halzen and A.D. Martin, *Quarks and Leptons*(John Wiley & Sons, New York, 1984).

[43] Particle Data Group, Euro. Phys. J. C**54**, 1 (2000).

[44] W.M. Albenico et al., Phys. Rep. 3 **58**, 182 (1995).

[45] G.P. Ramsey et al., Int. J. Mod. Phys. A**18** , 1211 (2003)

[46] G.A. Miller, Phys. Rev. C**57**, 1492 (1998).

[47] E. Hadjimichael, G.I. Poulis, and T.W. Donnelly, Phys. Rev. C**45**, 2666 (1992).

[48] L.Diaconescu, R. Schiavilla, and U. van Kolck, Phys. Rev. C**63**, 4007 (2001).

[49] S.-L. Zhu, S. J. Puglia, B. R. Holstein, and M. J. Ramsey-Musolf, Phys. Rev. D**62**, 033008 (2000).

[50] H.-W. Hammer, S.J. Puglia, M.J. Ramsey-Musolf, and S.-L. Zhu, Phys. Lett. B**562**, 208 (2003).

[51] F.E. Maas et al., Phys. Rev. Lett. **93**, 022002 (2004).

[52] L.Lee, *Report on North-American PMT-Base design*, http://burrhus.triumf.ca/g0/g0index.html/g0dsr6-pmtbase.pdf.

[53] R. Flood, private communication.

[54] G. Niculescu, *Resonant Cavities used as Beam Current Monitors*, CEBAF Internal Report (unpublished).

[55] C. Armstrong, *Beam Current Measured in Hall C*, CEBAF Internal Report (unpublished).

[56] K.B. Unser, *The Parameteric Current Transfer*, a Beam Current Monitor Developed for LEP, CERN SL/91-42 (unpublished).

[57] P. Gueye, *Status of the Actual Beam Position Monitors in Hall C Beamline*, CEBAF Internal Report CEBAF-TN-93-004 (unpublished).

[58] G. Krafft and A. Hofler, *How the LINAC Beam Position Monitors "Work"*, JLab Technical Note CEBAF-TN-93-004 (unpublished).

[59] M. Hauger et al., Nucl. Instrum. Meth. A **462**, 382 (2001).

[60] CODA *Users Manual* (1995).

[61] S. Lewis, *Overview of the Experimental Physics and Industrial Control System: EPICS*, LBNL Internal Report (2000).

[62] L. Hannelius, *G0-Geant Simulation of the Inelastic Background from the Target Windows*, Internal report G0-03-044 (unpublished).

[63] L.W. Mo and S. Tsai, Rev. Mod. Phys. **41**, 205 (1969).

[64] L.C. Maximon, Rev. Mod. Phys. **41**, 193 (1969).

[65] G. Batigne, et al., Q^2 *Determination in the First Phase of the G0 Experiment*, Internal Report G0-03-001.

[66] D.H. Beck and R.D. McKeown, Ann. Rev. Nucl. Part. Sci. **51**, 189 (2001).

[67] D.H. Beck and B.R. Holstein, Int. J. Mod. Phys. E**10**, 1 (2001).

[68] M.J. Musolf et al., Physics Reports 239 (1994).

[69] W. Koepf et al., Phys. Lett. B**288**, 11 (1992).

[70] M. Burkhardt et al., Z. Phys. C**61**, 433 (1994).

[71] R.L. Jaffe, Phys. Lett. B**229**, 275 (1989).

[72] G. Hohler et al., Nucl. Phys. B**114**, 505 (1976).

[73] H.-W. Hammer et al., Phys. Lett. B**367**, 323 (1996).

[74] U.-G. Meissner et al., Phys. Lett. B**408**, 381 (1997).

[75] H. Forkel, Phys. Rev. C**56**, 510 (1997).

[76] P. Geiger and N. Isgur, Phys. Rev. D**55**, 299 (1997).

[77] T.D. Cohen et al., Phys. Lett. B**316**, 1 (1993).

[78] N.W. Park et al., Phys. Rev. D**43**, 869 (1991).

[79] S.J. Dong et al., Phys. Rev. D**58**, (1998).

[80] T.R. Hemmert et al., Phys. Rev. C**60**, (1990).

[81] A. Abada et al., Phys. Lett. B**353**, 20 (1995).

[82] K. Goeke et al., Phys. Rev. D**65**, (2001).

[83] Th. Gutsche et al., Phys. Rev. C**66**, (2002).

[84] Jefferson Lab experiment 99-115, K. Kumar and D. Lhuiller, spokespersons.

[85] Jefferson Lab experiment 00-114, D. Armstrong and R. Michaels, spokespersons.

[86] K. McFarlane, *Required number of photoelectrons*, email to the g0-det mailing list on Oct, 6th 1998.

[87] J. Roche et *al.*, *Status Report of the G0 Detector 8 Prototype Studies*, Internal report G0-99-032.

[88] H. Breuer, *Photo-electrons for all detectors, Tosca 4.5 shapes, V7*, Internal report G0-99-012.

[89] Isotope Products Laboratories, 1800 N. Keystone Street, Burbank, CA 91504, (818)843-7000, fax (818)953-9776.

[90] R. Woo and D. Armstrong, *Spreadsheet of PMT Test Results*, Internal report G0-00-31.

VITA

Jeffery Allen Secrest

Jeffery Allen Secrest was born in Cincinnati, Ohio on November 22nd 1973 to Mike and Joy Secrest. He received a Bachelor of Science degree in physics at the University of Cincinnati in 1997. In the fall of 1997 he begun his graduate career at the University of Mississippi where he earned a Master of Arts in physics. In 1998 he won the Outstanding Teaching Assistant award. In the fall of 2000 he entered the College of William and Mary as doctoral candidate in the Department of Physics. Along the way, he earned a Masters of Science in 2001. This dissertation was defended on December 17th 2004 at the College of William and Mary.